ISSI Scientific Report SR-008

Multi-Spacecraft Analysis Methods Revisited

G. Paschmann & P. W. Daly (Eds.)

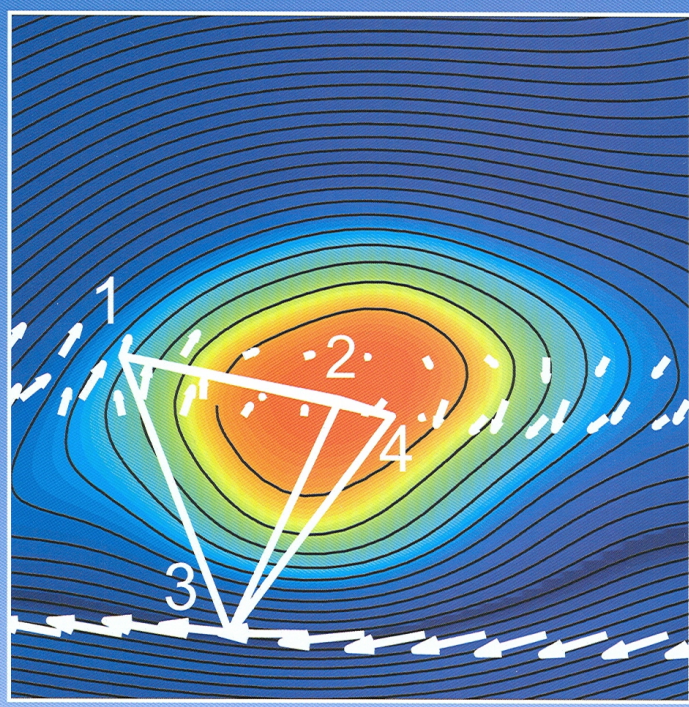

INTERNATIONAL SPACE SCIENCE INSTITUTE

SR-008

Multi-Spacecraft Analysis Methods Revisited

Editors

Götz Paschmann
Max-Planck-Institut für extraterrestrische Physik
Garching, Germany

Patrick W. Daly
Max-Planck-Institut für Sonnensystemforschung
Katlenburg-Lindau, Germany

Cover: Magneto-hydrostatic reconstruction of flux transfer event from Cluster data, showing projection of magnetic field lines onto the reconstruction plane as black curves, with the axial field in colour. The white tetrahedron is the spacecraft configuration, which moves rapidly from left to right; the white arrows represent the measured magnetic field vectors. For details and credit, see Chapter 9.

The International Space Science Institute is a Foundation under Swiss law. It is funded by the European Space Agency, the Swiss Federation, the Swiss National Science Foundation, and the University of Bern. For more information about ISSI see www.issibern.ch.

Published for: The International Space Science Institute
Hallerstrasse 6, CH-3012 Bern, Switzerland

By: ESA Communications
Keplerlaan 1, 2200 AG Noordwijk,
The Netherlands

Publication Manager: Karen Fletcher

Copyright: ©2008 ISSI/ESA
ISSN: 1608-280X
ISBN: 987-92-9221-937-6
Price: € 30

Contents

Foreword by the Directors of ISSI v

Introduction vii
- Notation Conventions . . . ix
- Cluster instruments . . . x
- Notes on ISSI SR-001 . . . xi

1 Discontinuity Orientation, Motion, and Thickness 1
- 1.1 Methods based on multi-spacecraft timing . . . 1
- 1.2 Single-spacecraft methods . . . 6
- 1.3 Applications . . . 9
- 1.4 Discussion . . . 10

2 The Curlometer and Other Gradient Based Methods 17
- 2.1 Introduction . . . 17
- 2.2 Magnetopause studies . . . 18
- 2.3 Magnetotail studies . . . 18
- 2.4 Curlometer for other structures . . . 20
- 2.5 Other gradient analyses . . . 20
- 2.6 Conclusions . . . 21

3 Geometrical Structure Analysis of the Magnetic Field 27
- 3.1 Curvature analysis . . . 27
- 3.2 Magnetic field strength gradient . . . 28
- 3.3 Magnetic rotation analysis . . . 29
- 3.4 Errors of the methods . . . 29
- 3.5 Analysis of structures . . . 30

4 Reciprocal Vectors 33
- 4.1 Introduction . . . 33
- 4.2 Crossing times in boundary analysis . . . 33
- 4.3 Properties of reciprocal vectors . . . 35
- 4.4 Estimation of spatial gradients . . . 36
- 4.5 Magnetic curvature . . . 38
- 4.6 Errors for boundary analysis and magnetic curvature . . . 40
- 4.7 Generalised reciprocal vectors for $N \neq 4$ . . . 43

5 Multi-Spacecraft Methods of Wave Field Characterisation 47
- 5.1 Introduction . . . 47
- 5.2 k-filtering — wave-telescope technique . . . 47
- 5.3 Phase differencing . . . 49
- 5.4 Method successes and limitations . . . 50
- 5.5 Outlook . . . 51

6 Multi-Spacecraft Turbulence Analysis Methods **55**
6.1 Introduction . . . 55
6.2 The k-filtering technique . . . 57
6.3 Phase differencing . . . 59
6.4 Correlation-based methods . . . 60
6.5 Other techniques . . . 61
6.6 Summary and prospects for the future . . . 62

7 Proper Frame Determination and Walén Test **65**
7.1 Introduction . . . 65
7.2 The deHoffmann-Teller frame . . . 66
7.3 General proper frame . . . 67
7.4 Walén relation . . . 69
7.5 Recent applications . . . 71
7.6 Summary . . . 71

8 Plasma Kinetics **75**
8.1 Concepts of plasma kinetics . . . 75
8.2 Applications of Liouville mapping . . . 75
8.3 Applications of remote sensing of boundaries . . . 78

9 Grad-Shafranov and MHD Reconstructions **81**
9.1 Magneto-hydrostatic structures . . . 81
9.2 Structures with field-aligned flow . . . 84
9.3 Plasma flow transverse to the magnetic field . . . 86
9.4 General two-dimensional MHD structures . . . 86
9.5 Discussion . . . 87

10 Empirical Reconstruction **91**
10.1 Introduction . . . 91
10.2 Dimensionality and initial reference frame . . . 91
10.3 One-dimensional reconstruction . . . 92
10.4 Two-dimensional reconstruction . . . 93
10.5 Discussion . . . 95

Authors' Addresses **99**

Foreword by the Directors of ISSI

It is ten years since *Analysis Methods for Multi-Spacecraft Data*, edited by Götz Paschmann and Patrick Daly, was published as the first volume in the ISSI Scientific Report Series. In these ten years, the methods and techniques have been extensively used for analysing multi-point space plasma measurements in and around the Earth's magnetosphere. Work on that book began at the time when the first attempt to launch ESA's four-spacecraft Cluster mission failed in 1996. Since the successful launches in 2000, it has become a very popular and much-quoted reference that has guided the increasingly productive data analysis of the challengingly complex Cluster data sets by the space physics scientific community. The Basic Sciences Book Award in October 1999 by the International Academy of Astronautics to the Editors and the team who produced that book has confirmed the very high esteem with which the book has been received.

Now, ten years after its publication, and after more than seven years of data accumulation by Cluster, it is time to complement the original book with a new volume in the same ISSI Scientific Reports series, now Volume SR-008, to briefly summarise the lessons learned in analysing the real multi-point data sets. The original editors, Götz Paschmann and Patrick Daly, have guided the team of authors, many of whom had taken part in producing the previous volume, in reviewing the application of the original analysis techniques to the real data and in outlining the progress that has been made in the techniques themselves. Given that the multi-spacecraft Cluster data set (now amounting to many terabytes) will remain a reference for space plasma physics research for many years to come, revisiting the first volume is a very necessary and valuable exercise. ISSI is proud of the success of the first volume and is equally proud to be associated with *Multi-Spacecraft Analysis Methods Revisited*. We are grateful to the editors and authors for their dedication to bringing to the space plasma scientists the revised techniques to support the full exploitation of the data from Cluster and other multi-spacecraft missions.

R. M. Bonnet, A. Balogh, R. von Steiger
Bern, Switzerland
February 2008

Introduction

In 1998, as part of the preparation for the Cluster mission, ISSI published a book entitled *Analysis Methods for Multi-Spacecraft Data* as the first volume, ISSI SR-001, in its Scientific Report series [*Paschmann and Daly*, 1998]. An updated version is still available in electronic form from the ISSI web site. As the book was published before Cluster was launched, no data were available for testing the multi-spacecraft methods. In the seven years since the launch in 2000, however, there have been ample opportunities to do so, as described, for example, in Volume 20 of the Space Sciences Series of ISSI.

The purpose of the present book, again published in ISSI's Scientific Report series, is to complement the original book by presenting the results of these applications, with emphasis on the validation and further development of the methods, including their limitations and pitfalls. Many of the original authors have contributed to this update.

There is no one-to-one correspondence between the chapters in the present volume and those in the original book, since the latter included chapters of a tutorial nature that are not needed here. This new book combines methods that were spread over a number of chapters, and presents additional methods that had not been developed in time, or were not included in ISSI SR-001 for other reasons.

While the focus of the methods is on multi-point measurements, this book also contains updates on a number of single-spacecraft methods, because their usefulness has become evident after their validity could be checked, for the first time, with four-spacecraft measurements.

The book is organised as follows:

- Chapter 1 (Discontinuity Orientation, Motion and Thickness) deals with the determination of the orientation, motion and thickness of plasma boundaries or discontinuities, based on single- and multi-spacecraft methods. The chapter is tied to Chapters 8, 10 and 11 of ISSI SR-001.

- Chapters 2, 3, and 4 deal with one of the unique capabilities available with four-spacecraft measurements, namely the determination of spatial derivatives of scalar or vector quantities. Chapter 2 (The Curlometer and Other Gradient Based Methods) emphasises the application to electric current density estimates from $\nabla \times \boldsymbol{B}$, hence the name curlometer, which was the subject of Chapter 16 of ISSI SR-001. But the chapter also refers to density gradient determinations and briefly introduces other gradient analysis methods. Chapter 3 (Geometrical Structure Analysis of the Magnetic Field) deals with the determination of the spatial rotation of the magnetic field, including its curvature, as well as the orientation of magnetic structures based on the gradient of the field strength. Chapter 4 (Reciprocal Vectors) summarises the utility of reciprocal vectors, dealt with in Chapters 12, 14 and 17 of ISSI SR-001, for the determination of boundary normals and speeds, as well for the estimation of spatial gradients, including the errors of those estimates.

- Chapters 5 and 6 deal with the multi-spacecraft analysis of waves and turbulence. Chapter 5 (Multi-Spacecraft Methods of Wave Field Characterisation) is about the unique four-spacecraft capability of identifying waves with different wave vectors

that are simultaneously incident on the spacecraft configuration. This topic was the subject of Chapters 3 and 4 of ISSI SR-001. Closely related to Chapter 5 is Chapter 6 (Multi-Spacecraft Turbulence Analysis Methods), which deals with the multi-point analysis of plasma turbulence, a topic not included in ISSI SR-001.

- Chapter 7 (Proper Frame Determination and Walén Test) describes the determination of the proper (co-moving) frame, in which plasma structures appear time-stationary, including the so-called deHoffmann-Teller (HT) frame, in which the plasma flow is magnetic field aligned, and describes the utility of such systems, including the identification of discontinuities via the Walén-relation test. It is an extension of Chapter 9 of ISSI SR-001.

- Chapter 8 (Plasma Kinetics) describes the analysis of plasma kinetics, particularly the determination of boundary orientation and motion from observations of anisotropies in particle distribution functions, and the mapping of electromagnetic fields based on Liouville's theorem. It is tied to Chapter 7 of ISSI SR-001.

- Chapters 9 and 10 deal with methods that allow field and plasma structures traversed by one or more spacecraft to be reconstructed in a two-dimensional region surrounding the spacecraft trajectory. Both methods were developed after ISSI SR-001 was published. Chapter 9 (Grad-Shafranov and MHD Reconstructions) describes the construction of two-dimensional maps of magnetic field and plasma flows, based on the Grad-Shafranov or other versions of the MHD equations. Chapter 10 (Empirical Reconstruction) describes a method to reconstruct the structure of plasma boundaries by assuming that the observations can be interpreted in terms of either time-stationary structures that are convected past the spacecraft or as waves propagating along the boundary.

Due to the close relation between the various subjects, it is unavoidable that there is a certain amount of overlap between the chapters. Cross-references help to navigate between chapters and subjects.

We thank the authors for the very substantial amount of time they invested in the writing of this book, and the referees (Dragos Constantinescu, Johan De Keyser, Stefan Eriksson, Mel Goldstein, Jonathan Eastwood, Bengt Sonnerup, Andris Vaivads, Joachim Vogt, Simon Walker, and Elden Whipple) for their helpful comments and criticism. We especially thank Bengt Sonnerup for his careful reading of the entire manuscript.

Götz Paschmann
Garching, Germany

Patrick W. Daly
Katlenburg-Lindau, Germany

Bibliography

Paschmann, G. and Daly, P. W., editors, 1998, *Analysis Methods for Multi-Spacecraft Data*, no. SR-001 in ISSI Scientific Reports, ESA Publ. Div., Noordwijk, Netherlands, http://www.issibern.ch/PDF-Files/analysis_methods_1_1a.pdf.

Paschmann, G., Schwartz, S. J., Escoubet, C. P., and Haaland, S., editors, 2005, *Outer Magnetospheric Boundaries: Cluster Results*, vol. 20 of *Space Science Series of ISSI*, Springer Verlag, Berlin, reprinted from *Space Sci. Rev.* 118, Nos. 1-4, 2005.

Notation Conventions

The conventions used in this book are the same as in ISSI SR-001:

- Greek subscripts $\alpha, \beta, \ldots$ apply to spacecraft; Latin subscripts $i, j, \ldots$ to cartesian coordinates.
- Vectors are indicated by boldface symbols, as $\boldsymbol{B}$, $\boldsymbol{v}$, $\boldsymbol{\omega}$. For purposes of matrix multiplication, these are considered to be *column vectors*; the corresponding row vectors are $\boldsymbol{B}^T$, $\boldsymbol{v}^T$, $\boldsymbol{\omega}^T$.
- Unit vectors are written as $\hat{\boldsymbol{n}}$, $\hat{\boldsymbol{b}}$.
- Matrices and tensors are represented by sans serif characters, e.g. M, $\mathsf{\Pi}$; their transposed forms are M^T, $\mathsf{\Pi}^T$ and their hermitian conjugates are $\mathsf{M}^\dagger$, $\mathsf{\Pi}^\dagger$.
- Multiplication of vectors is marked with the standard operators for the dot ($\boldsymbol{a} \cdot \boldsymbol{b}$) and cross ($\boldsymbol{a} \times \boldsymbol{b}$) products.
- Matrix multiplication has no explicit operator; in this context, vectors are treated as column matrices, e.g.:

$$\boldsymbol{a}^T \mathsf{S}\, \boldsymbol{b} = \sum_{ij} a_i S_{ij} b_j$$

  Thus the dyadic $\boldsymbol{a}\boldsymbol{b}^T$ represents the 3×3 tensor whose ij component is $a_i b_j$, while the product $\boldsymbol{a}^T \boldsymbol{b}$ is equivalent to $\boldsymbol{a} \cdot \boldsymbol{b} = \sum_i a_i b_i$.

Cluster instruments referred to in this book

CIS	Cluster Ion Spectrometry
CIS/HIA	CIS Hot Ion Analyzer
EFW	Electric Fields and Waves
FGM	Fluxgate Magnetometer
PEACE	Plasma Electron and Current Experiment
RAPID	Research with Adaptive Particle Imaging Detectors
STAFF	Spatio-Temporal Analysis of Field Fluctuations Experiment
STAFF-SC	STAFF Search Coil

Notes on ISSI SR-001

The Electronic Edition of ISSI SR-001, which is available as a PDF file at http://issibern.ch/PDF-Files/analysis_methods_1_1a.pdf , has a section called Notes, which collects errors corrected in the Electronic Edition and coments made by the authors. The only error reported since the Electronic Edition is the following:

In Chapter 6, Eqn. 6.8 for the heat flux vector $\boldsymbol{H}$ is missing a final term $-\frac{1}{2}\,\rho\,V^2\boldsymbol{V}$, such that the equation becomes

$$\boldsymbol{H} = \boldsymbol{Q} - \boldsymbol{V}\cdot\mathsf{P} - \frac{1}{2}\,\boldsymbol{V}\,\mathrm{Tr}\,(\mathsf{P}) - \frac{1}{2}\,\rho\,V^2\boldsymbol{V}$$

— 1 —

Discontinuity Orientation, Motion, and Thickness

BENGT U. Ö. SONNERUP
Thayer School of Engineering, Dartmouth College
Hanover, New Hampshire, USA

STEIN E. HAALAND
Max-Planck-Institut für extraterrestrische Physik
Garching, Germany
(also at: University of Bergen, Bergen, Norway)

GÖTZ PASCHMANN
Max-Planck-Institut für extraterrestrische Physik
Garching, Germany

Knowledge of their orientation, motion, and thickness is essential for the study of plasma discontinuities and the physical processes associated with them. In Chapters 8-12 of the original ISSI methods book [*Paschmann and Daly*, 1998], hereafter referred to as ISSI SR-001, a variety of single- and multi-spacecraft methods for determination of these quantities were presented. Since the publication of that book, the analysis of data from the Cluster mission has led to various inter-comparisons and generalisations of these methods. In this chapter, we present a brief overview of these developments. Applications to date have included interplanetary discontinuities as well as Earth's bow shock, magnetopause, and tail current sheet. Methods based on Cluster's curlometer and gradient capability, of utility for small spacecraft separations, are discussed in Chapter 3.

1.1 Methods based on multi-spacecraft timing

Provided they are well defined, the centre times, t_i, and durations, $2\tau_i$, of the discontinuity traversals by N spacecraft ($i = 0, 1, 2, 3, \ldots, N-1$) can be used to obtain information about the orientation, motion, and thickness of the discontinuity, under the assumption that it is locally planar and maintains a steady orientation. The timing can be determined from any quantity that is measured with sufficient time resolution by all spacecraft and that undergoes a significant change across the discontinuity or within it. In practice, the magnetic field data, which are accurately measured and have sufficiently high time resolution, are usually preferred. The situation for N=4 (the Cluster mission) is the simplest case: Two basic approaches, here referred to as the 'Constant Velocity Approach' or CVA, and the 'Constant Thickness Approach' or CTA can be found in the literature. The former was described in Section 10.4.3 [*Schwartz*, 1998] of ISSI SR-001 and discussed in

several other chapters of that book. This method was developed by *Russell et al.* [1983], who used it to study interplanetary discontinuities. For this application, the assumption of a constant velocity of the discontinuity during its encounter with all four spacecraft is well justified. CVA returns the unit vector, $\hat{\boldsymbol{n}}$, normal to the discontinuity, along with a single velocity of motion, V_0, along $\hat{\boldsymbol{n}}$, and also four thicknesses, one from each of the four spacecraft crossings.

For applications to the magnetopause and bow shock, the assumption of a constant velocity may be less appropriate because these discontinuities are often in rapidly changing motion. It is for this purpose that CTA was developed by *Haaland et al.* [2004a]. It returns the normal, $\hat{\boldsymbol{n}}$, a single thickness, d, and four velocities, one from the traversal of the discontinuity by each spacecraft. If single-spacecraft determinations (see Section 1.2) of the normal direction give accurate and consistent $\hat{\boldsymbol{n}}$ vectors from the four spacecraft, then this information can be used to allow for variable velocity and thickness in an approach referred to as the *Discontinuity Analyser* or DA (see Section 1.1.3 below and also Chapter 11 [*Dunlop and Woodward*, 1998] in ISSI SR-001 and *Dunlop et al.* [2002]). Alternatively, other single-spacecraft information can be used to allow for constant acceleration in CVA or linear time change of the thickness in CTA [*Haaland et al.*, 2004a]. A combination of CVA, CTA, and DA, called the Minimum Thickness Variation (MTV) method, has also been developed and applied in a statistical study of magnetopause crossings [*Paschmann et al.*, 2005].

1.1.1 Polynomial velocity approach (PVA): $N \geq 4$

Since future missions may contain more than four spacecraft, the development of methodology for $N > 4$ is an important task. A least-squares version of CVA for $N > 4$ was described in Chapter 12 [*Harvey*, 1998] of ISSI SR-001. This method gives a single, but presumably more reliable, estimate of the normal $\hat{\boldsymbol{n}}$ and of the velocity V_0 than is obtained for CVA with $N = 4$. It reduces to the regular CVA when $N = 4$. Here we outline a different approach, called PVA, in which the additional information gained from having data from more than four spacecraft is used to describe temporal variation of the velocity of the discontinuity. We present the PVA analysis for $N \geq 4$ and show how CVA emerges when $N = 4$. Using the approach developed for $N = 4$ by *Haaland et al.* [2004a], we write the velocity $V(t)$ of the discontinuity as the following polynomial in time t:

$$V(t) = A_0 + A_1 t + A_2 t^2 + A_3 t^3 + \ldots + A_{N-4} t^{N-4} = \sum_{j=0}^{j=N-4} A_j t^j \qquad (1.1)$$

The corresponding thicknesses $d_i (i = 0, 1, 2, 3, \ldots, N-1)$ at the individual spacecraft traversals of the discontinuity are then

$$d_i = \int_{t_i-\tau_i}^{t_i+\tau_i} V(t)dt = \left\{ \sum_{j=0}^{j=N-4} A_j t^{j+1}/(j+1) \right\}_{t_i-\tau_i}^{t_i+\tau_i} \qquad (1.2)$$

The traversals are ordered according to increasing time. The first crossing, denoted by CR0, occurs at time $t = t_0 = 0$ and has duration $2\tau_0$, while the last crossing, CR$(N-1)$, occurs at time $t = t_{N-1}$, and has duration $2\tau_{N-1}$. Similarly, the spacecraft separations

are given relative to the spacecraft that first encounters the discontinuity: the separation vector $\boldsymbol{R}_i$ runs from that spacecraft to the spacecraft that has its crossing at $t = t_i$ ($i = 1, 2, 3, \ldots, N-1$). The component of that vector along $\hat{\boldsymbol{n}}$ can then be expressed as

$$\boldsymbol{R}_i \cdot \hat{\boldsymbol{n}} = \int_{t=0}^{t=t_i} V(t)dt = A_0 \sum_{j=0}^{j=N-4} (A_j/A_0) t_i^{j+1}/(j+1) \tag{1.3}$$

There are (N-1) equations of this form. They are linear in the three components of the vector $\boldsymbol{m} \equiv \hat{\boldsymbol{n}}/A_0$ and in the $(N-4)$ coefficient ratios $[(A_1/A_0), (A_2/A_0), \ldots, (A_{N-4}/A_0)]$. The system of equations can be written in matrix form as $\mathsf{M}\boldsymbol{X} = \boldsymbol{Y}$, i.e., explicitly as

$$\begin{pmatrix} R_{1x} & R_{1y} & R_{1z} & -t_1^2/2 & \cdots & -t_1^{N''}/N'' \\ R_{2x} & R_{2y} & R_{2z} & -t_2^2/2 & \cdots & -t_2^{N''}/N'' \\ R_{3x} & R_{3y} & R_{3z} & -t_3^2/2 & \cdots & -t_3^{N''}/N'' \\ \cdots & \cdots & \cdots & \cdots & \cdots & \cdots \\ \cdots & \cdots & \cdots & \cdots & \cdots & \cdots \\ R_{N'x} & R_{N'y} & R_{N'z} & -t_{N'}^2/2 & \cdots & -t_{N'}^{N''}/N'' \end{pmatrix} \begin{pmatrix} m_x \\ m_y \\ m_z \\ A_1/A_0 \\ \cdots \\ A_{N''}/A_0 \end{pmatrix} = \begin{pmatrix} t_1 \\ t_2 \\ t_3 \\ \cdots \\ \cdots \\ t_{N'} \end{pmatrix} \tag{1.4}$$

where for reasons of compactness $(N-1)$ has been written as N' and $(N-4)$ as N''.

After the system has been solved for the vector $\boldsymbol{X}$, the coefficient A_0 (the velocity at t=0) is obtained from the normalisation condition $\hat{\boldsymbol{n}}^2 = 1$, the result being $A_0 = 1/|\boldsymbol{m}|$ and $\hat{\boldsymbol{n}} = \boldsymbol{m}/|\boldsymbol{m}|$ The coefficients $(A_1, A_2, \ldots, A_M)$ can then be obtained from $\boldsymbol{X}$ to yield a description of the temporal variation of the discontinuity velocity as the polynomial in Eqn. 1.1. The vector $\boldsymbol{m}$ is the 'slowness vector' in Section 4.2.

The durations of the N individual crossings of the discontinuity do not enter into the calculation but provide subsidiary conditions from which the N thicknesses d_i ($i = 0, 1, 2, \ldots, N-1$) can be calculated, using Eqn. 1.2. Thus, in addition to $\hat{\boldsymbol{n}}$, the method returns N thicknesses, one for each spacecraft crossing, and $(N-3)$ velocity coefficients. The thickness variations with time can also be described in terms of the polynomial

$$d(t) = \sum_{k=0}^{k=N-1} D_k t^k \tag{1.5}$$

in which the coefficients can be determined from the N thicknesses.

For $N = 4$ (Cluster), the matrix M has dimension 3×3 and therefore contains only the separation vectors. In this case, only the coefficient $A_0 = V_0$ is retained in Eqn. 1.1 and PVA reduces to CVA.

1.1.2 General polynomial approach (GPA): $N \geq 4$

We now describe a general family of methods for $N \geq 4$, in which both the crossing centre times, t_i, and the crossing durations, $2\tau_i$, are used in the determination of $\hat{\boldsymbol{n}}$ and the velocity coefficients A_i. We first modify the summations in equations 1.1, 1.2, and 1.3 to run from $j = 0$ to $j = (N-4+G)$ (rather than to $j = N-4$) so that there are now

$(N-3+G)$ coefficients A_j. We then represent the thickness $d(t)$ of the discontinuity as the polynomial in Eqn. 1.5 but with the upper limit of the summation changed from $(N-1)$ to $(N-1-G)$ so that there are now $(N-G)$ thickness coefficients. The total number of polynomial coefficients is $(2N-3)$. Since $(N-1)$ time delays relative to the first crossing and N crossing durations are measured, the problem has a total of $(2N-1)$ degrees of freedom, of which two are needed to specify the direction of the normal vector, leaving $(2N-3)$ for the coefficients in the velocity and thickness polynomials. The number denoted by G can take on the set of values $(0, 1, 2, 3, \ldots, N-1)$ so that the number of different individual methods is equal to the number of spacecraft, The case $G = 0$ corresponds to PVA, as described in Section 1.1.1. Note that negative G values are not allowed because Eqn. 1.3 then becomes over-determined: it gives $(N-1)$ equations for $(N-1+G) \leq (N-1)$ unknown quantities. Therefore, the assumption of a constant velocity of the discontinuity (CVA) is in general not consistent with the timing data for $N > 4$.

The case $G = 3$ (see Appendix) has the special property that the N velocity coefficients can be determined in terms of the $(N-3)$ thickness coefficients from Eqn. 1.2 combined with Eqn. 1.5, without coupling to Eqn. 1.3. The latter equation, together with the normalisation condition $\hat{\boldsymbol{n}}^2 = 1$, is then used to solve for the normal vector components and the $(N-3)$ thickness coefficients. This case reduces to CTA, as described by *Haaland et al.* [2004a], when $N = 4$ (Cluster). For $N > 4$, the case $G = (N-1)$ results in a more general version of CTA.

The existence of methods corresponding to G-values other than $G = 0$ and $G = 3$ was pointed out to us by J. P. Eastwood [private communication]; these additional cases are not developed in detail here. For $N = 4$, there are two methods in addition to CVA $(G = 0)$ and CTA $(G = 3)$: the case $G = 1$ describes linear time variation of the velocity, i.e., constant acceleration of the discontinuity, with parabolic time variation of the thickness; the case $G = 2$ describes parabolic time variation of the velocity and linear time variation of the thickness. These two new methods have the advantage over CVA and CTA that they do not have a built-in assumption that either the velocity or the thickness of the discontinuity is constant. If, in a chosen event, the velocity is in fact constant, or nearly constant, then the velocity coefficients from either of these new methods, except for the coefficient A_0, would come out zero or small. Similarly, if the thickness is in fact constant, or nearly constant, then the thickness coefficients, except for D_0, would come out zero or small. For $N > 4$, it would also seem preferable to use one of the methods intermediate between $G = 0$ and $G = (N-1)$ in order to maintain maximum flexibility in the polynomials describing velocity and thickness.

1.1.3 Generalisations of DA: $N \geq 4$

In the DA approach, one assumes that the normal vector $\hat{\boldsymbol{n}}$ is known from the analysis of single-spacecraft data. The two degrees of freedom thus gained can be used to provide a more detailed description of the time dependence of the velocity and thickness of the discontinuity. The development in Section 1.1.1 then simplifies to the solution of the following set of $(N-1)$ linear equations for the $(N-1)$ velocity coefficients A_j:

$$\boldsymbol{R}_i \cdot \hat{\boldsymbol{n}} = \sum_{j=0}^{j=N-2} A_j t_i^{j+1}/(j+1), \quad i = 1, 2, \ldots, N-1 \tag{1.6}$$

The N discrete thicknesses, one for each spacecraft, are then obtained from Eqn. 1.2, with its sum extended to $j = (N - 2)$. For N=4, this method reduces to the regular DA, in the form described by *Haaland et al.* [2004a], in which the velocity variation with time is described by a quadratic polynomial.

Adaptation of the general polynomial methods in Section 1.1.2 to the DA approach is straightforward. The total number of polynomial velocity coefficients is now $(N-1+G)$, while the number of thickness coefficients is $(N - G)$, with $G = (0, 1, 2, \ldots, N - 1)$ as before. The case $G = 0$ is described by Eqn. 1.6 above.

1.1.4 The case $N < 4$

We now briefly discuss cases where fewer than four spacecraft are available for timing. If $N = 1$, one or more of the single spacecraft methods described in Section 1.2 must be used to obtain the normal vector $\hat{\boldsymbol{n}}$ and the constant velocity V_0 along the normal; the only useful timing is the duration $2\tau_0$ of the discontinuity traversal, which is used to obtain the width $d_0 = 2\tau_0 V_0$.

For $N = 2$, the counterpart of CVA consists of using an $\hat{\boldsymbol{n}}$ vector obtained from a single-spacecraft method in $\boldsymbol{R}_1 \cdot \hat{\boldsymbol{n}} = A_0 t_1$ to obtain the constant velocity $V_0 = A_0$ and two thicknesses, $d_0 = 2\tau_0 V_0$ and $d_1 = 2\tau_1 V_0$. The corresponding version of CTA uses two terms, A_0 and A_1, of the sums in Eqns. 1.1, 1.2, 1.3, and 1.4, and a single term $D_0 = d$ of the sum in Eqn. 1.5. The result is two velocities, one at each spacecraft crossing, and a single thickness d.

For $N = 3$, one possibility is to still use an $\hat{\boldsymbol{n}}$ vector from single-spacecraft methods. The counterpart of PVA will then use two velocity terms, A_0 and A_1 (initial velocity and constant acceleration), in the sums on the right sides of Eqns. 1.1 and 1.2, these terms being determined from the two Eqns. 1.3. Three thicknesses will be obtained from Eqn. 1.2. More generally, the counterpart of GPA has $(2 + G)$ velocity coefficients and $(3 - G)$ thickness coefficients, with $G = (0, 1, 2)$. As before, $G = 0$ corresponds to PVA.

For $N = 3$ there are also other possibilities. For example, one may assume that, because of a poor separation between the two smallest eigenvalues, $\hat{\boldsymbol{n}}$ is not fully known from minimum-variance analysis of $\boldsymbol{B}$ (MVAB; see Section 1.2) but is constrained to lie in the plane perpendicular to the maximum-variance direction. In this case, GPA can have $(1 + G)$ velocity coefficients and $(3 - G)$ thickness coefficients, with $G = (0, 1, 2)$. The constraint is conveniently implemented by use of the eigenvectors from MVAB as basis vectors.

1.1.5 Timing and errors

The accuracy of the results produced by timing methods depends critically on the use of a systematic method for determination of the centre crossing times t_i and crossing durations $2\tau_i$. For magnetopause traversals, *Haaland et al.* [2004a] fitted a hyperbolic tangent curve to the time plot of the measured magnetic-field component along the maximum variance direction from MVAB by a least-squares procedure and then used the centre time and the duration of the fitted curve as t_i and $2\tau_i$. For bow shock crossings, *Bale et al.* [2003] fitted hyperbolic tangents to the measured density profiles.

An alternate approach for t_i is to determine the time lag between the spacecraft traversals of the discontinuity by cross correlation of corresponding time series. If, for example,

the changes in a magnetic field component are used for the analysis, the uncertainty Δt_i in the resulting time delay can be estimated as

$$(\Delta t_i)^2 = \frac{1}{(M-1)} \frac{(1-cc)}{cc} \frac{2\langle \delta B^2 \rangle}{\langle (dB/dt)^2 \rangle} \tag{1.7}$$

where M is the number of data points, cc is the optimal correlation coefficient obtained, $\langle \delta B^2 \rangle$ is the average magnitude square of the deviation of field component used from its average value, and $\langle (dB/dt)^2 \rangle$ is the average slope square of the signal. The above formula is based on the assumption of two time-shifted signals, each contaminated by white noise. Also, it is assumed that the signals approach constant levels at the two ends of the correlation window [A. V. Khrabrov, private communication].

Error estimates for CVA, based on uncertainties in the timing, were given by *Knetter et al.* [2004]. The Cluster experience with CVA, which method has been widely used, and also with CTA, has been that they often appear to work well, in some cases consistently better than the various single-spacecraft methods (see Section 1.2). But the accuracy of the vector $\hat{\boldsymbol{n}}$ is usually not high enough to allow reliable determination of the small components of $\boldsymbol{B}$ along $\hat{\boldsymbol{n}}$, encountered at the magnetopause. For example, in a magnetopause traversal such that $|\langle \boldsymbol{B} \rangle| = 40$ nT, an uncertainty of $\pm 3°$, say, in the orientation of $\hat{\boldsymbol{n}}$ leads to a corresponding uncertainty in the normal field component of up to ± 2 nT, which may be sufficient to mask the presence of a small component actually present or to preclude its accurate determination.

1.2 Single-spacecraft methods

Even for multi-spacecraft missions, methods based on data from the individual single spacecraft can play important roles. They provide consistency checks on normal vectors and velocities obtained from multi-spacecraft timing; they can help identify curvature of the discontinuity surface or systematic changes in orientation during the time interval between individual crossings; and they can be used to augment results from multi-spacecraft timing, as is done for example in the DA method.

Since the publication of ISSI SR-001, new developments of single-spacecraft methods have included finding a computationally convenient method for Minimum Faraday Residue (MFR) determination [*Khrabrov and Sonnerup*, 1998a] and Minimum Mass-flux Residue (MMR) determination [*Sonnerup et al.*, 2004] of the normal vector and velocity of a one-dimensional discontinuity. Both methods were discussed in Chapter 8 of ISSI SR-001 [*Sonnerup and Scheible*, 1998] but were not developed into suitable least-squares procedures. Recently, a unified approach to minimum-variance and minimum-residue methods has been presented [*Sonnerup et al.*, 2006, 2007] and has led to the identification of several additional methods.

The unified method can be applied to any measured quantity that obeys the classical conservation law

$$\partial \eta_i + (\partial / \partial x_j) q_{ij} = 0 \tag{1.8}$$

where η_i is the density of a conserved vector quantity, e.g., momentum, and q_{ij} is the corresponding second-rank transport tensor. If the conserved quantity is a scalar, e.g., mass, the subscript i is deleted; the density is then the scalar η and the transport is expressed

by the vector q_j. In some applications, such as the magnetic field, for which $\eta = 0$ and $q_j = B_j$, the procedure becomes regular Minimum Variance Analysis (MVAB; see Chapter 8 of ISSI SR-001). By minimisation of a suitably defined residue that is quadratic in the components of the normal vector $\hat{\boldsymbol{n}}$ and in the velocity u_n of the discontinuity (in the notation of Section 1.1: $u_n \equiv V_0$), both $\hat{\boldsymbol{n}}$ and u_n can be determined as described by *Sonnerup et al.* [2006]. The normal vector obtained from the minimisation is the eigenvector corresponding to the smallest eigenvalue of the symmetric matrix

$$Q_{ij} = \left\langle (\delta q_{ki} - U_i \delta \eta_k)(\delta q_{kj} - U_j \delta \eta_k) \right\rangle \tag{1.9}$$

where

$$U_j = \left\langle \delta \eta_i \delta q_{ij} \right\rangle / \left\langle |\delta \eta_k|^2 \right\rangle \tag{1.10}$$

is a velocity vector such that the speed of the discontinuity along $\hat{\boldsymbol{n}}$ is $u_n = \boldsymbol{U} \cdot \hat{\boldsymbol{n}} = U_j n_j$. (The physical significance of the full velocity vector $\boldsymbol{U}$ is not clear.) In these expressions, the δ symbol is used to indicate the deviation of an individual measured quantity from its average, the latter denoted by the brackets $\langle \cdots \rangle$. For example, we have $\delta \eta_k \equiv \eta_k - \langle \eta_k \rangle$. Also note that summation is implied over repeated subscripts, e.g., $|\eta_k|^2 = \eta_1^2 + \eta_2^2 + \eta_3^2$. If $\eta_i = 0$ or $\delta \eta_i = 0$, no velocity u_n is obtained and the matrix becomes $Q_{ij} = \left\langle \delta q_{ki} \delta q_{kj} \right\rangle$. Furthermore, when the transport quantity is a vector, e.g., the magnetic field, the subscript k is suppressed so that $q_{ki} = q_i = B_i$. The matrix $Q_{ij} = \left\langle \delta B_i \delta B_j \right\rangle$ then is the usual magnetic variance matrix and the method becomes MVAB. The motion of the discontinuity in this case cannot be obtained from MVAB but can be estimated as $u_n = \boldsymbol{V}_{\mathrm{HT}} \cdot \hat{\boldsymbol{n}}$ where $\boldsymbol{V}_{\mathrm{HT}}$ is the deHoffmann-Teller velocity (see Chapter 9 of ISSI SR-001 [*Khrabrov and Sonnerup*, 1998b] and Chapter 7 of the present volume).

As described in detail by *Sonnerup et al.* [2006], the above formalism can be applied to a variety of conservation laws, including mass (Minimum Mass-flux Residue, MMR), linear momentum (MLMR), total energy (MTER), entropy (MER), electric charge, and (via Faraday's law) magnetic flux. In this latter case, the result is the method known as Minimum Faraday Residue (MFR) analysis, originally described by *Terasawa et al.* [1996], and then developed into a convenient form by *Khrabrov and Sonnerup* [1998a]. This method should strictly speaking be used with actually measured electric field vectors $\boldsymbol{E}$ but has often been applied to the convection electric field, $\boldsymbol{E}_c = -\boldsymbol{v} \times \boldsymbol{B}$ instead. The basic formulas for MFR are

$$Q_{ij} = -\left\langle \delta E_i \delta E_j \right\rangle + \delta_{ij} \left\langle |\delta E_k|^2 \right\rangle - P_i P_j / \left\langle |\delta B_k|^2 \right\rangle \tag{1.11}$$

and $u_n = \boldsymbol{U} \cdot \hat{\boldsymbol{n}}$, where $\boldsymbol{U} = \boldsymbol{P} / \left\langle |\delta B_k|^2 \right\rangle$, and $\boldsymbol{P}$ is the Poynting-like vector $\boldsymbol{P} = \langle \delta \boldsymbol{E} \times \delta \boldsymbol{B} \rangle$. Examples of normal vectors from MFR and several other single-spacecraft methods, and, for comparison, also from the four-spacecraft methods CVA and CTA, are shown in Figure 1.1.

In the case of electric charge conservation, one has $\eta = 0$ in practice, so that the conservation law reduces to $\nabla \cdot \boldsymbol{j} = 0$ and $Q_{ij} = \left\langle \delta j_i \delta j_j \right\rangle$. Therefore this application reduces to minimum variance analysis (MVAJ) of the current density, $\boldsymbol{j}$ [*Haaland et al.*, 2004b; *Xiao et al.*, 2004]. In an ideal situation, one could directly measure the current density, $\boldsymbol{j} = ne(\boldsymbol{v}_i - \boldsymbol{v}_e)$, from measurements taken by a single spacecraft, but at present the velocity difference between the ions and electrons is not determined with adequate accuracy. For sufficiently small spacecraft separations, compared to the discontinuity thickness, one

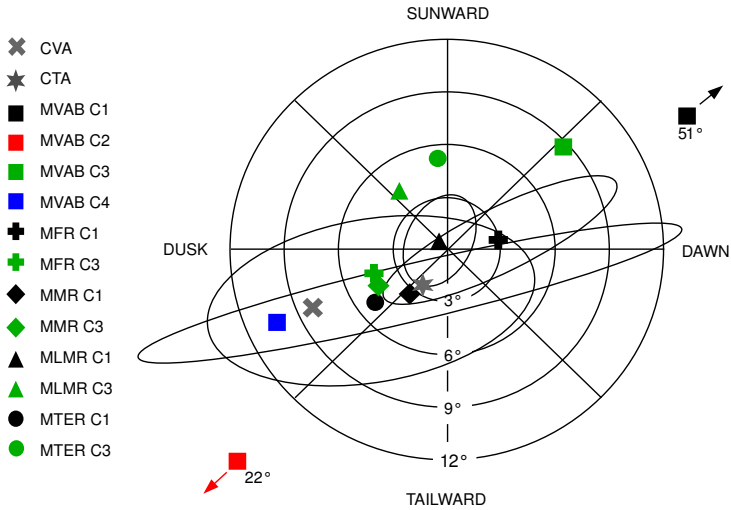

Figure 1.1: Polar plot of normal vectors from various single-spacecraft methods and also from the four-spacecraft methods CVA and CTA, applied to a magnetopause crossing by the Cluster spacecraft (C1–C4), around 0624 UT, on July 5, 2001. The centre of the plot is defined as the combined normal direction from all four spacecraft and MVAB, constrained by $\langle \boldsymbol{B} \rangle \cdot \hat{\boldsymbol{n}} = 0$. Methods requiring plasma information are based on data from the CIS/HIA instruments onboard C1 and C3. As indicated in the figure, MVAB vectors from C1 and C2 are outliers. To avoid clutter, results from MER are not shown but fall near those from MMR. Error ellipses, based on Eqn 8.23 in ISSI SR-001, are shown only for C1; they indicate 1-σ statistical uncertainties. Adapted from *Sonnerup et al.* [2006].

can instead use the $\boldsymbol{j}$-vectors from Cluster's curlometer capability (see Chapter 2), and then obtain the normal direction, $\hat{\boldsymbol{n}}$, as the eigenvector of Q_{ij} corresponding to the smallest eigenvalue (possibly using the constraint $\langle \boldsymbol{j} \rangle \cdot \hat{\boldsymbol{n}} = 0$). Since $\eta = 0$, Eqn. 1.10 fails to provide a velocity $\boldsymbol{U}$, and therefore a discontinuity speed. However, as shown by *Haaland et al.* [2004b], this speed (and, more generally, a time record of it) can be deduced from Ampère's law, applied to a one-dimensional layer.

Estimates of statistical errors for all of these methods can be obtained from equations 8.23 and 8.24 in ISSI SR-001; actual errors can be much larger, as a consequence of deviations from the base assumption underlying all of the methods, namely that the structure of the discontinuity is one-dimensional and does not change its orientation during the analysis interval. A problem occurs when the two smallest eigenvalues of Q_{ij} are not well separated. In some cases the result can be that the sought-after normal direction is closer to the intermediate-variance direction than to the minimum-variance direction. Usually, the largest uncertainty of $\hat{\boldsymbol{n}}$ is under rotation about the maximum-variance axis. In other words, the latter axis is a good tangent vector to the discontinuity surface.

Also described in the papers by *Sonnerup et al.* [2006] and *Haaland et al.* [2006b]

are methods for combining the results of several different methods into a single optimal result and methods for implementing a variety of constraints on the normal direction, e.g., the requirement that there be no magnetic flux or no plasma flux across the discontinuity or that the flow along $\hat{\boldsymbol{n}}$ be Alfvénic. As mentioned, but not described in detail in Chapter 8 of ISSI SR-001, such constraints can be conveniently enforced by use of the 3×3 matrix operator $P_{ij} \equiv \delta_{ij} - e_i e_j$, where δ_{ij} is the identity operator. The matrix P_{ij} projects any vector to which it is applied (either to the left or to the right) onto the plane perpendicular to a chosen unit vector $\hat{\boldsymbol{e}}$. For example, to implement the frequently-used tangential-discontinuity constraint, $\langle \boldsymbol{B} \rangle \cdot \hat{\boldsymbol{n}} = 0$, one uses $\hat{\boldsymbol{e}} = \langle \boldsymbol{B} \rangle / |\langle \boldsymbol{B} \rangle|$. The matrix $P_{ik} Q_{kn} P_{nj}$ is then constructed. It has two non-zero eigenvalues, λ'_1 and λ'_2, with corresponding eigenvectors $\hat{\boldsymbol{x}}'_1$ and $\hat{\boldsymbol{x}}'_2$. The third eigenvalue is $\lambda'_3 = 0$, with corresponding eigenvector $\hat{\boldsymbol{x}}'_3 = \hat{\boldsymbol{e}}$. Provided λ'_1 is well separated from λ'_2, the intermediate-variance direction, $\hat{\boldsymbol{x}}'_2$, should be a good predictor of the constrained normal vector, i.e., $\hat{\boldsymbol{n}} = \hat{\boldsymbol{x}}'_2$.The constraint $\langle \boldsymbol{B} \rangle \cdot \hat{\boldsymbol{n}} = 0$ was first implemented by *Sonnerup and Cahill* [1968] by use of the less elegant Lagrange-multiplier method detailed in Chapter 8 of ISSI SR-001. Still another method for implementing this constraint was used by *Bargatze et al.* [2005].

1.3 Applications

In addition to the applications already cited in the previous sections, four-spacecraft timing analysis (CVA), sometimes including comparisons with minimum variance results for the individual spacecraft, has been applied to determine the orientation, motion, and thickness of

- the heliospheric current sheet, including a comparison with results from from MVAB [*Eastwood et al.*, 2002];
- a large set of interplanetary discontinuities, including comparisons with MVAB results [*Knetter et al.*, 2004];
- the bow shock [*Horbury et al.*, 2001, 2002; *Bale et al.*, 2003; *Maksimovic et al.*, 2003; *Behlke et al.*, 2003];
- magnetic structures near the quasi-parallel bow shock [*Lucek et al.*, 2004];
- magnetic structures in the magnetosheath [*Horbury et al.*, 2004];
- the magnetopause [*Owen et al.*, 2004; *Paschmann et al.*, 2005; *Dunlop and Balogh*, 2005], with the last using the DA method.
- the current sheet in the magnetotail, with comparisons to MVAB [*Runov et al.*, 2003, 2005, 2006].

.

Of the single-spacecraft methods, MVAB is applied frequently, but the more advanced methods only rarely:

- *Nykyri et al.* [2006] have applied MFR to a number of magnetopause crossings;
- *Weimer et al.* [2003]; *Haaland et al.* [2007] have applied MVAB with the constraint $\langle \boldsymbol{B} \rangle \cdot \hat{\boldsymbol{n}} = 0$ to interplanetary magnetic field data.

1.4 Discussion

The Cluster mission has provided opportunities to compare normal vectors and discontinuity velocities from methods based on multi-spacecraft timing (such as CVA and CTA) or, for small spacecraft separation, gradient determinations [*Shi et al.*, 2005, 2006] with those based on single-spacecraft data (such as MVAB and MFR) and also, within each group, to inter-compare the various methods. Results of such comparisons at the magnetopause are limited [*Haaland et al.*, 2004a; *Sonnerup et al.*, 2004, 2006; *Shi et al.*, 2006] but indicate that, with proper care, agreement of various normal vectors can be as close as 5°, or better, as illustrated in Figure1.1, with velocities that agree within 10–20 km s^{-1}. However, as seen in the figure, one often also finds outlying results, in particular among the normal vectors from MVAB. This behaviour can be the result of poor separation of the two smallest eigenvalues. For example, a perfectly one-dimensional current sheet, in which the electric current is also purely unidirectional, has the two smallest eigenvalues from MVAB equal to zero, leaving the normal direction undetermined. If this current sheet is modified by including a set of tearing-mode magnetic islands, the variance of the magnetic field component along the true normal becomes nonzero while that in the direction of the current remains zero. As a result, it is now the eigenvector corresponding to the intermediate eigenvalue, rather than that corresponding to the minimum eigenvalue, that points in the normal direction. If one also includes small deviations from the unidirectionality of the current, the result may be that neither of these two eigenvectors provides a meaningful estimate of the normal direction. The eigenvector corresponding to the largest eigenvalue is usually still tangential, or nearly tangential, to the current sheet but all that can be said about the normal vector itself is that it lies nearly in a plane perpendicular to that vector. Comparison of results from MVAB with those from timing indicates that problems of this type occur frequently in applications to interplanetary discontinuities [*Knetter et al.*, 2004] and to the current sheet in the geomagnetic tail [*Shen et al.*, 2003; *Zhang et al.*, 2005; *Volwerk*, 2006]. It appears that these structures are better treated by using multi-spacecraft timing methods such as CVA or CTA, or, for small spacecraft separation, by using gradient methods (see Chapter 3 and *Shen et al.* [2007]).

An alternative approach for interplanetary discontinuities, the magnetopause, and the tail current sheet, is to apply the constraint $\langle \boldsymbol{B} \rangle \cdot \hat{\boldsymbol{n}} = 0$ to single-spacecraft methods, such as MVAB. For examples, see the work by *Weimer et al.* [2003] (although this is not apparent from their paper, as discussed by *Bargatze et al.* [2005] and by *Haaland et al.* [2006a]) and references therein. In the above applications, it remains difficult to establish whether the current sheets are true tangential discontinuities or have a small nonzero normal magnetic field component as for propagating Alfvén waves or shocks.

In light of what appears to be a widespread lack of understanding, and misinterpretation of the results from the MVAB method in the literature, the following comments concerning all the single-spacecraft methods are in order. Most of them were already discussed for MVAB in Chapter 8 of ISSI SR-001.

The error estimates given in Eqn. 8.23 of ISSI SR-001, refer only to the statistical uncertainties of the eigenvectors themselves. They give essentially the same result as the bootstrap method. As expected for statistical errors, the estimates are inversely proportional to $\sqrt{M-1}$, M being the number of data points used. Unless the smallest eigenvalue increases with increasing time resolution, owing to the presence of higher-frequency noise, the uncertainty therefore gets smaller as the time resolution of the data used in the anal-

ysis increases. When the two smallest eigenvalues are well separated, the uncertainty in the eigenvector of the smallest eigenvalue (the minimum-variance direction) under rotation about the maximum variance eigenvector direction is approximately inversely proportional to the square root of the ratio of intermediate to minimum eigenvalue. For this reason, a ratio of 10 or more is often used as a rule of thumb for a desirable event. It is extremely important to realise that these estimates only describe the statistical uncertainties in the eigenvector orientations. They do not account for errors associated with the interpretation of the minimum-variance direction as representing the direction normal to a current sheet. For example, in the current sheet described above that contains a purely unidirectional one-dimensional current and a set of magnetic islands, the eigenvalue ratio is infinite so that the minimum variance direction has zero statistical error. But the interpretation of this direction as the normal to the current sheet is in error: In this case, it is the intermediate variance direction that is the appropriate predictor for the normal vector. The presence of two small eigenvalues (even when their ratio is large or very large) is a warning that this kind of situation may be at hand. In short, a large intermediate-to-minimum eigenvalue ratio is, on its own, not a sufficient indicator that the minimum variance direction is a good predictor of the normal. In reporting results from MVAB and other single-spacecraft methods, it is therefore not sufficient to give this ratio. The actual set of eigenvalues and the number of data points used should be given. Hodogram plots are also useful tools in visually assessing whether the minimum-variance direction is a valid predictor of the normal direction.

Appendix

Here we present the details of GPA for the special case $G = 3$. The polynomial in Eqn. 1.5, with its upper summation limit changed to $(N - 4)$, can be evaluated at each of the centre times $t = t_i$ of the N spacecraft crossings ($i = 0, 1, 2, \ldots, N - 1$) to give the N unknown thicknesses, d_i, in terms of the unknown $(N - 3)$ coefficients $(D_0, D_1, D_2, \ldots, D_{N-4})$. When these d_i values are substituted into Eqn. 1.2, with upper summation limit changed to $(N - 1)$, we obtain N linear equations for the N coefficients A_i. In matrix form, this system of equations is

$$\begin{pmatrix} 1 & 0 & 0 & \cdots & 0 \\ 1 & t_1 & t_1^2 & \cdots & t_1^{N-4} \\ 1 & t_2 & t_2^2 & \cdots & t_2^{N-4} \\ 1 & t_3 & t_3^2 & \cdots & t_3^{N-4} \\ \cdots & \cdots & \cdots & \cdots & \cdots \\ 1 & t_{N-1} & t_{N-1}^2 & \cdots & t_{N-1}^{N-4} \end{pmatrix} \begin{pmatrix} D_0 \\ D_1 \\ D_2 \\ D_3 \\ \cdots \\ D_{N-4} \end{pmatrix} = \begin{pmatrix} 2\tau_0 & 0 & 2\tau_0^3/3 & 0 & \cdots & \mathsf{M}_{1N} \\ 2\tau_1 & M_{22} & \mathsf{M}_{23} & \mathsf{M}_{24} & \cdots & \mathsf{M}_{2N} \\ 2\tau_2 & M_{32} & \mathsf{M}_{33} & \mathsf{M}_{34} & \cdots & \mathsf{M}_{3N} \\ 2\tau_3 & M_{42} & \mathsf{M}_{43} & \mathsf{M}_{44} & \cdots & \mathsf{M}_{4N} \\ \cdots & \cdots & \cdots & \cdots & \cdots & \cdots \\ 2\tau_{N-1} & \mathsf{M}_{N2} & \mathsf{M}_{N3} & \mathsf{M}_{N4} & \cdots & \mathsf{M}_{NN} \end{pmatrix} \begin{pmatrix} A_0 \\ A_1 \\ A_2 \\ A_3 \\ \cdots \\ A_{N-1} \end{pmatrix} \tag{1.12}$$

where the elements of the $N \times N$ matrix M on the right are $\mathsf{M}_{pq} = [(t_{p-1} + \tau_{p-1})^q - (t_{p-1} - \tau_{p-1})^q]/q$ with $p, q = 1, 2, 3, \ldots, N$ and $t_0 = 0$. By inverting M, we may express each of the N velocity coefficients $(A_0, A_1, \ldots, A_{N-1})$ as a linear combination of the (N-3) thickness coefficients $(D_0, D_1, \ldots, D_{N-4})$. In other words, we may write $A_{i-1} = K_{ij} D_{j-1}$ with i=1,2,..,N and $j = 1, 2, \ldots, N-3$. The matrix K therefore has N rows and $(N-3)$ columns; it is obtained by multiplying M^{-1} into the time matrix on the left in Eqn. 1.12. The A_i values thus obtained are substituted into a modified version of Eqn. 1.3, namely

$$\boldsymbol{R}_k \cdot \boldsymbol{m} = (1/D_0) \sum_{i=1}^{i=N} A_{i-1} t_k^i / i = \sum_{i=1}^{i=N} \sum_{j=1}^{j=N-3} (t_k^i / i) K_{ij} (D_{j-1}/D_0) \tag{1.13}$$

where $\boldsymbol{m} = \hat{\boldsymbol{n}}/D_0$. The $(N-1)$ linear equations $(k = 1, 2, \ldots, N-1)$ expressed by Eqn. 1.13 can now be solved for the $(N-1)$ unknown quantities comprising the components of the vector $\boldsymbol{X}^T = [m_x, m_y, m_z, (D_1/D_0), (D_2/D_0), \ldots, (D_{N-4}/D_0)]$ (the superscript T denotes the transpose, i.e., $\boldsymbol{X}$ itself is a column vector). Finally, D_0 is obtained from the normalisation $|\boldsymbol{m}| = 1/D_0$. Thus the calculation will return N velocity coefficients and (N-3) thickness coefficients. The resulting matrix equation is again of the form $\tilde{\mathsf{M}} \cdot \boldsymbol{X} = \boldsymbol{Y}$, where the known vector $\boldsymbol{Y}$ on the right-hand side is now specified by $Y_k^T = \sum_{i=1}^{i=N} (t_k^i / i) K_{i1}$ and the matrix $\tilde{\mathsf{M}}$ is of the form

$$\tilde{\mathsf{M}} = \begin{pmatrix} R_{1x} & R_{1y} & R_{1z} & \tilde{\mathsf{M}}_{14} & \cdots & \tilde{\mathsf{M}}_{1(N-1)} \\ R_{2x} & R_{2y} & R_{2z} & \tilde{\mathsf{M}}_{24} & \cdots & \tilde{\mathsf{M}}_{2(N-1)} \\ R_{3x} & R_{3y} & R_{3z} & \tilde{\mathsf{M}}_{34} & \cdots & \tilde{\mathsf{M}}_{3(N-1)} \\ \cdots & \cdots & \cdots & \cdots & \cdots & \cdots \\ \cdots & \cdots & \cdots & \cdots & \cdots & \cdots \\ R_{(N-1)x} & R_{(N-1)y} & R_{(N-1)z} & \tilde{\mathsf{M}}_{(N-1)4} & \cdots & \tilde{\mathsf{M}}_{(N-1)(N-1)} \end{pmatrix} \tag{1.14}$$

The matrix components $\tilde{\mathsf{M}}_{kj}$ $(k = 1, 2, \ldots, N-1;\ j = 4, 5, \ldots, N-1)$ are given by

$$\tilde{\mathsf{M}}_{kj} = \sum_{i=1}^{i=N} (t_k^i / i) K_{ij} \tag{1.15}$$

For the case of four spacecraft, only the coefficient D_0 in Eqn. 1.5 is nonzero and is equal to the constant discontinuity thickness d. In this case, the left side of Eqn. 1.12 is a 4×1 column vector in which all four components are equal to D_0 and the matrix on the right has dimension 4×4. This matrix can then be inverted to produce the vector $(A_0/D_0;\ A_1/D_0;\ A_2/D_0;\ A_3/D_0)$ and the method reduces to CTA.

Software implementation

The multi-spacecraft methods (CVA, CTA, and DA) for the case of four spacecraft, along with the various single-spacecraft methods, are implemented in the QSAS software, available at http://www.sp.ph.ic.ac.uk/csc-web/QSAS/.

Acknowledgements

The work by B.U.Ö.S. was supported by the National Aeronautics and Space Administration under Cluster Theory Guest Investigator Grant NNG-05-GG26G to Dartmouth College. Work by S.E.H. was supported by Deutsches Zentrum für Luft- und Raumfahrt under grant 50 OC 01 and by the Norwegian Research Council.

Bibliography

Bale, S. D., Mozer, F. S., and Horbury, T. S., 2003, Density-Transition Scale at Quasiperpendicular Collisionless Shocks, *Phys. Rev. Lett.*, **91**, 265004, doi:10.1103/PhysRevLett.91.265004.

Bargatze, L. F., McPherron, R. L., Minamora, J., and Weimer, D., 2005, A new interpretation of Weimer et al.'s solar wind propagation delay technique, *J. Geophys. Res.*, **110**, A07105, doi:10.1029/2004JA010902.

Behlke, R., André, M., Buchert, S. C., Vaivads, A., Eriksson, A. I., Lucek, E. A., and Balogh, A., 2003, Multipoint electric field measurements of Short Large-Amplitude Magnetic Structures (SLAMS) at the Earth's quasi-parallel bow shock, *Geophys. Res. Lett.*, **30**, 1177, doi:10.1029/2002GL015871.

Dunlop, M. W. and Balogh, A., 2005, Magnetopause current as seen by Cluster, *Ann. Geophys.*, **23**, 901–907, http://www.ann-geophys.net/23/901/2005/.

Dunlop, M. W. and Woodward, T. I., 1998, Multi-Spacecraft Discontinuity Analysis: Orientation and Motion, in *Analysis Methods for Multi-Spacecraft Data*, edited by G. Paschmann and P. W. Daly, no. SR-001 in ISSI Scientific Reports, chap. 11, pp. 271–305, ESA Publ. Div., Noordwijk, Netherlands.

Dunlop, M. W., Balogh, A., and Glassmeier, K.-H., 2002, Four-point Cluster application of magnetic field analysis tools: The discontinuity analyzer, *J. Geophys. Res.*, **107**, 1385, doi:10.1029/2001JA005089.

Eastwood, J. P., Balogh, A., Dunlop, M. W., and Smith, C. W., 2002, Cluster observations of the heliospheric current sheet and an associated magnetic flux rope and comparisons with ACE, *J. Geophys. Res.*, **107**, 1365, doi:10.1029/2001JA009158.

Haaland, S., Sonnerup, B., Dunlop, M., Balogh, A., Georgescu, E., Hasegawa, H., Klecker, B., Paschmann, G., Puhl-Quinn, P., Rème, H., Vaith, H., and Vaivads, A., 2004a, Four-spacecraft determination of magnetopause orientation, motion and thickness: comparison with results from single-spacecraft methods, *Ann. Geophys.*, **22**, 1347–1365, http://www.ann-geophys.net/22/1347/2004/.

Haaland, S., Sonnerup, B. U. Ö., Dunlop, M. W., Georgescu, E., Paschmann, G., Klecker, B., and Vaivads, A., 2004b, Orientation and motion of a discontinuity from Cluster curlometer capability: Minimum variance of current density, *Geophys. Res. Lett.*, **31**, L10804, doi:10.1029/2004GL020001.

Haaland, S., Paschmann, G., and Sonnerup, B. U. Ö., 2006a, Comment on "A new interpretation of Weimer et al.'s solar wind propagation delay technique" by Bargatze et al., *J. Geophys. Res.*, **111**, A06102, doi:10.1029/2005JA011376.

Haaland, S., Sonnerup, B. U. Ö., Paschmann, G., Georgescu, E., Dunlop, M. W., Balogh, A., Klecker, B., Rème, H., and Vaivads, A., 2006b, Discontinuity Analysis with Cluster, in *Cluster and Double Star Symposium*, ESA SP-598, ESA Publ. Div., Noordwijk, Netherlands.

Haaland, S. E., Paschmann, G., Förster, M., Quinn, J. M., Torbert, R. B., McIlwain, C. E., Vaith, H., Puhl-Quinn, P. A., and Kletzing, C. A., 2007, High-latitude plasma convection from Cluster EDI measurements: method and IMF-dependence, *Ann. Geophys.*, **25**, 239–253, http://www.ann-geophys.net/25/239/2007/.

Harvey, C. C., 1998, Spatial Gradients and the Volumetric Tensor, in *Analysis Methods for Multi-Spacecraft Data*, edited by G. Paschmann and P. W. Daly, no. SR-001 in ISSI Scientific Reports, chap. 12, pp. 307–322, ESA Publ. Div., Noordwijk, Netherlands.

Horbury, T. S., Cargill, P. J., Lucek, E. A., Balogh, A., Dunlop, M. W., Oddy, T. M., Carr, C., Brown, P., Szabo, A., and Fornaçon, K.-H., 2001, Cluster magnetic field observations of the bowshock: Orientation, motion and structure, *Ann. Geophys.*, **19**, 1399–1409, http://www.ann-geophys.net/19/1399/2001/.

Horbury, T. S., Cargill, P. J., Lucek, E. A., Eastwood, J., Balogh, A., Dunlop, M. W., Fornacon, K.-H., and Georgescu, E., 2002, Four spacecraft measurements of the quasiperpendicular terrestrial bow shock: Orientation and motion, *J. Geophys. Res.*, **107**, 1208, doi:10.1029/2001JA000273.

Horbury, T. S., Lucek, E. A., Balogh, A., Dandouras, I., and Rème, H., 2004, Motion and orientation of magnetic field dips and peaks in the terrestrial magnetosheath, *J. Geophys. Res.*, **109**, A09209, doi:10.1029/2003JA010237.

Khrabrov, A. V. and Sonnerup, B. U. Ö., 1998a, Orientation and motion of current layers: Minimization of the Faraday residue, *Geophys. Res. Lett.*, **25**, 2373.

Khrabrov, A. V. and Sonnerup, B. U. Ö., 1998b, DeHoffmann-Teller Analysis, in *Analysis Methods for Multi-Spacecraft Data*, edited by G. Paschmann and P. W. Daly, no. SR-001 in ISSI Scientific Reports, chap. 9, pp. 221–248, ESA Publ. Div., Noordwijk, Netherlands.

Knetter, T., Neubauer, F. M., Horbury, T., and Balogh, A., 2004, Four-point discontinuity observations using Cluster magnetic field data: A statistical survey, *J. Geophys. Res.*, **109**, A06102, doi:10.1029/2003JA010099.

Lucek, E., Horbury, T., Balogh, A., Dandouras, I., and Rème, H., 2004, Cluster observations of structures at quasi-parallel bow shocks, *Ann. Geophys.*, **22**, 2309–2313, http://www.ann-geophys.net/22/2309/2004/.

Maksimovic, M., Bale, S. D., Horbury, T. S., and André, M., 2003, Bow shock motions observed with CLUSTER, *Geophys. Res. Lett.*, **30**, 1393, doi:10.1029/2002GL016761.

Nykyri, K., Otto, A., Lavraud, B., Mouikis, C., Kistler, L. M., Balogh, A., and Rème, H., 2006, Cluster observations of reconnection due to the Kelvin-Helmholtz instability at the dawnside magnetospheric flank, *Ann. Geophys.*, **24**, 2619–2643, http://www.ann-geophys.net/24/2619/2006/.

Owen, C., Taylor, M., Krauklis, I., Fazakerley, A., Dunlop, M., and Bosqued, J., 2004, Cluster observations of surface waves on the dawn flank magnetopause, *Ann. Geophys.*, **22**, 971–983, http://www.ann-geophys.net/22/971/2004/.

Paschmann, G. and Daly, P. W., editors, 1998, *Analysis Methods for Multi-Spacecraft Data*, no. SR-001 in ISSI Scientific Reports, ESA Publ. Div., Noordwijk, Netherlands, http://www.issibern.ch/PDF-Files/analysis_methods_1_1a.pdf.

Paschmann, G., Haaland, S., Sonnerup, B. U. Ö., Hasegawa, H., Georgescu, E., Klecker, B., Phan, T. D., Rème, H., and Vaivads, A., 2005, Characteristics of the near-tail dawn magnetopause and boundary layer, *Ann. Geophys.*, **23**, 1481–1497, http://www.ann-geophys.net/23/1481/2005/.

Runov, A., Nakamura, R., Baumjohann, W., Treumann, R. A., Zhang, T. L., Volwerk, M., Vörös, Z., Balogh, A., Glaßmeier, K.-H., Klecker, B., Rème, H., and Kistler, L., 2003, Current sheet structure near magnetic X-line observed by Cluster, *Geophys. Res. Lett.*, **30**, 1579, doi:10.1029/2002GL016730.

Runov, A., Sergeev, V. A., Baumjohann, W., Nakamura, R., Apatenkov, S., Asano, Y., Volwerk, M., Vörös, Z., Zhang, T. L., Petrukovich, A., Balogh, A., Sauvaud, J.-A., Klecker, B., and Rème, H., 2005, Electric current and magnetic field geometry in flapping magnetotail current sheets, *Ann. Geophys.*, **23**, 1391–1403, http://www.ann-geophys.net/23/1391/2005/.

Runov, A., Sergeev, V. A., Nakamura, R., Baumjohann, W., Apatenkov, S., Asano, Y., Takada, T., Volwerk, M., Vörös, Z., Zhang, T. L., Sauvaud, J.-A., Rème, H., and Balogh, A., 2006, Local structure of the magnetotail current sheet: 2001 Cluster observations, *Ann. Geophys.*, **24**, 247–262, http://www.ann-geophys.net/24/247/2006/.

Russell, C. T., Mellot, M. M., Smith, E. J., and King, J. H., 1983, Multiple spacecraft observations of interplanetary shocks: Four spacecraft determination of shock normals, *J. Geophys. Res.*, **88**, 4739–4748.

Schwartz, S. J., 1998, Shock and Discontinuity Normals, Mach Numbers, and Related Parameters, in *Analysis Methods for Multi-Spacecraft Data*, edited by G. Paschmann and P. W. Daly, no. SR-001 in ISSI Scientific Reports, chap. 10, pp. 249–270, ESA Publ. Div., Noordwijk, Netherlands.

Shen, C., Li, X., Dunlop, M., Liu, Z. X., Balogh, A., Baker, D. N., Hapgood, M., and Wang, X., 2003, Analyses on the geometrical structure of magnetic field in the current sheet based on cluster measurements, *J. Geophys. Res.*, **108**, 1168, doi:10.1029/2002JA009612.

Shen, C., Dunlop, M., Li, X., Liu, Z. X., Balogh, A., Zhang, T. L., Carr, C. M., Shi, Q. Q., and Chen, Z. Q., 2007, New approach for determining the normal of the bow shock based on Cluster four-point magnetic field measurements, *J. Geophys. Res.*, **112**, A03201, doi:10.1029/2006JA011699.

Shi, Q. Q., Shen, C., Pu, Z. Y., Dunlop, M. W., Zong, Q.-G., Zhang, H., Xiao, C. J., Liu, Z. X., and Balogh, A., 2005, Dimensional analysis of observed structures using multipoint magnetic field measurements: Application to Cluster, *Geophys. Res. Lett.*, **32**, L012105, doi:10.1029/2005GL022454.

Shi, Q. Q., Shen, C., Dunlop, M. W., Pu, Z. Y., Zong, Q.-G., Liu, Z. X., Lucek, E., and Balogh, A., 2006, Motion of observed structures calculated from multi-point magnetic field measurements: Application to Cluster, *Geophys. Res. Lett.*, **33**, L08109, doi:10.1029/2005GL025073.

Sonnerup, B. U. Ö. and Cahill, L. J., Jr., 1968, Explorer 12 Observations of the Magnetopause Current Layer, *J. Geophys. Res.*, **73**, 1757.

Sonnerup, B. U. Ö. and Scheible, M., 1998, Minimum and Maximum Variance Analysis, in *Analysis Methods for Multi-Spacecraft Data*, edited by G. Paschmann and P. W. Daly, no. SR-001 in ISSI Scientific Reports, chap. 8, pp. 185–220, ESA Publ. Div., Noordwijk, Netherlands.

Sonnerup, B. U. Ö., Haaland, S., Paschmann, G., Lavraud, B., Dunlop, M. W., Rème, H., and Balogh, A., 2004, Orientation and motion of a discontinuity from single-spacecraft measurements of plasma velocity and density: Minimum mass flux residue, *J. Geophys. Res.*, **109**, A03221, doi:10.1029/2003JA010230.

Sonnerup, B. U. Ö., Haaland, S., Paschmann, G., Dunlop, M. W., Rème, H., and Balogh, A., 2006, Orientation and motion of a plasma discontinuity from single-spacecraft measurements: Generic residue analysis of

Cluster data, *J. Geophys. Res.*, **111**, A05203, doi:10.1029/2005JA011538.

Sonnerup, B. U. Ö., Haaland, S., Paschmann, G., Dunlop, M. W., Rème, H., and Balogh, A., 2007, Correction to "Orientation and motion of a plasma discontinuity from single-spacecraft measurements: Generic residue analysis of Cluster data", *J. Geophys. Res.*, **112**, A04201, doi:10.1029/2007JA012288.

Terasawa, T., Kawano, H., Shinohara, I., Mukai, T., Saito, Y., Hoshino, M., Nishida, A., Machida, S., Nagai, T., Yamamoto, T., and Kokobun, S., 1996, On the determination of a moving MHD structure: Minimization of residue of intergral Faraday's equation, *J. Geomagn. Geoelectr.*, **48**, 603, doi:10.1029/2006GL028802.

Volwerk, M., 2006, Multi-Satellite observations of ULF waves, in *Magnetospheric ULF waves: Synthesis and new directions*, edited by K. Takahashi, P. J. Chi, R. E. Denton, and R. L. Lysak, pp. 109 – 135, AGU, Washington.

Weimer, D. R., Ober, D. M., Maynard, N. C., Collier, M. R., McComas, D. J., Ness, N. F., Smith, C. W., and Watermann, J., 2003, Predicting interplanetary magnetic field (IMF) propagation delay times using the minimum variance technique, *J. Geophys. Res.*, **108**, 1026, doi:10.1029/2002JA009405.

Xiao, C. J., Pu, Z. Y., Ma, Z. W., Fu, S. Y., Huang, Z. Y., and Zong, Q. G., 2004, Inferring of flux rope orientation with the minimum variance analysis technique, *J. Geophys. Res.*, **109**, A011218, doi:10.1029/2004JA010594.

Zhang, T. L., Baumjohann, W., Nakamura, R., Volwerk, M., Runov, A., Vörös, Z., Glassmeier, K.-H., and Balogh, A., 2005, Neutral sheet normal direction determination, *Adv. Space Res.*, **36**, 1940–1945, doi:10.1016/j.asr.2004.08.010.

— 2 —

The Curlometer and Other Gradient Based Methods

MALCOLM W. DUNLOP
Rutherford Appleton Laboratory
Chilton, Didcot, United Kingdom

JONATHAN P. EASTWOOD
Space Sciences Laboratory
University of California at Berkeley
Berkeley, California, USA

2.1 Introduction

The magnetic field measurements on the four Cluster spacecraft can be combined to produce a determination of the electric current density, $\boldsymbol{j}$, point by point in time, from Ampère's law, i.e., through an estimate of the curl of the magnetic field, $\nabla \times \boldsymbol{B}$, assuming the displacement current may be neglected (an assumption nearly always true in space plasmas). This combination of spatial gradients is named the Curlometer technique, first introduced by *Dunlop et al.* [1988], and first used on Cluster measurements by *Dunlop et al.* [2002b]. Although estimates of current density from single and dual spacecraft have been attempted in the past [e.g. *van Allen and Adnan*, 1992] (a simple 1-D current layer, sampled from an individual spacecraft, can at least give an estimate of the current magnitude), these estimates also depend on accurate knowledge of relative orientation and motion in order to obtain positions within a current layer (the finite region where the current density is distributed). The curlometer technique independently estimates the current vector at each time in the data stream and can be understood in a number of different ways, as outlined in Chapters 12, 14, 15, and 16 of ISSI SR-001. In using the Curlometer, a clear understanding of the associated caveats is important, the main one being that only linear estimates of $\nabla \times \boldsymbol{B}$ and $\nabla \cdot \boldsymbol{B}$ can be made. Multi-spacecraft analysis also depends upon temporal behaviour, and most methods assume some degree of stationarity in their interpretation. The Curlometer is an important part of the analysis of spatial gradients as measured by four spacecraft, and this general problem was addressed in part in ISSI SR-001. A number of additional methods have since been introduced which are also based on the use of spatial gradients and we also deal briefly with these below, or reference them.

The four Cluster spacecraft fly in an evolving configuration, which repeats every orbit (apart from minor perturbations), but which has been changed at intervals during the mission to cover a large range of spacecraft separation distances (100–10,000 km) at the magnetopause and in the magnetotail. The results presented here therefore have been confirmed over a variety of spatial scales, and have been used in a number of different investigations, and below we list those papers that have used the technique in these circumstances. Through these studies, an understanding of the applicability of the method has developed. For example, the thickness of a planar current layer can be accurately estimated from its magnetic profile at each spacecraft and the corresponding boundary crossing times; the

latter also giving a determination of boundary motion relative to the Cluster array, which scales the corresponding current profile through the current layer. The estimate of electric current density can be representative even when the configuration of Cluster spacecraft approaches the thickness of the current layer and minimum variance analysis on the Curlometer measurements can estimate the current normal. The other gradient methods can be used to calculate a number of other properties, such as the dimensionality of the structure.

2.2 Magnetopause studies

The Curlometer has been used to measure the magnetopause current itself [*Dunlop and Balogh*, 2005], and has been applied to several studies of magnetopause reconnection [*Maynard et al.*, 2003; *Phan et al.*, 2004; *Maynard*, 2005; *Panov et al.*, 2006a, b]. It has also been used in studies of the cusp [*Khotyaintsev et al.*, 2004; *Dunlop and Balogh*, 2005], and to investigate the properties of flux ropes on the magnetopause [*Zuo et al.*, 2004; *Xiao et al.*, 2004a], including high latitudes [*Thompson et al.*, 2004]. Some of these studies have been summarised in Chapter 8 of Volume 20 of ISSI's Space Sciences Series [*De Keyser et al.*, 2005].

In one study [*Dunlop and Balogh*, 2005] the Curlometer technique was able to consistently estimate the magnetopause current vector with a clear alignment to the magnetopause surface (which has a mean thickness of $\sim$1200 km and mean crossing speed of $\sim$25 km s^{-1}), consistent with a Chapman-Ferraro current. The mean current was $\sim$10 nA m^{-2}, and the main current vectors are aligned to within 5°. Slight tilting of the current directions corresponds to the tilting of the local magnetopause direction. The current is also measured in a train of FTE (flux transfer event) signatures, associated with the occurrence of extensive reconnection during the event [*Phan et al.*, 2004; *Pu et al.*, 2005]. The mean current for this interval containing the FTEs is $\sim$1 nA m^{-2}, along the mean flux tube direction.

In another event, on the dawn flank magnetosheath, a series of surface ripples resulted in two distinct boundary orientations and the estimated direction of the current maintained its alignment to these magnetopause orientations. Figure 2.1 shows the curlometer results for this pass, together with simultaneous estimates of $\nabla \cdot \boldsymbol{B}$. Note the pronounced current peaks at the times of the magnetopause crossings, identified by the vertical dashed lines.

A third event showed small amplitude ($<$1 R$_E$), inward and outward motions of the magnetopause, resulting in both slow and fast crossings. Using both the Curlometer and the discontinuity analysis, first applied by [*Dunlop et al.*, 2002a] the thickness of the current layer (ΔD) can be used to compute an average current density in the magnetopause from $\Delta \boldsymbol{B}/\Delta D$, and compared to $\mu_0|\boldsymbol{j}|$. For a number of magnetopause crossings, they agree to within 15% (worst case).

2.3 Magnetotail studies

The Curlometer has also been extensively applied to the magnetotail current sheet. The Curlometer can reproduce the cross-tail current and also suggests the existence of field-aligned currents, often correlating with the field aligned and trapped energetic electron populations. In fact several authors have applied the technique as part of investigations

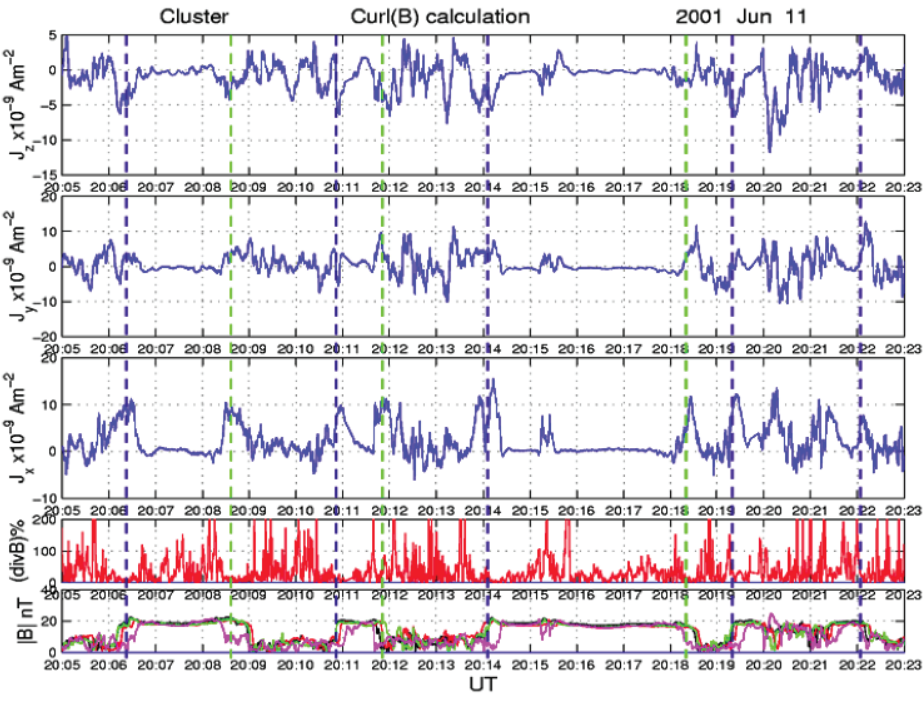

Figure 2.1: Plot of the curlometer estimate of the electric current (top three panels); estimate of $\nabla \cdot \boldsymbol{B}$, scaled to $|\nabla \times \boldsymbol{B}|$; and the field magnitude, B, measured by the four Cluster spacecraft. From *Dunlop and Balogh* [2005].

into the properties of the magnetotail current sheet. It has been used in many studies investigating the basic structure of the magnetotail [*Shen et al.*, 2003; *Thompson et al.*, 2005; *Runov et al.*, 2005b, 2006a, b; *Thompson et al.*, 2006]. It has been employed in studies of dynamic behaviour such as magnetotail flapping [*Volwerk et al.*, 2003; *Runov et al.*, 2005a; *Sergeev et al.*, 2006], wave activity [*Takada et al.*, 2006], substorm activity [*Kivelson et al.*, 2005], and near-Earth flow shears at the PSBL [*Nakamura et al.*, 2004].

The technique has also been applied to the study of magnetotail current sheet reconnection sites [*Runov et al.*, 2003; *Henderson et al.*, 2006a; *Lui et al.*, 2006; *Nakamura et al.*, 2006; *Xiao et al.*, 2006; *Laitinen et al.*, 2007; *Lui et al.*, 2007]. In particular, it has been used to examine the $\boldsymbol{j} \times \boldsymbol{B}$ term in the generalised Ohm's law and thus identify encounters with the ion diffusion region, where the ion plasma is not frozen to the magnetic field. The Curlometer has also been employed to examine the extent to which magnetotail flux ropes are force-free [*Slavin et al.*, 2003; *Henderson et al.*, 2006b; *Amm et al.*, 2006; *Eastwood et al.*, 2006], as well as to study the connection of the magnetotail to the ionosphere via field aligned currents [*Amm et al.*, 2005; *Cheng et al.*, 2007], including calculation of the Joule term $\boldsymbol{E} \cdot \boldsymbol{j}$ [*Marghitu et al.*, 2006; *Hamrin et al.*, 2006].

2.4 Curlometer for other structures

The Curlometer has been used to measure the current density across the Heliospheric Current Sheet [*Eastwood et al.*, 2002], the current density in the ring current [*Vallat et al.*, 2005] and to measure spatial gradients in the plasmasphere [*Darrouzet et al.*, 2006; *De Keyser et al.*, 2007]. It has also allowed study of the contributions to the cross shock electric field at the quasi-perpendicular bow shock [*Eastwood et al.*, 2007].

A large number of magnetopause FTE signatures have been analysed and usually are found to contain an axially aligned current signature and an enhanced flux of out-flowing energetic ions [e.g., *Pu et al.*, 2005]. The axis and motion of the implied flux tubes can also be found by minimisation of the current density [*Xiao et al.*, 2004b], by employing the condition that $\nabla \cdot (\nabla \times \boldsymbol{B}) = 0$. All these FTEs are consistent with northward moving flux tubes with similar alignments. Large scale FTEs can provide the current profile which has been shown to suggest that the main current is consistent with a force free current structure. Cusp current signatures are seen at both the inner and outer cusp boundaries [*Dunlop and Balogh*, 2005].

The properties of the magnetospheric ring current have also been monitored using the Curlometer technique [*Vallat et al.*, 2005]. These results show that an azimuthal (westward) current is maintained at the equator which evolves into a field aligned current at the plasma sheet boundary. The signatures are limited by the spacecraft configuration, but give good estimates for the current components perpendicular to the background field. A statistical study has also been performed and this gives a clear confirmation of the ring current extending over different latitudes.

2.5 Other gradient analyses

One important feature of the Curlometer analysis is that it provides an estimate point by point in time and therefore accesses the temporal evolution of the current structure. If the properties of the data are stationary in the sense that this observed time dependence represents a convective evolution relative to the spacecraft, the spatial form of the current structure is well resolved by the observations. The Curlometer measurement, however, represents the combination of spatial gradients across the four spacecraft (to provide an average of the electric current density). Individual spacecraft have different locations within the current structure so that the interpretation of this average depends upon the temporal nature as much as on the relative spatial extent. Linear estimates of the spatial gradients can be combined into a variety of other quantities which can form other gradient based methods which are also dependent on the temporal interpretation. For example, gradient analysis has also been applied to other quantities, such as the plasma density [*Darrouzet et al.*, 2004].

A recent, generalised gradient method, also based on least squares optimisation has been introduced by *De Keyser et al.* [2007]. The method does not limit itself to four spacecraft, but is designed to also obtain scalar gradients with fewer than four spacecraft, for example, and performs a self diagnosis to check applicability. The validity of the classical gradient computation depends on the requirement that the four measurement points are sufficiently close to each other in space so that the spatial gradient can be taken constant over the spacecraft configuration. The least squares gradient computation discussed

by *De Keyser et al.* is based on homogeneity in space-time: It collects all measurement points in a region in space and time in which the gradient is essentially constant to build an over-determined system of equations for the spatial and temporal gradients. This system is solved in a weighted least-squares sense, with the weights being the inverse of the estimated total error on the measurements. This approach exploits the information content in the data in an optimal way. The algorithm provides total error estimates on the computed gradient, including the effects of measurement errors and the errors due to deviations from spatio-temporal homogeneity. It also has the ability to diagnose the conditioning of the problem. The algorithm can be applied to both scalar and vector fields. It thus can be used to construct a new version of the curlometer, in particular by explicitly incorporating the additional constraint of vanishing magnetic field divergence. While the generalised algorithm is computationally more expensive, it provides total error estimates on the gradient, which the classical algorithm cannot. A particular advantage is that it may be applied in situations with less than 4 instruments (e.g. using measurements along the separation directions of 3 spacecraft plus along the orbit direction, or by incorporating geometrical constraints) or with more than 4 spacecraft. It is obvious that the generalised method effectively reduces to the classical algorithm if the homogeneity time scale is very short. The least-squares method therefore is useful especially when the time variations are not too rapid, for instance for the computation of gradients in the plasmasphere.

We also highlight a simple gradient based method called the Minimum Directional Derivative method [MDD—see *Shi et al.*, 2005], which is based on a principal value decomposition (diagonalisation) of the symmetric matrix, $\mathsf{L} = (\nabla \boldsymbol{B})(\nabla \boldsymbol{B})^T$, where $\nabla \boldsymbol{B}$ is the dyadic of the magnetic field vector $\boldsymbol{B}$. The analysis returns the maximum, intermediate and minimum eigenvalues (λ_1, λ_2, λ_3) and associated eigenvectors ($\hat{\boldsymbol{n}}_1$, $\hat{\boldsymbol{n}}_2$, $\hat{\boldsymbol{n}}_3$), and the separation of the eigenvalues defines the dimensionality of the structure. For example, when the maximum eigenvalue is large compared to the others, the structure is a 1-D boundary. A related method calculates the associated orientation and motion of the structure [*Shi et al.*, 2006] via the convective equation, $D\boldsymbol{B}/Dt + \boldsymbol{V}_{str} \cdot \nabla \boldsymbol{B} = 0$. The normals and velocity have been shown to agree well with estimates from other boundary analysis.

In addition, since the launch of Cluster, several researchers have further developed the curlometer technique, for example applying MVA analysis to the current density time series at the magnetopause [*Haaland et al.*, 2004] and inside magnetopause flux rope FTEs [*Xiao et al.*, 2004b; *Zhou et al.*, 2006]. It has also been summarised in more recent reviews [*Pu et al.*, 2005; *Dunlop and Balogh*, 2005; *van Allen*, 2006]. The review by van Allen was published in the American Journal of Physics, a journal intended to aid the education of students and physics teachers by bringing contemporary research into the classroom. Sadly this was his last article, published posthumously.

2.6 Conclusions

The magnetic field measurements on Cluster can produce a realistic determination of the electric current density at the magnetopause, even where the scale size of the Cluster configuration approaches that of the current layer thickness. The current directions can be shown to lie in the plane of the magnetopause boundary, even during times of induced motion and large-scale surface ripples. These results have depended upon first accurately determining the orientation and thickness of the current layer, using discontinuity analysis

in combination with the curlometer estimate of $\nabla \times \boldsymbol{B}$. The current profiles have been shown to compare well to the mean current defined by the overall magnetic shear across the boundary layer.

Knowledge of boundary orientation and motion in principle allows a mapping of time to spatial location in the current layer (through $\delta x = v_n \delta t$, if x lies along the boundary normal). This allows the current density to be compared to the magnetic field change with distance through the layer and the change in the magnetic field component with time can therefore often be related to distance through the boundary layer, and hence to the current profile (since $v_n \mu_0 |\boldsymbol{j}| = \delta \boldsymbol{B}/\delta t$).

Other applications of the Curlometer, to flux tubes represented by FTEs, to the magnetotail, cusp, and bow shock, and also to the plasma sphere and ring current, have been briefly reviewed here. These results all indicate that a very wide application of the Curlometer to provide meaningful results is possible. We have also highlighted some other recent gradient-based methods which give results which compare well with other methods.

Acknowledgements

The work by M.W.D. is supported by the Science and Technology Facilities Council Rolling Grants, that by J.P.E. by NASA grant NNX07AF32G.

Bibliography

Amm, O., Donovan, E. F., Frey, H., Lester, M., Nakamura, R., Wild, J. A., Aikio, A., Dunlop, M., Kauristie, K., Marchaudon, A., McCrea, I. W., Opgenoorth, H. J., and Stromme, A., 2005, Coordinated studies of the geospace environment using Cluster, satellite and ground-based data: an interim review, *Ann. Geophys.*, **23**, 2129–2170, http://www.ann-geophys.net/23/2129/2005/.

Amm, O., Nakamura, R., Frey, H. U., Ogawa, Y., Kubyshkina, M., Balogh, A., and Rème, H., 2006, Substorm topology in the ionosphere and magnetosphere during a flux rope event in the magnetotail, *Ann. Geophys.*, **24**, 735–750, http://www.ann-geophys.net/24/735/2006/.

Cheng, Z.-W., Shi, J.-K., Zhang, T.-L., and Liu, Z.-X., 2007, Probability of Field-Aligned Currents Observed by the Satellite Cluster in the Magnetotail, *Chinese Physics Letter*, **24**, 1125–1127, doi:10.1088/0256-307X/24/4/076.

Darrouzet, F., Décréau, P., De Keyser, J., Masson, A., Gallagher, D., Santolik, O., Sandel, B., Trotignon, J., Rauch, J., Le Guirriec, E., Canu, P., Sedgemore, F., André, M., and Lemaire, J., 2004, Density structures inside the plasmasphere: Cluster observations, *Ann. Geophys.*, **22**, 2577–2585, http://www.ann-geophys.net/22/2577/2004/.

Darrouzet, F., De Keyser, J., Décréau, P. M. E., Lemaire, J. F., and Dunlop, M. W., 2006, Spatial gradients in the plasmasphere from Cluster, *Geophys. Res. Lett.*, **33**, L08105, doi:10.1029/2006GL025727.

De Keyser, J., Dunlop, M. W., Owen, C. J., Sonnerup, B. U. Ö., Haaland, S. E., Vaivads, A., Paschmann, G., Lundin, R., and Rezeau, L., 2005, Magnetopause and Boundary Layer, *Space Sci. Rev.*, **118**, 231–320, doi:10.1007/s11214-005-3834-1.

De Keyser, J., Darrouzet, E., Dunlop, M. W., and Décréau, P. M. E., 2007, Least-squares gradient calculation from multi-point observations of scalar and vector fields: methodology and applications with Cluster in the plasmasphere, *Ann. Geophys.*, **25**, 971–987, http://www.ann-geophys.net/25/971/2007/.

Dunlop, M. W. and Balogh, A., 2005, Magnetopause current as seen by Cluster, *Ann. Geophys.*, **23**, 901–907, http://www.ann-geophys.net/23/901/2005/.

Dunlop, M. W., Southwood, D. J., Glassmeier, K.-H., and Neubauer, F. M., 1988, Analysis of Multipoint Magnetometer Data, *Adv. Space Res.*, **8**, (9)273–(9)277.

Dunlop, M. W., Balogh, A., and Glassmeier, K.-H., 2002a, Four-point Cluster application of magnetic field analysis tools: The discontinuity analyzer, *J. Geophys. Res.*, **107**, 1385, doi:10.1029/2001JA005089.

Dunlop, M. W., Balogh, A., Glassmeier, K. H., and Robert, P., 2002b, Four-point Cluster application of magnetic field analysis tools: The Curlometer, *J. Geophys. Res.*, **107**, 1384, doi:10.1029/2001JA005088.

Eastwood, J. P., Balogh, A., Dunlop, M. W., and Smith, C. W., 2002, Cluster observations of the heliospheric current sheet and an associated magnetic flux rope and comparisons with ACE, *J. Geophys. Res.*, **107**, 1365, doi:10.1029/2001JA009158.

Eastwood, J. P., Sibeck, D. G., Slavin, J. A., Lavraud, B., Lucek, E. A., Balogh, A., and Dandouras, I., 2006, Observations of flux ropes and X-lines in the near Earth magnetotail, in *Proceedings Cluster and Double Star Symposium—5th Anniversary of Cluster in Space*, edited by K. Fletcher, ESA SP-598, ESA Publ. Div., Noordwijk, Netherlands.

Eastwood, J. P., Bale, S. D., Mozer, F. S., and Hull, A. J., 2007, Contributions to the cross shock electric field at a quasiperpendicular collisionless shock, *Geophys. Res. Lett.*, **34**, L17104, doi:10.1029/2007GL03610.

Haaland, S., Sonnerup, B. U. O., Dunlop, M. W., Georgescu, E., Paschmann, G., Klecker, B., and Vaivads, A., 2004, Orientation and motion of a discontinuity from Cluster curlometer capability: Minimum variance of current density, *Geophys. Res. Lett.*, **31**, L10804, doi:10.1029/2004GL02001.

Hamrin, M., Marghitu, O., Ronnmark, K., Klecker, B., André, M., Buchert, S., Kistler, L. M., McFadden, J., Rème, H., and Vaivads, A., 2006, Observations of concentrated generator regions in the nightside magnetosphere by Cluster/FAST conjunctions, *Ann. Geophys.*, **24**, 637–649, http://www.ann-geophys.net/24/637/2006/.

Henderson, P. D., Owen, C. J., Alexeev, I. V., Slavin, J., Fazakerley, A. N., Lucek, E., and Rème, H., 2006a, Cluster observations of flux rope structures in the near-tail, *Ann. Geophys.*, **24**, 651–666, http://www.ann-geophys.net/24/651/2006/.

Henderson, P. D., Owen, C. J., Lahiff, A. D., Alexeev, I. V., Fazakerley, A. N., Lucek, E., and Rème, H., 2006b, Cluster PEACE observations of electron pressure tensor divergence in the magnetotail, *Geophys. Res. Lett.*, **33**, L22106, doi:10.1029/2006GL027868.

Khotyaintsev, Y., Vaivads, A., Ogawa, Y., Popielawska, B., André, M., Buchert, S., Décréau, P., Lavraud, B., and Rème, H., 2004, Cluster observations of high-frequency waves in the exterior cusp, *Ann. Geophys.*, **22**, 2403–2411, http://www.ann-geophys.net/22/2403/2004/.

Kivelson, M. G., McPherron, R. L., Thompson, S., Khurana, K. K., Weygand, J. M., and Balogh, A., 2005, The response of the near earth magnetotail to substorm activity, *Adv. Space Res.*, **36**, 1818–1824, doi:10.1016/j.asr.2004.03.024.

Laitinen, T. V., Nakamura, R., Runov, A., Rème, H., and Lucek, E. A., 2007, Global and local disturbances in the magnetotail during reconnection, *Ann. Geophys.*, **25**, 1025–1035, http://www.ann-geophys.net/25/1025/2007/.

Lui, A. T. Y., Zheng, Y., Zhang, Y., Livi, S., Rème, H., Dunlop, M. W., Gustafsson, G., Mende, S. B., Mouikis, C., and Kistler, L. M., 2006, Cluster observation of plasma flow reversal in the magnetotail during a substorm, *Ann. Geophys.*, **24**, 2005–2013, http://www.ann-geophys.net/24/2005/2006/.

Lui, A. T. Y., Zheng, Y., Rème, H., Dunlop, M. W., Gustafsson, G., and Owen, C. J., 2007, Breakdown of the frozen-in condition in the Earth's magnetotail, *J. Geophys. Res.*, **112**, A04215, doi:10.1029/2006JA012000.

Marghitu, O., Hamrin, M., Klecker, B., Vaivads, A., McFadden, J., Buchert, S., Kistler, L. M., Dandouras, I., André, M., and Rème, H., 2006, Experimental investigation of auroral generator regions with conjugate Cluster and FAST data, *Ann. Geophys.*, **24**, 619–635, http://www.ann-geophys.net/24/619/2006/.

Maynard, N. C., 2005, Coupling the solar-wind/IMF to the ionosphere through the high latitude cusps, *Surveys in Geophys.*, **26**, 255–280.

Maynard, N. C., Ober, D. M., Burke, W. J., Scudder, J. D., Lester, M., Dunlop, M., Wild, J. A., Grocott, A., Farrugia, C. J., Lund, E. J., Russell, C. T., Weimer, D. R., Siebert, K. D., Balogh, A., André, M., and Rème, H., 2003, Polar, Cluster and SuperDARN evidence for high-latitude merging during southward IMF: temporal/spatial evolution, *Ann. Geophys.*, **21**, 2233–2258, http://www.ann-geophys.net/21/2233/2003/.

Nakamura, R., Baumjohann, W., Nagai, T., Fujimoto, M., Mukai, T., Klecker, B., Treumann, R., Balogh, A., Rème, H., Sauvaud, J. A., Kistler, L., Mouikis, C., Owen, C. J., Fazakerley, A. N., Dewhurst, J. P., and Bogdanova, Y., 2004, Flow shear near the boundary of the plasma sheet observed by Cluster and Geotail, *J. Geophys. Res.*, **109**, A05204, doi:10.1029/2003JA010174.

Nakamura, R., Baumjohann, W., Asano, Y., Runov, A., Balogh, A., Owen, C. J., Fazakerley, A. N., Fujimoto, M., Klecker, B., and Rème, H., 2006, Dynamics of thin current sheets associated with magnetotail reconnection, *J. Geophys. Res.*, **111**, A11206, doi:10.1029/2006JA011706.

Panov, E. V., Buchner, J., Franz, M., Korth, A., Khotyaintsev, Y., Nikutowski, B., Savin, S., Fornacon, K. H., Dandouras, I., and Rème, H., 2006a, CLUSTER spacecraft observation of a thin current sheet at the Earth's magnetopause, *Adv. Space Res.*, **37**, 1363–1372, doi:10.1016/j.asr.2005.08.024.

Panov, E. V., Buchner, J., Franz, M., Korth, A., Savin, S. P., Fornacon, K. H., Dandouras, I., and Rème, H., 2006b, CLUSTER observation of collisionless transport at the magnetopause, *Geophys. Res. Lett.*, **33**, L15109, doi:

10.1029/2006GL026556.

Phan, T. D., Dunlop, M. W., Paschmann, G., Klecker, B., Bosqued, J. M., Rème, H., Balogh, A., Twitty, C., Mozer, F. S., Carlson, C. W., Mouikis, C., and Kistler, L. M., 2004, Cluster observations of continuous reconnection at the magnetopause under steady interplanetary magnetic field conditions, *Ann. Geophys.*, **22**, 2355–2367, http://www.ann-geophys.net/22/2355/2004/.

Pu, Z. Y., Zong, Q. G., Fritz, T. A., Xiao, C. J., Huang, Z. U., Fu, S. U., Shi, Q. Q., Dunlop, M. W., Glassmeier, K. H., Balogh, A., Daly, P., Rème, H., Dandouras, J., Cao, J. B., Liu, Z. X., Shen, C., and Shi, J. K., 2005, Multiple flux rope events at the high-latitude magnetopause: Cluster/RAPID observation on 26 January, 2001, *Surveys in Geophys.*, **26**, 193–214.

Runov, A., Nakamura, R., Baumjohann, W., Treumann, R. A., Zhang, T. L., Volwerk, M., Voros, Z., Balogh, A., Glassmeier, K. H., Klecker, B., Rème, H., and Kistler, L., 2003, Current sheet structure near magnetic X-line observed by Cluster, *Geophys. Res. Lett.*, **30**, 1579, doi:10.1029/2002GL016730.

Runov, A., Sergeev, V. A., Baumjohann, W., Nakamura, R., Apatenkov, S., Asano, Y., Volwerk, M., Voros, Z., Zhang, T. L., Petrukovich, A., Balogh, A., Sauvaud, J. A., Klecker, B., and Rème, H., 2005a, Electric current and magnetic field geometry in flapping magnetotail current sheets, *Ann. Geophys.*, **23**, 1391–1403, http://www.ann-geophys.net/23/1391/2005/.

Runov, A., Sergeev, V. A., Nakamura, R., Baumjohann, W., Zhang, T. L., Asano, Y., Volwerk, M., Voros, Z., Balogh, A., and Rème, H., 2005b, Reconstruction of the magnetotail current sheet structure using multi-point Cluster measurements, *Planet. Space Sci.*, **53**, 237–243, doi:10.1016/j.pss.2004.09.049.

Runov, A., Nakamura, R., and Baumjohann, W., 2006a, Multi-point study of the magnetotail current sheet, *Adv. Space Res.*, **38**, 85–92, doi:10.1016/j.asr.2004.09.024.

Runov, A., Sergeev, V. A., Nakamura, R., Baumjohann, W., Apatenkov, S., Asano, Y., Takada, T., Volwerk, M., Voros, Z., Zhang, T. L., Sauvaud, J. A., Rème, H., and Balogh, A., 2006b, Local structure of the magnetotail current sheet: 2001 Cluster observations, *Ann. Geophys.*, **24**, 247–262, http://www.ann-geophys.net/24/247/2006/.

Sergeev, V. A., Sormakov, D. A., Apatenkov, S. V., Baumjohann, W., Nakamura, R., Runov, A. V., Mukai, T., and Nagai, T., 2006, Survey of large-amplitude flapping motions in the midtail current sheet, *Ann. Geophys.*, **24**, 2015–2024, http://www.ann-geophys.net/24/2015/2006/.

Shen, C., Li, X., Dunlop, M., Liu, Z. X., Balogh, A., Baker, D. N., Hapgood, M., and Wang, X., 2003, Analyses on the geometrical structure of magnetic field in the current sheet based on cluster measurements, *J. Geophys. Res.*, **108**, 1168, doi:10.1029/2002JA009612.

Shi, Q. Q., Shen, C., Pu, Z. Y., Dunlop, M. W., Zong, Q. G., Zhang, H., Xiao, C. J., Liu, Z. X., and Balogh, A., 2005, Dimensional analysis of observed structures using multipoint magnetic field measurements: Application to Cluster, *Geophys. Res. Lett.*, **32**, L12105, doi:10.1029/2005GL022454.

Shi, Q. Q., Shen, C., Dunlop, M. W., Pu, Z. Y., Zong, Q.-G., Liu, Z. X., Lucek, E., and Balogh, A., 2006, Motion of observed structures calculated from multi-point magnetic field measurements: Application to Cluster, *Geophys. Res. Lett.*, **33**, L08109, doi:10.1029/2005GL025073.

Slavin, J. A., Lepping, R. P., Gjerloev, J., Goldstein, M. L., Fairfield, D. H., Acuna, M. H., Balogh, A., Dunlop, M., Kivelson, M. G., Khurana, K., Fazakerley, A., Owen, C. J., Rème, H., and Bosqued, J. M., 2003, Cluster electric current density measurements within a magnetic flux rope in the plasma sheet, *Geophys. Res. Lett.*, **30**, 1362, doi:10.1029/2002GL016411.

Takada, T., Nakamura, R., Baumjohann, W., Seki, K., Voros, Z., Asano, Y., Volwerk, M., Runov, A., Zhang, T. L., Balogh, A., Paschmann, G., Torbert, R. B., Klecker, B., Rème, H., Puhl-Quinn, P., Canu, P., and Décréau, P. M. E., 2006, Alfven waves in the near-PSBL lobe: Cluster observations, *Ann. Geophys.*, **24**, 1001–1013, http://www.ann-geophys.net/24/1001/2006/.

Thompson, S. M., Kivelson, M. G., Khurana, K. K., Balogh, A., Rème, H., Fazakerley, A. N., and Kistler, L. M., 2004, Cluster observations of quasi-periodic impulsive signatures in the dayside northern lobe: High-latitude flux transfer events?, *J. Geophys. Res.*, **109**, A02213, doi:10.1029/2003JA010138.

Thompson, S. M., Kivelson, M. G., Khurana, K. K., McPherron, R. L., Weygand, J. M., Balogh, A., Rème, H., and Kistler, L. M., 2005, Dynamic Harris current sheet thickness from Cluster current density and plasma measurements, *J. Geophys. Res.*, **110**, A02212, doi:10.1029/2004JA010714.

Thompson, S. M., Kivelson, M. G., El Alaoui, M., Balogh, A., Rème, H., and Kistler, L. M., 2006, Bifurcated current sheets: Statistics from Cluster magnetometer measurements, *J. Geophys. Res.*, **111**, A03212, doi:10.1029/2005JA011009.

Vallat, C., Dandouras, I., Dunlop, M., Balogh, A., Lucek, E., Parks, G. K., Wilber, M., Roelof, E. C., Chanteur, G., and Rème, H., 2005, First current density measurements in the ring current region using simultaneous multi-spacecraft CLUSTER-FGM data, *Ann. Geophys.*, **23**, 1849–1865, http://www.ann-geophys.net/23/1849/2005/.

van Allen, J. A., 2006, Inference of magnetospheric currents from multipoint magnetic field measurements, *Amer.*

J. Phys., **74**, 809–814.

van Allen, J. A. and Adnan, J., 1992, Observed currents on the earth's high-latitude magnetopause, *J. Geophys. Res.*, **97**, 6381–6395.

Volwerk, M., Glassmeier, K. H., Runov, A., Baumjohann, W., Nakamura, R., Zhang, T. L., Klecker, B., Balogh, A., and Rème, H., 2003, Kink mode oscillation of the current sheet, *Geophys. Res. Lett.*, **30**, 1320, doi: 10.1029/2002GL016467.

Xiao, C. J., Pu, Z. Y., Huang, Z. Y., Fu, S. Y., Xie, L., Zong, Q. G., Fritz, T., Glassmeier, K. H., Liu, Z. X., Cao, J. B., Shi, J. K., Shen, C., Lu, L., Wang, N. Q., and Chen, T., 2004a, Multiple flux rope events at the high-latitude magnetopause on January 26, 2001: Current density calculating, *Chinese J. Geophys.*, **47**, 555–561.

Xiao, C. J., Pu, Z. Y., Ma, Z. W., Fu, S. Y., Huang, Z. Y., and Zong, Q. G., 2004b, Inferring of flux rope orientation with the minimum variance analysis technique, *J. Geophys. Res.*, **109**, A11218, doi:10.1029/2004JA010594.

Xiao, C. J., Wang, X. G., Pu, Z. Y., Zhao, H., Wang, J. X., Ma, Z. W., Fu, S. Y., Kivelson, M. G., Liu, Z. X., Zong, Q. G., Glassmeier, K. H., Balogh, A., Korth, A., Rème, H., and Escoubet, C. P., 2006, In situ evidence for the structure of the magnetic null in a 3D reconnection event in the Earth's magnetotail, *Nature Physics*, **2**, 478–483.

Zhou, X. Z., Zong, Q. G., Pu, Z. Y., Fritz, T. A., Dunlop, M. W., Shi, Q. Q., Wang, J., and Wei, Y., 2006, Multiple Triangulation Analysis: another approach to determine the orientation of magnetic flux ropes, *Ann. Geophys.*, **24**, 1759–1765, http://www.ann-geophys.net/24/1759/2006/.

Zuo, P. B., Liu, S. L., Jin, S. P., Liu, Z. X., and Shi, J. K., 2004, A study of the characteristics for the magnetic flux transfer events occurred on March 2, 2001, *Chinese J. Geophys.*, **47**, 376–384.

— 3 —

Geometrical Structure Analysis of the Magnetic Field

CHAO SHEN
Centre for Space Science and Applied Research
Chinese Academy of Sciences
Beijing, China

MALCOLM W. DUNLOP
Rutherford Appleton Laboratory
Chilton, Didcot, United Kingdom

The geometrical configuration of the magnetic field underpins important research topics in magnetospheric physics. The magnetic field is the skeleton of the magnetosphere and plays a crucial role in determining the plasma distribution of particles, the occurrences of various macro and micro instabilities, the triggering and evolution of substorms and magnetic storms, etc. On the other hand, the magnetic reconnection process at the magnetopause and in the tail plasma sheet alters the topological structures of the magnetosphere, producing transient magnetic structures, such as rotational discontinuities, flux ropes, plasmoids, etc. The magnetometer investigation on the multiple spacecraft Cluster mission has made it possible to reveal the three-dimensional geometrical structure of the magnetic field in the magnetosphere, at least to local first order gradients. To achieve a full analysis of the local nature of the magnetic field geometry, several new gradient and curvature based methods have been proposed to describe the topological configurations of the key regions of magnetosphere. These methods are the curvature analysis method [*Shen et al.*, 2003], magnetic field strength gradient method [*Shen et al.*, 2003, 2007a], and the magnetic rotation analysis [MRA, see *Shen et al.*, 2007b]. In this chapter, we give a summary of the development of these new approaches.

3.1 Curvature analysis

In order to clarify the topological configuration of the magnetic structures in the magnetosphere, *Shen et al.* [2003] first used the curvature analysis method to describe the local geometrical features of the magnetic field lines (MFLs) including the curvature, the radius of curvature, and the binormal. The curvature of the MFLs can be expressed as *Shen et al.* [2003]

$$\boldsymbol{\rho}_c = (\boldsymbol{b}\cdot\nabla\boldsymbol{b}) = B^{-2}B_i\nabla_i B_j - B^{-4}B_j B_i B_l \nabla_i B_l \tag{3.1}$$

where $\hat{\boldsymbol{b}}$ is the unit vector of the magnetic field $\boldsymbol{B}$, $\hat{\boldsymbol{b}} = \boldsymbol{B}/B$; the indices i, j and l (=1, 2, and 3) denote the three components (x, y, and z) and $B = |\boldsymbol{B}|$. Obviously, $\boldsymbol{\rho}_c$ is normal to

the unit vector $\hat{\boldsymbol{b}}$. The normal $\hat{\boldsymbol{N}}$ of osculating plane of the MFLs is defined as

$$\hat{\boldsymbol{N}} = \frac{\hat{\boldsymbol{b}} \times \boldsymbol{\rho}_c}{\left|\hat{\boldsymbol{b}} \times \boldsymbol{\rho}_c\right|} \tag{3.2}$$

$\hat{\boldsymbol{N}}$ is also called the binormal of the MFLs.

The curvature of the magnetic field lines can be determined by Eqn. 3.1 if the gradient of the magnetic field $\nabla \boldsymbol{B}$ can be calculated with the four-point magnetic measurements of Cluster with the approach described in Chapters 12 [*Harvey*, 1998] or 14 [*Chanteur*, 1998] of ISSI SR-001. The curvature radius R_c is just $1/\rho_c$. Finally, we may further determine the binormal $\hat{\boldsymbol{N}}$ of the magnetic field lines with Eqn. 3.2. Therefore, with four-point spacecraft magnetic measurements, we can get the curvature vector $\boldsymbol{\rho}_c$, the curvature radius R_c and the binormal $\hat{\boldsymbol{N}}$ of the magnetic field lines. In addition, the local natural coordinates $[\hat{\boldsymbol{b}}, \hat{\boldsymbol{\rho}}_c, \hat{\boldsymbol{N}}]$, into which the physical vector quantities, for example current density can be projected, are readily obtained. Here $\hat{\boldsymbol{\rho}}_c = \boldsymbol{\rho}_c/|\boldsymbol{\rho}_c|$.

Curvature analysis has been successfully applied to investigate the geometrical configuration and topological structures of the tail current sheet, magnetic reconnection, flux ropes and the cusp [*Shen et al.*, 2003, 2007c; *Runov et al.*, 2003, 2005].

For a discussion of magnetic curvature analysis, see also Chapter 4.

3.2 Magnetic field strength gradient

This method has been developed in order to obtain the normal to one-dimensional magnetic structures, such as the shock front, tail current sheet, and boundary layer [*Shen et al.*, 2003, 2007a].

The normal $\hat{\boldsymbol{n}}$ of one-dimensional magnetic structures can be regarded as a parallel to the gradient of the magnetic pressure p_B or the magnetic field strength [*Shen et al.*, 2003], i.e.

$$\hat{\boldsymbol{n}} = -\nabla p_B / |\nabla p_B| = -\nabla B / |\nabla B| = -B_j \nabla B_j / \left|B_j \nabla B_j\right| \tag{3.3}$$

In addition, the width W of the 1-D magnetic structures may be calculated by [*Shen et al.*, 2007c]

$$W = \int_0^W \mathrm{d}Z = \int_{B1}^{B2} \mathrm{d}B/|\nabla B| \approx (B_2 - B_1)/\langle|\nabla B|\rangle \tag{3.4}$$

where B_1 and B_2 are the magnetic field strengths at the two boundaries of the 1-D structures and $\langle|\nabla B|\rangle$is the average of $|\nabla B|$.

∇B, deduced from the measurements from Cluster, may also be used to determine the B contours in the magnetosphere.

This method has been very successful for determining the normal to the tail current sheet, and it has been shown that the gradient of the magnetic strength reverses its direction during crossings of the centre of the current sheet [*Shen et al.*, 2003, 2007b]. It has also been applied to determine the normal to the bow shock, and the deduced shape of the bow shock resulting from this analysis is consistent with the standard shock model [*Shen et al.*, 2007a].

3.3 Magnetic rotation analysis

Shen et al. [2007b] have developed the magnetic rotation analysis (MRA) approach with the purpose of revealing the three-dimensional features of the spatial rotation of the magnetic vector. The square of the spatial rotation rate of $\hat{\boldsymbol{b}}$ along an arbitrary direction $\hat{\boldsymbol{e}}$ is [*Shen et al.*, 2007b]

$$I^{(e)} = \left|(\hat{\boldsymbol{e}} \cdot \nabla)\hat{\boldsymbol{b}}\right|^2 = e_i e_j S_{ij} \tag{3.5}$$

where the magnetic rotation tensor $\mathsf{S}_{ij} = \nabla_i b_l \, \nabla_j b_l$. Assuming that the symmetrical tensor S_{ij} has three eigenvectors, $\hat{\boldsymbol{e}}^{(1)}$, $\hat{\boldsymbol{e}}^{(2)}$, $\hat{\boldsymbol{e}}^{(3)}$ and three corresponding eigenvalues, μ_1, μ_2 and μ_3 with $\mu_1 \geq \mu_2 \geq \mu_3 \geq 0$, and the square of the magnetic rotation rate along $\hat{\boldsymbol{e}}$ becomes [*Shen et al.*, 2007b]

$$I^{(e)} = \mu_1(\cos\alpha_1)^2 + \mu_2(\cos\alpha_2)^2 + \mu_3(\cos\alpha_3)^2 \tag{3.6}$$

where α_l is the angle between $\hat{\boldsymbol{e}}$ and base vector $\hat{\boldsymbol{e}}^{(l)}$ (l=1, 2, and 3). Eqn. 3.6 yields $\mu_1 \geq I^{(e)} \geq \mu_3$, so that the magnetic unit vector $\hat{\boldsymbol{b}}$ rotates at the largest rotation rate $\mu_1^{1/2}$ along the direction $\hat{\boldsymbol{e}}^{(1)}$, and at the least rotation $\mu_3^{1/2}$ along the direction $\hat{\boldsymbol{e}}^{(3)}$. (Incidently, it can be shown that $\mu_3 = 0$.)

For a one-dimensional planar boundary layer, as occurs typically in shock fronts or current sheets, the largest magnetic rotation rate is along the normal to the 1-D boundary layers. Thus the first eigenvector $\hat{\boldsymbol{e}}^{(1)}$ is the normal to the 1-D planar boundary layers. For a one-dimensional, axi-symmetrical magnetic structure, such as an ideal flux rope, the magnetic vector has a zero rotation rate along its principal direction, hence the principal axis of an axi-symmetric structure is along the third eigenvector $\hat{\boldsymbol{e}}^{(3)}$.

The curvature of the magnetic field lines, which is just the magnetic rotation rate along $\hat{\boldsymbol{b}}$, can be expressed as

$$\rho_c = \sqrt{I^{(b)}} \tag{3.7}$$

Actual calculations have shown that Eqns. 3.7 and 3.1 yield identical values of the curvature of the magnetic field lines [*Shen et al.*, 2007b]. Moreover, the typical scale of a 1-D neutral sheet may be determined by MRA. The half-thickness h of the neutral sheet is the reciprocal value of the maximum of the largest rotation rate [*Shen et al.*, 2007b], i.e.,

$$h = 1/\mu_{1\,\max}^{1/2} \tag{3.8}$$

MRA can be applied to investigate the geometrical features of various magnetic structures in magnetosphere [*Shen et al.*, 2007b], such as those of the current sheets, rotational discontinuities, flux ropes, magnetic reconnection regions, and cusp, etc. It can not only yield the characteristic directions of a structure, but also deduce its internal, geometrical configuration.

3.4 Errors of the methods

Besides the magnetic measurement error, the main error arises from truncation. Generally, the truncation error of $\nabla \boldsymbol{B}$ or $\nabla \hat{\boldsymbol{b}}$ is at the first order, i.e., at L/D, where L is the

size of the Cluster tetrahedron, and D is the typical spatial scale of the magnetic structure [see Appendix in *Shen et al.*, 2007b]. However, the truncation error of $\nabla \boldsymbol{B}$ or $\nabla \hat{\boldsymbol{b}}$ will disappear if the magnetic field is linearly varying in space.

3.5 Analysis of structures

The main analysis performed so far with these methods has included the topics mentioned briefly above. Below, we quote the key results found, which are based on investigations with the Cluster multi-spacecraft magnetic field measurements.

3.5.1 Bow shock

Shen et al. [2007a] investigated the geometrical configuration of the bow shock, based on the gradient analysis of the magnetic field strength. They find that within the bow shock front there is strong gradient of magnetic field strength having values of about 1000 nT/R_E and with the direction constantly pointing downstream. The normals of a number of bow shock crossings, as determined by Eqn. 3.3, are in agreement with those obtained by the timing algorithm [*Russell et al.*, 1983; *Harvey*, 1998; *Schwartz*, 1998; *Dunlop and Woodward*, 1998], MVA [*Sonnerup and Cahill*, 1967; *Sonnerup and Scheible*, 1998], and the coplanarity theorem method [*Abraham-Shrauner*, 1972; *Seon et al.*, 1996]. They are also found to be consistent with the standard model of the bow shock and appear to be rather more stable to shock structure.

3.5.2 Magnetopause

The shape of the magnetopause, including the cusp, can be determined by analysing the geometrical configuration of the MFLs in the vicinity of the magnetopause. Preliminary analysis suggests that the magnetic field lines bend toward dayside and nightside in the pre-cusp and post-cusp regions, respectively, which confirms the existence of a funnel-like geometry in the cusp region. It is also found that the minimum radius of curvature of the pre- and post-cusp magnetopause at the noon-midnight meridian are both about 2–3 R_E. The curvature radius of the dayside, low latitude magnetopause, however, is found to be less than the geocentric (radial) distance; much less than the conventional expectation.

3.5.3 Magnetotail current sheet

The geometric structures of the tail current sheet have also been analysed with the above-mentioned methods. Based on these geometrical features, the tail current sheets may be divided into three types: the normal current sheet [*Shen et al.*, 2003], the flattened current sheet [*Shen et al.*, 2007c] and the tilted sheet [*Lui et al.*, 1978; *Sergeev et al.*, 2003; *Petrukovich et al.*, 2006]. The normal current sheet is typically observed, in which the MFLs are plane curves with constant binormals parallel to the equatorial plane; the current density is normal to the MFLs and lies along the binormal [*Shen et al.*, 2003]. The flattened current sheet has a strong guide field, or B_y component. In the corresponding neutral sheet, the magnetic field vectors lean towards the equatorial plane and rotate around the normal direction from tailward in the southern hemisphere to earthward in the northern

hemisphere. In the flattened current sheet, the MFLs are spiral-like and not plane curves. The half-width of the corresponding neutral sheet is much less than the minimum radius of curvature of the MFLs and the current density in the neutral sheet is duskward and nearly field-aligned [*Shen et al.*, 2007c]. Finally, for the tilted current sheet, the MFLs slip in the north-south direction, while their shape and orientation are almost the same as those in the normal current sheet. The corresponding normal is directed dawnward or duskward and the current density in the neutral sheet has an apparent field-aligned component. It is found that, during the growth phase of substorms, the magnetic rotation in the neutral sheet grows stronger, while the width of the neutral sheet and the minimum radius of curvature of the MFLs both decrease gradually [*Shen et al.*, 2007c].

3.5.4 Magnetic reconnection

The topological structure of magnetic reconnection and of the corresponding flux ropes has also been investigated. During magnetic reconnection processes in the tail current sheet, there are curvature vector reversals as Cluster crosses the X point [*Runov et al.*, 2003, 2005]. It is also found in one case that, in the tail flattened current sheet, component magnetic reconnection may occur, in which no magnetic null point is observed at all. It may be expected that component magnetic reconnection in the flattened current sheet can lead to the formation of flux ropes where the direction of the guiding field remains unchanged. The features of the configuration of the flux ropes have been revealed with geometrical analysis [*Shen et al.*, 2007b]. The flux ropes are generally composed of two parts: the inner part with rather strong magnetic field and the outer part with spiral MFLs. In the inner part of the flux ropes, the curvature radius of the MFLs is rather large, indicating the MFLs are rather straight and that the magnetic rotation is mainly in the radial direction. In the outer part, the curvature radius of the MFLs is smaller, and the magnetic rotation is mainly at the azimuthal direction. The typical spatial scale of the flux ropes in the near earth region is about 1 R_E.

Acknowledgements

The work by C.S. is supported by the NSFC Grant 40390150, 40674094 and the Hundred Talents Program of CAS. The work by M.W.D. is supported by the Science and Technology Facilities Council Rolling Grants.

Bibliography

Abraham-Shrauner, B., 1972, Determination of magnetohydrodynamic shock normals., *J. Geophys. Res.*, **77**, 736–739.

Chanteur, G., 1998, Spatial Interpolation for Four Spacecraft: Theory, in *Analysis Methods for Multi-Spacecraft Data*, edited by G. Paschmann and P. W. Daly, no. SR-001 in ISSI Scientific Reports, chap. 14, pp. 349–369, ESA Publ. Div., Noordwijk, Netherlands.

Dunlop, M. W. and Woodward, T. I., 1998, Multi-Spacecraft Discontinuity Analysis: Orientation and Motion, in *Analysis Methods for Multi-Spacecraft Data*, edited by G. Paschmann and P. W. Daly, no. SR-001 in ISSI Scientific Reports, chap. 11, pp. 271–305, ESA Publ. Div., Noordwijk, Netherlands.

Harvey, C. C., 1998, Spatial Gradients and the Volumetric Tensor, in *Analysis Methods for Multi-Spacecraft Data*, edited by G. Paschmann and P. W. Daly, no. SR-001 in ISSI Scientific Reports, chap. 12, pp. 307–322, ESA Publ. Div., Noordwijk, Netherlands.

Lui, A. T. Y., Meng, C.-I., and Akasofu, S.-I., 1978, Wavy nature of the magnetotail neutral sheet, *Geophys. Res. Lett.*, **5**, 279–282.

Petrukovich, A. A., Zhang, T. L., Baumjohann, W., Nakamura, R., Runov, A., Balogh, A., and Carr, C., 2006, Oscillatory magnetic flux tube slippage in the plasma sheet, *Ann. Geophys.*, **24**, 1695–1704, http://www.ann-geophys.net/24/1695/2006/.

Runov, A., Nakamura, R., Baumjohann, W., Treumann, R. A., Zhang, T. L., Volwerk, M., Vörös, Z., Balogh, A., Glaßmeier, K.-H., Klecker, B., Rème, H., and Kistler, L., 2003, Current sheet structure near magnetic X-line observed by Cluster, *Geophys. Res. Lett.*, **30**, 1579, doi:10.1029/2002GL016730.

Runov, A., Sergeev, V. A., Baumjohann, W., Nakamura, R., Apatenkov, S., Asano, Y., Volwerk, M., Vörös, Z., Zhang, T. L., Petrukovich, A., Balogh, A., Sauvaud, J.-A., Klecker, B., and Rème, H., 2005, Electric current and magnetic field geometry in flapping magnetotail current sheets, *Ann. Geophys.*, **23**, 1391–1403, http://www.ann-geophys.net/23/1391/2005/.

Russell, C. T., Mellot, M. M., Smith, E. J., and King, J. H., 1983, Multiple spacecraft observations of interplanetary shocks: Four spacecraft determination of shock normals, *J. Geophys. Res.*, **88**, 4739–4748.

Schwartz, S. J., 1998, Shock and Discontinuity Normals, Mach Numbers, and Related Parameters, in *Analysis Methods for Multi-Spacecraft Data*, edited by G. Paschmann and P. W. Daly, no. SR-001 in ISSI Scientific Reports, chap. 10, pp. 249–270, ESA Publ. Div., Noordwijk, Netherlands.

Seon, J., Frank, L. A., Paterson, W. R., Scudder, J. D., Coroniti, F. V., Kokubun, S., and Yamamoto, T., 1996, Observations of ion and electron velocity distributions associated with slow-mode shocks in Earth's distant magnetotail, *J. Geophys. Res.*, **101**, 27 399–27 412, doi:10.1029/96JA02525.

Sergeev, V., Runov, A., Baumjohann, W., Nakamura, R., Zhang, T. L., Volwerk, M., Balogh, A., Rème, H., Sauvaud, J. A., André, M., and Klecker, B., 2003, Current sheet flapping motion and structure observed by Cluster, *Geophys. Res. Lett.*, **30**, 1327, doi:10.1029/2002GL016500.

Shen, C., Li, X., Dunlop, M., Liu, Z. X., Balogh, A., Baker, D. N., Hapgood, M., and Wang, X., 2003, Analyses on the geometrical structure of magnetic field in the current sheet based on cluster measurements, *J. Geophys. Res.*, **108**, 1168, doi:10.1029/2002JA009612.

Shen, C., Dunlop, M., Li, X., Liu, Z. X., Balogh, A., Zhang, T. L., Carr, C. M., Shi, Q. Q., and Chen, Z. Q., 2007a, New approach for determining the normal of the bow shock based on Cluster four-point magnetic field measurements, *J. Geophys. Res.*, **112**, A03201, doi:10.1029/2006JA011699.

Shen, C., Li, X., Dunlop, M., Shi, Q. Q., Liu, Z. X., Lucek, E., and Chen, Z. Q., 2007b, Magnetic field rotation analysis and the applications, *J. Geophys. Res.*, **112**, A06211, doi:10.1029/2005JA011584.

Shen, C., Liu, Z. X., Li, X., Dunlop, M., Lucek, E., Rong, Z. J., Chen, Z. Q., Escoubet, C. P., Malova, H. V., Lui, A. T. Y., Fazakerley, A., Walsh, A. P., and Mouikis, C., 2007c, Flattened current sheet and its evolution in substorms, *J. Geophys. Res.*, **112**, submitted.

Sonnerup, B. U. O. and Cahill, L. J., Jr., 1967, Magnetopause Structure and Attitude from Explorer 12 Observations, *J. Geophys. Res.*, **72**, 171.

Sonnerup, B. U. Ö. and Scheible, M., 1998, Minimum and Maximum Variance Analysis, in *Analysis Methods for Multi-Spacecraft Data*, edited by G. Paschmann and P. W. Daly, no. SR-001 in ISSI Scientific Reports, chap. 8, pp. 185–220, ESA Publ. Div., Noordwijk, Netherlands.

— 4 —

Reciprocal Vectors

JOACHIM VOGT
School of Engineering and Science
Jacobs University Bremen
Bremen, Germany

GÖTZ PASCHMANN
Max-Planck-Institut für extraterrestrische Physik
Garching, Germany

GÉRARD CHANTEUR
CETP/CNRS
Vélizy, France

4.1 Introduction

Reciprocal vectors and barycentric coordinates are well-established concepts in various scientific fields, where lattices and grids are essential, e.g., in solid state physics, crystallography, in the numerical analysis of partial differential equations using finite elements, and also in computer graphics and visualisation. In preparation of the Cluster mission, *Chanteur* [1998] in Chapter 14 of ISSI SR-001 adopted reciprocal vectors to construct estimators for spatial derivatives from four-point measurements, to perform error analysis, and to write down the spatial aliasing condition for four-point wave analysis techniques in a very transparent form. Reciprocal vectors also entered the study on the accuracy of plasma moment derivatives, described in Chapter 17 of ISSI SR-001 [*Vogt and Paschmann*, 1998]. As will be shown below, by using the least squares approach presented in Chapter 12 of ISSI SR-001 [*Harvey*, 1998], reciprocal vectors are a convenient means in discontinuity analysis to express boundary parameters in terms of crossing times.

This chapter is intended to provide a conceptual introduction to reciprocal vectors, and to emphasise their importance for the analysis of data from the Cluster spacecraft mission. It is organised as follows: The crossing times approach to boundary analysis is presented in Section 4.2 as a way to motivate the use of reciprocal vectors; some of their most important properties are briefly addressed in Section 4.3; then Section 4.4 deals with various aspects of the spatial gradient reconstruction problem; magnetic curvature estimation is reviewed in Section 4.5, while Section 4.6 contains a discussion on the errors of boundary analysis and curvature estimation. Finally, in Section 4.7 we suggest a way to generalise the reciprocal vector concept to cases where the number of spacecraft, N, is not four.

4.2 Crossing times in boundary analysis

To determine boundary parameters from a single-spacecraft crossing of a discontinuity, minimum variance analysis is the method of choice. To overcome the inherent

spatio-temporal ambiguity of single-spacecraft measurements, it is assumed that a planar discontinuity is moving at constant speed. A conservation law is used to identify one particular component of a vector-valued variable that should not change across the discontinuity, e.g., the normal component of the magnetic field, or the normal component of the mass flux density vector. In the measurements, this particular component is determined through a minimum variance condition (see Section 1.2).

Multipoint measurements provide additional information for the analysis of discontinuities, namely the *crossing times*. This information can be exploited independently to determine boundary parameters, or combined with the individual minimum variance results (see Section 1.1). Crossing time analysis does not make use of an underlying physical model to identify a special component of vector-valued data, and it works also for scalar data. In practice, it is not straightforward to determine the crossing times directly. Here we emphasise the analysis principle to introduce the set of reciprocal vectors of the Cluster tetrahedron, and adopt the least-squares approach presented by *Harvey* [1998].

A planar discontinuity characterised by the boundary normal unit vector $\hat{\boldsymbol{n}}$ is assumed to move with the speed u parallel to the normal $\hat{\boldsymbol{n}}$. The individual crossings are assumed to occur at times t_α and at locations $\boldsymbol{r}_\alpha$, $\alpha = 1, \ldots, N$, where N is the total number of spacecraft. In the case of Cluster, of course $N = 4$. For convenience, and without loss of generality, we choose the origin of our coordinate system to be the barycentre of the spacecraft array, which implies $\sum_\alpha \boldsymbol{r}_\alpha = 0$.

A least-squares cost function could be formulated in terms of the boundary model parameters $\hat{\boldsymbol{n}}$ and u directly, however, in this case a constraint would have to be added to ensure the normalisation condition $|\hat{\boldsymbol{n}}| = 1$. We avoid this technical difficulty by using the so-called *slowness vector* $\boldsymbol{m} = \hat{\boldsymbol{n}}/u$, and express the mismatch of the planar boundary model prediction with the observed crossing data as follows:

$$S = \sum_\alpha [\boldsymbol{m} \cdot \boldsymbol{r}_\alpha - (t_\alpha - t_0)]^2 \tag{4.1}$$

This expression has to be minimised. *Harvey* [1998] defined $t_0 = \frac{1}{N}\sum_\alpha t_\alpha$ as the time origin, and found

$$\left(\sum_\beta \boldsymbol{r}_\beta \boldsymbol{r}_\beta^\dagger\right) \boldsymbol{m} = \sum_\alpha (t_\alpha - t_0)\boldsymbol{r}_\alpha \quad \Rightarrow \quad \boldsymbol{m} = \left(\sum_\beta \boldsymbol{r}_\beta \boldsymbol{r}_\beta^\dagger\right)^{-1} \sum_\alpha (t_\alpha - t_0)\boldsymbol{r}_\alpha \tag{4.2}$$

for the slowness vector $\boldsymbol{m}$. (Since throughout this chapter we are dealing with real variables only, the hermitian conjugate is identical with the transpose, and thus superscripts $\dagger$ and T have the same meaning here.)

This solution applies to more general N point measurements. The tensor $\sum_\beta \boldsymbol{r}_\beta \boldsymbol{r}_\beta^\dagger$ has to be inverted to determine $\boldsymbol{m}$, and then $u = 1/|\boldsymbol{m}|$ as well as $\hat{\boldsymbol{n}} = \boldsymbol{m}/|\boldsymbol{m}|$ (see also Section 1.1.1). In the case of the Cluster mission, we are dealing with four-point measurements, and the inverse tensor can be written as

$$\left(\sum_\beta \boldsymbol{r}_\beta \boldsymbol{r}_\beta^\dagger\right)^{-1} = \sum_\beta \boldsymbol{k}_\beta \boldsymbol{k}_\beta^\dagger \tag{4.3}$$

(Eqn. 15.2 in Chapter 15 of ISSI SR-001 [*Chanteur and Harvey*, 1998]) where the vectors $\boldsymbol{k}_\beta$, $\beta = 1, 2, 3, 4$ are the reciprocal vectors of the tetrahedron. With $\boldsymbol{k}_\beta^\dagger \boldsymbol{r}_\alpha = \delta_{\alpha\beta} - \frac{1}{4}$

(Eqn. 15.1 in ISSI SR-001) and $\sum_\beta \boldsymbol{k}_\beta = 0$ (Eqn 14.10 in ISSI SR-001 [*Chanteur*, 1998]) we finally arrive at the following explicit formula for the slowness vector:

$$\begin{aligned} \boldsymbol{m} &= \sum_\alpha \sum_\beta (t_\alpha - t_0)\, \boldsymbol{k}_\beta\, \boldsymbol{k}_\beta^\dagger\, \boldsymbol{r}_\alpha = \sum_\alpha (t_\alpha - t_0)\, \boldsymbol{k}_\alpha + \sum_\alpha (t_\alpha - t_0) \sum_\beta \boldsymbol{k}_\beta \\ &= \sum_\alpha (t_\alpha - t_0)\, \boldsymbol{k}_\alpha \end{aligned} \tag{4.4}$$

Note that the result is invariant with respect to a change of the origin of time because $\sum_\alpha \boldsymbol{k}_\alpha = 0$ and

$$\boldsymbol{m} = \sum_\alpha (t_\alpha - t_0)\, \boldsymbol{k}_\alpha = \sum_\alpha t_\alpha\, \boldsymbol{k}_\alpha - t_0 \sum_\alpha \boldsymbol{k}_\alpha = \sum_\alpha t_\alpha\, \boldsymbol{k}_\alpha \tag{4.5}$$

Using a similar approach, this result was derived also in Chapter 14 of ISSI SR-001 (Eqns. 14.46 and 14.47), where the case of a uniformly accelerated planar boundary was investigated as well.

The structure of this estimator follows a typical pattern: at each spacecraft α, the measured variable (in this case $t_\alpha - t_0$) is multiplied or combined with the respective reciprocal vector $\boldsymbol{k}_\alpha$, and then a summation of these expressions over all spacecraft is carried out to yield the physical parameter of interest. Linear estimators for spatial gradients can be written in the same way, see Section 4.4.

4.3 Properties of reciprocal vectors

The reciprocal vectors $\boldsymbol{k}_\alpha$ introduced in Section 4.2 are defined through

$$\boldsymbol{k}_\alpha = \frac{\boldsymbol{r}_{\beta\gamma} \times \boldsymbol{r}_{\beta\lambda}}{\boldsymbol{r}_{\beta\alpha} \cdot (\boldsymbol{r}_{\beta\gamma} \times \boldsymbol{r}_{\beta\lambda})} \tag{4.6}$$

where $\boldsymbol{r}_{\alpha\beta} = \boldsymbol{r}_\beta - \boldsymbol{r}_\alpha$ are relative position vectors, and $(\alpha, \beta, \gamma, \lambda)$ must be a cyclic permutation of $(1, 2, 3, 4)$. The set $\{\boldsymbol{k}_\alpha\}$ of reciprocal vectors is also called the reciprocal base of the tetrahedron.

The geometrical relationships of the $\boldsymbol{k}_\alpha$ within the tetrahedron are explained in the work of *Chanteur* [1998]. Most importantly, a reciprocal vector $\boldsymbol{k}_\alpha$ is perpendicular to the face of the tetrahedron that opposes the spacecraft at location $\boldsymbol{r}_\alpha$, and the length of $\boldsymbol{k}_\alpha$ is the inverse distance from spacecraft α to the opposing plane (see Figure 14.1 in ISSI SR-001). If the reciprocal vector $\boldsymbol{k}_\alpha$ is large, the distance between the spacecraft and the opposing plane is small, and this limits the resolving power of the Cluster satellite array in this particular direction. This is why reciprocal vectors are of key importance for error estimation [e.g., *Vogt and Paschmann*, 1998; *Chanteur*, 1998]. See also Sections 4.4.3 and 4.6.

The use of reciprocal vectors in boundary analysis was explained in Section 4.2. In Section 4.4 we will discuss in some detail how they enter spatial gradient estimators. They are useful also in a third area of multi-spacecraft data analysis, namely in wave parameter estimation. As pointed out by *Neubauer and Glassmeier* [1990], wave analysis techniques for multi-spacecraft missions suffer from spatial aliasing in a similar way as the traditional Fourier transform of time series does from temporal aliasing. *Chanteur* [1998] reformulated the spatial aliasing condition in terms of reciprocal vectors. If two harmonic plane

waves differ only by their wave vectors $\boldsymbol{k}$ and $\boldsymbol{k}'$, then they cannot be distinguished by measurement of the Cluster tetrahedron if

$$\boldsymbol{k} - \boldsymbol{k}' \;=\; 2\pi \sum_{\alpha} n_\alpha \boldsymbol{k}_\alpha \tag{4.7}$$

where n_α are signed integers. This condition is important for wave analysis techniques such as the k-filtering discussed in Chapter 5 of the present book.

4.4 Estimation of spatial gradients

Since spatial derivatives such as grad, div, and curl can be constructed from the gradient matrix of a vector field, one may collectively refer to *spatial gradient estimation* in this context. Before the reciprocal vector method is discussed in detail below, it is worth summarising some general aspects of the gradient estimation problem, and comparing related techniques. We conclude this section with a brief discussion of the geometrical errors associated with gradient estimation.

4.4.1 General aspects of gradient estimation

There exist several approaches to gradient estimation from Cluster data. Besides the reciprocal vector method, there is the *curlometer technique* [*Dunlop et al.*, 1988] described in Chapter 16 of ISSI SR-001 and in Chapter 2 of the present book, and the *least squares estimator* (given by *Harvey* [1998] in Chapter 12 of ISSI SR-001) that permit additional constraints, e.g., $\nabla \cdot \boldsymbol{B} = 0$, to be taken into account. It is important to note that without such constraints, the problem of linear gradient estimation from Cluster data is expected to yield a unique solution. This can be seen from an inspection of the general form of a vector-valued linear function

$$\boldsymbol{V}(\boldsymbol{r}) \;=\; \boldsymbol{V}_* \,+\, \mathsf{M}(\boldsymbol{r} - \boldsymbol{r}_*) \tag{4.8}$$

where $\boldsymbol{V}_*$ is a constant parameter representing the field value at a position $\boldsymbol{r}_*$, and M is a (3×3) matrix, namely, the gradient matrix $\nabla \boldsymbol{V}$. The parameters of this equation $\boldsymbol{V}_*$ and M provide 12 degrees of freedom. Measurements of four field vectors $\boldsymbol{V}_\alpha$ with three components yield 12 independent data. Hence, as long as the geometry is regular (i.e., the spacecraft configuration does not degenerate into a plane or line), and no additional constraints are considered, the linear interpolation problem has a unique solution, which also implies that all unconstrained linear gradient estimators are equivalent. Thus the spatial gradient estimation method based on reciprocal vectors yields the same result as, both, the curlometer technique and the unconstrained least squares estimator. For a refinement of the least squares approach, see *De Keyser et al.* [2007] and also Chapter 2.

The relationship of the least-squares estimator with the reciprocal vectors can be made explicit. The unconstrained least squares estimator requires constructing the inverse of the so-called *volumetric tensor* [*Harvey*, 1998]. For the general case of N spacecraft, and choosing (without loss of generality) the barycentre $(1/N)\sum_\alpha \boldsymbol{r}_\alpha$ of the spacecraft positions $\boldsymbol{r}_\alpha$ to be at the origin of the coordinate system, the volumetric tensor is given by $\mathsf{R} \;=\; (1/N)\sum_\alpha \boldsymbol{r}_\alpha \boldsymbol{r}_\alpha^\dagger$. If $N \;=\; 4$, the inverse tensor can be found from Eqn. 15.2

in ISSI SR-001, repeated here as Eqn. 4.3. Using this relationship, *Chanteur and Harvey* [1998] discussed the equivalence of the unconstrained least squares estimator and the reciprocal vectors method.

4.4.2 The reciprocal vector approach to gradient estimation

As explained by *Chanteur* [1998], linear interpolation of a scalar field $g = g(\boldsymbol{r})$ from measurements $g_\alpha = g(\boldsymbol{r}_\alpha)$ within the tetrahedron is accomplished by means of the *barycentric coordinates*

$$\mu_\alpha(\boldsymbol{r}) \;=\; 1 + \boldsymbol{k}_\alpha \cdot (\boldsymbol{r} - \boldsymbol{r}_\alpha) \tag{4.9}$$

as follows:

$$\tilde{g}(\boldsymbol{r}) \;=\; \sum_\alpha \mu_\alpha(\boldsymbol{r})\, g_\alpha \tag{4.10}$$

Vector functions $\boldsymbol{V}$ can be handled in a similar way. Here and in the following, the tilde symbol ˜ denotes linear estimation.

Since $\tilde{g}$ and $\tilde{\boldsymbol{V}}$ are linear functions, the calculation of spatial derivatives, such as the gradient of some scalar function or the divergence or curl of a vector function, can be done quite easily. The results are:

$$\nabla g \;\simeq\; \nabla\tilde{g} \;=\; \sum_{\alpha=0}^{3} \boldsymbol{k}_\alpha g_\alpha \tag{4.11}$$

$$\hat{\boldsymbol{e}} \cdot \nabla g \;\simeq\; \hat{\boldsymbol{e}} \cdot \nabla\tilde{g} \;=\; \sum_{\alpha=0}^{3} (\hat{\boldsymbol{e}} \cdot \boldsymbol{k}_\alpha) g_\alpha \tag{4.12}$$

$$\nabla \cdot \boldsymbol{V} \;\simeq\; \nabla \cdot \tilde{\boldsymbol{V}} \;=\; \sum_{\alpha=0}^{3} \boldsymbol{k}_\alpha \cdot \boldsymbol{V}_\alpha \tag{4.13}$$

$$\nabla \times \boldsymbol{V} \;\simeq\; \nabla \times \tilde{\boldsymbol{V}} \;=\; \sum_{\alpha=0}^{3} \boldsymbol{k}_\alpha \times \boldsymbol{V}_\alpha \tag{4.14}$$

As a general rule, the formula for the linear estimator of a spatial derivative is given by replacing the del operator ∇ with the sum $\sum_\alpha \boldsymbol{k}_\alpha$. The element (i, j) of the matrix $\nabla\boldsymbol{V}$ is given by:

$$\frac{\partial V_j}{\partial x_i} \;\equiv\; (\nabla\boldsymbol{V})_{ij} \;\simeq\; \sum_{\alpha=0}^{3} \left(\boldsymbol{k}_\alpha \boldsymbol{V}_\alpha^\dagger\right)_{ij} \;\equiv\; \sum_{\alpha=0}^{3} k_{\alpha i} V_{\alpha j} \tag{4.15}$$

or, in short,

$$\nabla\boldsymbol{V} \;\simeq\; \nabla\tilde{\boldsymbol{V}} \;=\; \sum_{\alpha=0}^{3} \boldsymbol{k}_\alpha \boldsymbol{V}_\alpha^\dagger \tag{4.16}$$

With regard to error estimation it is important to note that $\nabla \times \boldsymbol{V}$ and $\nabla \cdot \boldsymbol{V}$ are just linear combinations of various $(\nabla\boldsymbol{V})_{ij}$'s, and thus of terms like $k_{\alpha i} V_{\alpha j}$, with $i = j$ or $i \neq j$.

A number of papers on Cluster data have applied the reciprocal vector technique to compute spatial derivatives such as grad, div, or curl [e.g., *Rosenqvist et al.*, 2006; *Runov et al.*, 2003, 2005a, b; *Vallat et al.*, 2005; *Runov et al.*, 2006; *Vaivads et al.*, 2007].

4.4.3 Geometrical errors

The errors of spatial gradient estimators for the Cluster mission were analysed by a number of authors using theory and numerical simulations [e.g., *Chanteur*, 1998; *Chanteur and Harvey*, 1998; *Robert et al.*, 1998a; *Vogt and Paschmann*, 1998; *Chanteur*, 2000]. Here we do not summarise all this work but instead write down a simplified formula for spatial gradient estimation that quantifies the average (omnidirectional) uncertainty introduced by the geometry of the Cluster tetrahedron.

As demonstrated first by *Vogt and Paschmann* [1998], and confirmed also by *Chanteur* [2000], the inverse length scale

$$L_K^{-1} = \sqrt{\sum_{\alpha=0}^{3} |\boldsymbol{k}_\alpha|^2} \tag{4.17}$$

is of key importance in the analysis of geometrical errors of gradient estimation. *Vogt and Paschmann* [1998] demonstrated that first-order (isotropic) error estimation yields the following geometrical error of a spatial derivative $D\boldsymbol{V}$:

$$\delta|D\boldsymbol{V}| = \sqrt{\frac{f}{3}}\,\frac{\delta V}{L_K} \tag{4.18}$$

where δV denotes a typical error of the field measurement. The parameter f can be understood as the number of degrees of freedom of the differential operator D: use $f = 3$ if $D\boldsymbol{V} = \nabla\cdot\boldsymbol{V}$, $f = 2$ if $D\boldsymbol{V} = \nabla\times\boldsymbol{V}$, and $f = 1$ if $D\boldsymbol{V} = \hat{\boldsymbol{e}}\cdot\nabla\boldsymbol{V}$ (directional derivative or partial derivative).

4.5 Magnetic curvature

The gradient estimation based on reciprocal vectors can be applied directly to the magnetic field unit vector along the magnetic field line, $\hat{\boldsymbol{b}} = \boldsymbol{B}/B$, to yield the gradient matrix $\nabla\hat{\boldsymbol{b}}$, from which the curvature follows as $\boldsymbol{c} = \hat{\boldsymbol{b}}\cdot\nabla\hat{\boldsymbol{b}} = (\nabla\hat{\boldsymbol{b}})^{\dagger}\hat{\boldsymbol{b}}$. The curvature radius R_c is given by $R_c = 1/|\boldsymbol{c}|$. This identity was mentioned by *Runov et al.* [2005a] in their approach to magnetic curvature analysis, however, the precise implementation in the form of a curvature estimator was not given in their paper. A straightforward translation of this expression using reciprocal vectors yields

$$\boldsymbol{c} = \hat{\boldsymbol{b}}\cdot\nabla\hat{\boldsymbol{b}} \simeq \left(\sum_{\alpha=0}^{3}\hat{\boldsymbol{b}}_\alpha\boldsymbol{k}_\alpha^{\dagger}\right)\langle\hat{\boldsymbol{b}}\rangle = \sum_{\alpha=0}^{3}(\langle\hat{\boldsymbol{b}}\rangle\cdot\boldsymbol{k}_\alpha)\hat{\boldsymbol{b}}_\alpha \tag{4.19}$$

where $\langle\hat{\boldsymbol{b}}\rangle$ is defined as the unit vector colinear with $\langle\boldsymbol{B}\rangle = (1/4)\sum_\alpha \boldsymbol{B}_\alpha$.

Another starting point to curvature estimation is the gradient matrix $\nabla\boldsymbol{B}$ instead of $\nabla\hat{\boldsymbol{b}}$, from which one may directly compute the so-called magnetic tension $\boldsymbol{t} = \boldsymbol{B}\cdot\nabla\boldsymbol{B}$, which is an important term in the MHD equation of motion. The magnetic tension can be split into components perpendicular and parallel to the magnetic field as follows:

$$\boldsymbol{B}\cdot\nabla\boldsymbol{B} = \boldsymbol{B}\cdot\nabla(B\hat{\boldsymbol{b}}) = B^2\hat{\boldsymbol{b}}\cdot\nabla\hat{\boldsymbol{b}} + \hat{\boldsymbol{b}}(\boldsymbol{B}\cdot\nabla B) = \boldsymbol{t}_\perp + \boldsymbol{t}_\parallel \tag{4.20}$$

The first term is proportional to the magnetic field curvature $\boldsymbol{c} = \hat{\boldsymbol{b}} \cdot \nabla \hat{\boldsymbol{b}}$, already encountered above (Eqn. 4.19). The second term can be rewritten to yield

$$\boldsymbol{t}_{\parallel} \;=\; B^{-2} \boldsymbol{B} \left[\boldsymbol{B} \cdot (\boldsymbol{B} \cdot \nabla \boldsymbol{B}) \right] \tag{4.21}$$

Combining these expressions, the curvature can be expressed in terms of the gradient matrix as follows:

$$\boldsymbol{c} \;=\; B^{-2} \boldsymbol{t}_{\perp} \;=\; B^{-2} \left[\boldsymbol{t} - \boldsymbol{t}_{\parallel} \right] \;=\; B^{-2} \boldsymbol{B} \cdot \nabla \boldsymbol{B} - B^{-4} \boldsymbol{B} \left[\boldsymbol{B} \cdot (\boldsymbol{B} \cdot \nabla \boldsymbol{B}) \right] \tag{4.22}$$

or, using cartesian components $i, j, \ell \in \{x, y, z\}$:

$$c_j \;=\; B^{-2} \sum_i B_i \nabla_i B_j - B^{-4} B_j \sum_{i,\ell} B_i B_\ell \nabla_\ell B_i \tag{4.23}$$

Shen et al. [2003] based their curvature estimation on this identity (see Chapter 3).

An estimator of the curvature vector $\boldsymbol{c}$ is easily derived by defining the mean field encompassed by Cluster, and the associated unit vector through $\langle \boldsymbol{B} \rangle = (1/4) \sum_\alpha \boldsymbol{B}_\alpha = B \langle \hat{\boldsymbol{b}} \rangle$. This yields

$$B \boldsymbol{c} \simeq \left(\sum_{\alpha=0}^{3} \boldsymbol{B}_\alpha \, \boldsymbol{k}_\alpha^\dagger \right) \langle \hat{\boldsymbol{b}} \rangle - \langle \hat{\boldsymbol{b}} \rangle^\dagger \left(\sum_{\alpha=0}^{3} \boldsymbol{B}_\alpha \, \boldsymbol{k}_\alpha^\dagger \right) \langle \hat{\boldsymbol{b}} \rangle \langle \hat{\boldsymbol{b}} \rangle \tag{4.24}$$

which can be rewritten as

$$\boldsymbol{c} \simeq \frac{1}{B^4} \sum_{\alpha=0}^{3} \langle \boldsymbol{B} \rangle^\dagger \left(\langle \boldsymbol{B} \rangle \boldsymbol{B}_\alpha - \boldsymbol{B}_\alpha \langle \boldsymbol{B} \rangle \right) \langle \boldsymbol{B} \rangle^\dagger \boldsymbol{k}_\alpha \tag{4.25}$$

We conclude this section with some words of caution. Obviously, the estimator 4.25 yields a curvature vector that vanishes when the four measured magnetic vectors $\boldsymbol{B}_\alpha$ are identical. This is not immediately clear in configurations where the field lines are still straight (zero curvature) but the magnitude is varying in space, e.g., at a planar current sheet if the normal component of the ambient magnetic field is zero. In this case, and in the absence of measurement errors, the two contributions to the estimator 4.25 have to be equal in magnitude and opposite in sign. If measurement errors come into play, two almost equally large terms are subtracted, and cancellation errors may occur.

The estimator 4.19 may avoid this particular problem, however, in this case consistency has to be checked because linear interpolation of the data $\hat{\boldsymbol{b}}_\alpha$ does not in general give a field $\tilde{\boldsymbol{b}} = \tilde{\boldsymbol{b}}(\boldsymbol{r})$ that satisfies the normalisation condition $|\tilde{\boldsymbol{b}}| = 1$. A more detailed analysis shows that 4.19 is indeed a consistent curvature estimator but it is not clear, *a priori*, how neglecting the normalisation constraint affects the quality of the estimation. A proper analysis of the truncation errors of the curvature estimators is beyond the scope of this paper. For the case of a thick and planar current sheet, such an analysis suggests that the number of truncation error terms is reduced if the constraint $|\hat{\boldsymbol{b}}| = 1$ is taken into account properly.

4.6 Errors for boundary analysis and magnetic curvature

The results of boundary motion and magnetic curvature analyses (Eqns. 4.4 and 4.19 respectively) can be written formally in a unique way that allows a full error analysis, taking into account both physical and geometrical uncertainties. These results have been applied to crossings of the terrestrial bow shock by *Cornilleau-Wehrlin et al.* [2003]. This section gives the details of this unpublished derivation. In the following, $\boldsymbol{A}$ is either the slowness vector $\boldsymbol{m}$ (Eqn. 4.4) or the mean curvature vector $\boldsymbol{c}$ (Eqn. 4.25) of the magnetic field lines encompassed by the cluster of spacecraft.

$$\boldsymbol{A} = \sum_{\alpha=0}^{3} A_\alpha \boldsymbol{k}_\alpha \tag{4.26}$$

$$\lambda = (\boldsymbol{A}\cdot\boldsymbol{A})^{-1/2} \tag{4.27}$$

$$\hat{\boldsymbol{n}} = \lambda\,\boldsymbol{A} \tag{4.28}$$

where the physical coefficient A_α is either the scalar crossing time t_α for the boundary analysis, or the tensor product $\langle\boldsymbol{B}\rangle^\dagger\,(\langle\boldsymbol{B}\rangle\boldsymbol{B}_\alpha - \boldsymbol{B}_\alpha\langle\boldsymbol{B}\rangle)\,\langle\boldsymbol{B}\rangle^\dagger$ in the case of the magnetic curvature.

The investigation of the statistical properties of A, λ, and $\hat{\boldsymbol{n}}$ rely upon the following considerations. The true position of spacecraft α differs from its nominal position $\boldsymbol{r}_\alpha$ by a small and random vector $\delta\boldsymbol{r}_\alpha$, and the true physical coefficient differs from the nominal one by a small and random deviation δA_α. The deviations of measured quantities are assumed to be sufficiently small to represent the uncertainties of the computed quantities in terms of their linear variations. Differentiating Eqns. 4.26–4.28 and noticing that $(\boldsymbol{A}\cdot\delta\boldsymbol{A})\,\boldsymbol{A} = \boldsymbol{A}\,\boldsymbol{A}^\dagger\,\delta\boldsymbol{A}$, the variations $\delta\boldsymbol{A}$, $\delta\hat{\boldsymbol{n}}$ and $\delta\lambda$ are written:

$$\delta\boldsymbol{A} = \sum_{\alpha} (\delta A_\alpha \boldsymbol{k}_\alpha + A_\alpha \delta\boldsymbol{k}_\alpha) \tag{4.29}$$

$$\delta\hat{\boldsymbol{n}} = \lambda\left(\mathsf{I} - \hat{\boldsymbol{n}}\,\hat{\boldsymbol{n}}^\dagger\right)\delta\boldsymbol{A} \tag{4.30}$$

$$\delta\lambda = -\lambda^3\,(\boldsymbol{A}\cdot\delta\boldsymbol{A}) \tag{4.31}$$

where $\hat{\boldsymbol{n}}^\dagger$ denotes the transpose of $\hat{\boldsymbol{n}}$ and I is the unit tensor. The uncertainty of a physical quantity X is measured by the covariance $\langle(\delta X - \langle\delta X\rangle)(\delta X - \langle\delta X\rangle)^\dagger\rangle$ of its variation δX.

A few supplementary assumptions are made when computing uncertainties. First, it is assumed that both physical coefficients and spacecraft positions are unbiased, $\langle\delta A_\alpha\rangle = 0$ and $\langle\delta\boldsymbol{r}_\alpha\rangle = 0$, which ensures unbiased estimations of the reciprocal vectors and of λ, $\boldsymbol{A}$ and $\hat{\boldsymbol{n}}$. Second, the covariances of physical coefficients and positions are assumed equal to zero, $\langle\delta\boldsymbol{r}_\alpha\,\delta A\dagger_\beta\rangle = 0$. It then follows from Eqn. 14.24 in ISSI SR-001 that $\langle\delta\boldsymbol{k}_\alpha\delta A^\dagger_\beta\rangle = 0$. Third, it is assumed that covariances of spacecraft positions can be written as Eqn. 14.27 in ISSI SR-001. With these hypotheses, the covariances of $\delta\boldsymbol{A}$, $\delta\hat{\boldsymbol{n}}$ and the uncertainty $\Delta\lambda$ can be written:

$$\langle \delta \boldsymbol{A}\, \delta \boldsymbol{A}^{\dagger} \rangle = \sum_{\alpha,\beta} \langle \delta A_{\alpha}\, \boldsymbol{k}_{\alpha}\, \boldsymbol{k}_{\beta}^{\dagger}\, \delta A_{\beta}^{\dagger} \rangle + \sum_{\alpha,\beta} A_{\alpha} \langle \delta \boldsymbol{k}_{\alpha}\, \delta \boldsymbol{k}_{\beta}^{\dagger} \rangle A_{\beta}^{\dagger} \tag{4.32}$$

$$\langle \delta \hat{\boldsymbol{n}}\, \delta \hat{\boldsymbol{n}}^{\dagger} \rangle = \lambda^2 \left(\mathsf{I} - \hat{\boldsymbol{n}}\, \hat{\boldsymbol{n}}^{\dagger} \right) \langle \delta \boldsymbol{A}\, \delta \boldsymbol{A}^{\dagger} \rangle \left(\mathsf{I} - \hat{\boldsymbol{n}}\, \hat{\boldsymbol{n}}^{\dagger} \right) \tag{4.33}$$

$$(\Delta\lambda)^2 = \lambda^4\, \hat{\boldsymbol{n}}^{\dagger}\, \langle \delta \boldsymbol{A}\, \delta \boldsymbol{A}^{\dagger} \rangle\, \hat{\boldsymbol{n}} \tag{4.34}$$

where the covariance $\langle \delta \boldsymbol{k}_{\alpha}\, \delta \boldsymbol{k}_{\beta}^{\dagger} \rangle$ is given by :

$$\langle \delta \boldsymbol{k}_{\alpha}\, \delta \boldsymbol{k}_{\beta}^{\dagger} \rangle = \sum_{\gamma} \boldsymbol{k}_{\alpha}^{\dagger}\, \langle \delta \boldsymbol{r}\, \delta \boldsymbol{r}^{\dagger} \rangle_{\gamma}\, \boldsymbol{k}_{\beta}\, \boldsymbol{k}_{\gamma}\, \boldsymbol{k}_{\gamma}^{\dagger} \tag{4.35}$$

The angular uncertainty of $\hat{\boldsymbol{n}}$ in the plane given by $\hat{\boldsymbol{n}}$ and a given unit vector $\hat{\boldsymbol{e}}$ orthogonal to $\hat{\boldsymbol{n}}$ is approximately equal to the following expression, as long as it is small compared to unity:

$$(\Delta\theta)^2 = \hat{\boldsymbol{e}}^{\dagger} \langle \delta \hat{\boldsymbol{n}}\, \delta \hat{\boldsymbol{n}}^{\dagger} \rangle\, \boldsymbol{e} \tag{4.36}$$

$$= \lambda^2\, \hat{\boldsymbol{e}}^{\dagger} \langle \delta \boldsymbol{A}\, \delta \boldsymbol{A}^{\dagger} \rangle\, \hat{\boldsymbol{e}} \tag{4.37}$$

From now on, the discussion is limited to the case of scalar physical coefficients A_{α}, for example $A_{\alpha} = t_{\alpha}$, the crossing time. In that case, Eqn. 4.32 simplifies to:

$$\langle \delta \boldsymbol{A}\, \delta \boldsymbol{A}^{\dagger} \rangle = \sum_{\alpha,\beta} \langle \delta t_{\alpha}\, \delta t_{\beta} \rangle \boldsymbol{k}_{\alpha}\, \boldsymbol{k}_{\beta}^{\dagger} + \sum_{\alpha,\beta} t_{\alpha} t_{\beta} \langle \delta \boldsymbol{k}_{\alpha}\, \delta \boldsymbol{k}_{\beta}^{\dagger} \rangle \tag{4.38}$$

With the help of Eqns. 4.37, 4.38, and 4.35, the angular uncertainty is explicitly written as:

$$C_1 = \sum_{\alpha,\beta} \langle \delta t_{\alpha} \delta t_{\beta} \rangle (\hat{\boldsymbol{e}} \cdot \boldsymbol{k}_{\alpha})(\hat{\boldsymbol{e}} \cdot \boldsymbol{k}_{\beta}) \tag{4.39}$$

$$C_2 = \sum_{\gamma} \boldsymbol{A}^{\dagger} \langle \delta \boldsymbol{r}\, \delta \boldsymbol{r}^{\dagger} \rangle_{\gamma}\, \boldsymbol{A}\, (\hat{\boldsymbol{e}} \cdot \boldsymbol{k}_{\gamma})^2 \tag{4.40}$$

$$(\Delta\theta)^2 = \lambda^2 (C_1 + C_2) \tag{4.41}$$

Figure 4.1 shows the cone of uncertainty of the determined direction. In the general case, this cone is not axi-symmetric (i.e., has elliptical cross-section), because the coefficients C_1 and C_2, defined by Eqns. 4.39 and 4.40, depend upon the unit vector $\hat{\boldsymbol{e}}$. Crossing time measurements onboard different spacecraft with uncertainties Δt_{α} are statistically independent, which means that $\langle \delta t_{\alpha}\, \delta t_{\beta} \rangle = \delta_{\alpha,\beta}\, (\Delta t_{\alpha})^2$, and the covariances of $\delta \boldsymbol{A}$ become:

$$C_{\gamma} = (\Delta t_{\gamma})^2 + \boldsymbol{A}^{\dagger} \langle \delta \boldsymbol{r}\, \delta \boldsymbol{r}^{\dagger} \rangle_{\gamma}\, \boldsymbol{A} \tag{4.42}$$

$$\langle \delta \boldsymbol{A}\, \delta \boldsymbol{A}^{\dagger} \rangle = \sum_{\gamma} C_{\gamma}\, \boldsymbol{k}_{\gamma}\, \boldsymbol{k}_{\gamma}^{\dagger} \tag{4.43}$$

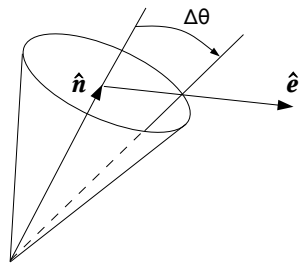

Figure 4.1: The cone of uncertainty of $\hat{\boldsymbol{n}}$ is defined through the angular uncertainty of $\hat{\boldsymbol{n}}$ along a given direction, specified by a unit vector $\hat{\boldsymbol{e}}$ orthogonal to $\hat{\boldsymbol{n}}$.

The error analysis for the bow shock crossings presented in *Cornilleau-Wehrlin et al.* [2003] made use of Eqns. 4.37, 4.42, and 4.43.

If the uncertainties Δt_γ and covariances $\langle \delta \boldsymbol{r}_\alpha \, \delta \boldsymbol{r}_\beta^\dagger \rangle_\gamma$ are the same for all four spacecraft, then C does not depend on γ and the covariances of $\delta \boldsymbol{A}$, $\delta \hat{\boldsymbol{n}}$ and the uncertainty $\delta\lambda$ can be further simplified and written:

$$C = (\Delta t)^2 + \boldsymbol{A}^\dagger \langle \delta \boldsymbol{r} \, \delta \boldsymbol{r}^\dagger \rangle \, \boldsymbol{A} \tag{4.44}$$

$$\langle \delta \boldsymbol{A} \, \delta \boldsymbol{A}^\dagger \rangle = C \, \mathsf{K} \tag{4.45}$$

$$\langle \delta \hat{\boldsymbol{n}} \, \delta \hat{\boldsymbol{n}}^\dagger \rangle = C \, \lambda^2 \left(\mathsf{I} - \hat{\boldsymbol{n}} \, \hat{\boldsymbol{n}}^\dagger \right) \mathsf{K} \left(\mathsf{I} - \hat{\boldsymbol{n}} \, \hat{\boldsymbol{n}}^\dagger \right) \tag{4.46}$$

$$(\Delta\lambda)^2 = C \, \lambda^4 \, \hat{\boldsymbol{n}}^\dagger \mathsf{K} \hat{\boldsymbol{n}} \tag{4.47}$$

where K is the reciprocal tensor. For a regular tetrahedron with an inter-spacecraft distance d, the reciprocal tensor is proportional to the unit tensor, $\mathsf{K} = (2/d^2)\mathsf{I}$, so that the covariances and uncertainties given by Eqns. 4.37, 4.46, and 4.47 reduce to:

$$\Delta\theta = \frac{\lambda}{d} \sqrt{2C} \tag{4.48}$$

$$\frac{\Delta\lambda}{\lambda} = \Delta\theta \tag{4.49}$$

$$\langle \delta \hat{\boldsymbol{n}} \, \delta \hat{\boldsymbol{n}}^\dagger \rangle = (\Delta\theta)^2 \left(\mathsf{I} - \hat{\boldsymbol{n}} \, \hat{\boldsymbol{n}}^\dagger \right) \tag{4.50}$$

In that case, the cone of uncertainty is axi-symmetric around $\hat{\boldsymbol{n}}$. Another simplification occurs when $\langle \delta \boldsymbol{r} \, \delta \boldsymbol{r}^\dagger \rangle = (\Delta r)^2 \, \mathsf{I}$, where Δr is the uncertainty of the spacecraft positions. In that case, the coefficient C, defined by Eqn. 4.44, simplifies to:

$$C = (\Delta t)^2 + \frac{(\Delta r)^2}{\lambda^2} \tag{4.51}$$

Note that the results from this section apply equally to the gradient of a scalar field. Regarding the effect of the spacecraft configuration, it should be noted that a flat or elongated tetrahedron makes the errors very anisotropic.

4.7 Generalised reciprocal vectors for $N \neq 4$

The least-squares approach presented in Section 4.2 suggests a straightforward generalisation of the reciprocal vector concept to the general case where the number of spacecraft N is larger than four. As before, we choose the origin of our coordinate system to be the barycentre of the spacecraft array, which implies

$$\sum_\alpha \boldsymbol{r}_\alpha \;=\; 0 \tag{4.52}$$

As pointed out in ISSI SR-001 by *Harvey* [1998], boundary parameter estimation using the crossing time approach as well as spatial gradient estimation involves minimisation of a cost function of the type

$$S \;=\; \sum_\alpha [\boldsymbol{p}\cdot\boldsymbol{r}_\alpha - d_\alpha]^2 \tag{4.53}$$

Here $\boldsymbol{p}$ denotes the parameter vector to be estimated, and the data are given by $d_\alpha, \alpha = 1,\ldots,N$. In boundary analysis using crossing times t_α, we have $\boldsymbol{p} = \boldsymbol{m}$ (slowness vector) and $d_\alpha = (t_\alpha - t_0)$. In the estimation of the spatial gradient of a scalar observable g, $\boldsymbol{p} = \nabla g$ and $d_\alpha = g_\alpha$. The algebra presented by *Harvey* [1998] and summarised in Section 4.2 translates directly to the general case which means that the solution of the least-squares problem is given by

$$\boldsymbol{p} \;=\; \mathsf{R}^{-1}\sum_\alpha \boldsymbol{r}_\alpha\, d_\alpha \tag{4.54}$$

where the position tensor R is defined through

$$\mathsf{R} \;=\; \sum_\beta \boldsymbol{r}_\beta\, \boldsymbol{r}_\beta^{\dagger} \tag{4.55}$$

Note that the position tensor differs by a factor of $1/N$ from the volumetric tensor used by *Harvey* [1998].

We now introduce N vectors through the relation

$$\boldsymbol{q}_\alpha \;=\; \mathsf{R}^{-1}\boldsymbol{r}_\alpha\;,\;\; \alpha = 1,\ldots,N \tag{4.56}$$

By use of the vectors $\boldsymbol{q}_\alpha$, one can write the solution of the least-squares problem in the following form:

$$\boldsymbol{p} \;=\; \sum_\alpha \boldsymbol{q}_\alpha\, d_\alpha \tag{4.57}$$

In particular, a spatial gradient estimator can be expressed as $\sum_\alpha \boldsymbol{q}_\alpha\, g_\alpha$. The other formulas in Section 4.4 also translate to the case $N > 4$, if we replace the $\boldsymbol{k}_\alpha$'s with the $\boldsymbol{q}_\alpha$'s. The slowness vector $\boldsymbol{m}$ of Section 4.2 is given by

$$\boldsymbol{m} \;=\; \sum_\alpha (t_\alpha - t_0)\,\boldsymbol{q}_\alpha \;=\; \sum_\alpha t_\alpha\,\boldsymbol{q}_\alpha - t_0\sum_\alpha \boldsymbol{q}_\alpha \;=\; \sum_\alpha t_\alpha\,\boldsymbol{q}_\alpha \tag{4.58}$$

because

$$\sum_\alpha \boldsymbol{q}_\alpha \;=\; \sum_\alpha \mathsf{R}^{-1}\boldsymbol{r}_\alpha \;=\; \mathsf{R}^{-1}\sum_\alpha \boldsymbol{r}_\alpha \;=\; 0 \tag{4.59}$$

In this sense, the vectors $\boldsymbol{q}_\alpha, \alpha = 1, \ldots, N$, can be interpreted as generalised reciprocal vectors for the case $N \geq 4$. We further note that the definition of the vectors $\boldsymbol{q}_\alpha$ implies that

$$\sum_\alpha \boldsymbol{q}_\alpha \boldsymbol{r}_\alpha^\dagger = \mathsf{I} = \sum_\alpha \boldsymbol{r}_\alpha \boldsymbol{q}_\alpha^\dagger \tag{4.60}$$

$$\sum_\alpha \boldsymbol{q}_\alpha \cdot \boldsymbol{r}_\alpha = \mathrm{Tr}\{\mathsf{I}\} = 3 \tag{4.61}$$

$$\sum_\alpha \boldsymbol{q}_\alpha \times \boldsymbol{r}_\alpha = 0 \tag{4.62}$$

and that

$$\mathsf{RQ} = \mathsf{I} = \mathsf{QR} \quad \Rightarrow \quad \mathsf{R}^{-1} = \mathsf{Q} \tag{4.63}$$

Here I denotes the identity tensor, and the generalised reciprocal tensor Q is given by

$$\mathsf{Q} = \sum_\alpha \boldsymbol{q}_\alpha \boldsymbol{q}_\alpha^\dagger \tag{4.64}$$

The corresponding relations for the reciprocal vectors $\boldsymbol{k}_\alpha$ (special case $N = 4$) can be found in ISSI SR-001, see Section 14.2.1 in the Chapter by *Chanteur* [1998], and Eqn. 15.2 in the Chapter by *Chanteur and Harvey* [1998].

In the definition of the generalised reciprocal vectors $\boldsymbol{q}_\alpha$ given above, the position tensor R has to be inverted. The inverse R^{-1} exists if the spacecraft configuration does not degenerate into a planar one. More specifically, if R is singular, at least one of its eigenvalues is zero, and the plane that contains all spacecraft is perpendicular to any eigenvector $\boldsymbol{w} \neq \boldsymbol{0}$ to the zero eigenvalue. To formally demonstrate this statement, we note that $\mathsf{R}\boldsymbol{w} = \boldsymbol{0}$ and look at the associated quadratic form

$$0 = \boldsymbol{w}^\dagger \mathsf{R} \boldsymbol{w} = \boldsymbol{w}^\dagger \left(\sum_\alpha \boldsymbol{r}_\alpha \boldsymbol{r}_\alpha^\dagger \right) \boldsymbol{w} = \sum_\alpha \boldsymbol{w}^\dagger \boldsymbol{r}_\alpha \boldsymbol{r}_\alpha^\dagger \boldsymbol{w} = \sum_\alpha |\boldsymbol{w}^\dagger \boldsymbol{r}_\alpha|^2 \tag{4.65}$$

which implies that

$$\boldsymbol{w}^\dagger \boldsymbol{r}_\alpha \equiv \boldsymbol{w} \cdot \boldsymbol{r}_\alpha = 0 \tag{4.66}$$

for all $\alpha = 1, \ldots, N$. Equivalently,

$$\boldsymbol{w} \perp \boldsymbol{r}_\alpha \,, \; \alpha = 1, \ldots, N \tag{4.67}$$

Hence all position vectors $\boldsymbol{r}_\alpha$ are perpendicular to the eigenvector $\boldsymbol{w}$, and this effectively constrains all spacecraft to lie in one plane.

In those cases where the geometrical configuration is three-dimensional but deviates not much from a planar one, a straightforward numerical inversion may still be problematic (ill-conditioned). Note that the condition number of the symmetric and positive semi-definite tensor R can be written in terms of its eigenvalues. These in turn are related to the planarity and the elongation of the spacecraft polyhedron as defined in Section 13.3.3 of ISSI SR-001 [*Robert et al.*, 1998b]. In the ill-conditioned case, a regularisation approach, using Singular Value Decomposition, may improve the solution. This problem, however, is beyond the scope of this chapter and requires further study. It is interesting to note that

in the field of computer graphics there is considerable research activity on closely related questions [see e.g. *Ju et al.*, 2007].

In the case $N \leq 3$, i.e., if the number of spacecraft is three or less, the position tensor is always singular, and reciprocal vectors cannot be constructed as outlined above. Planar reciprocal vectors can still be defined in the case $N = 3$; however, in order to arrive at a fully three-dimensional reconstruction, additional information (assumptions or physical constraints) have to be taken into account. This case is currently under investigation by one of the authors (J.V.).

Software implementation

Implementations of the reciprocal vector approach to spatial gradient estimation exist, e.g., in IDL (the package cdat by Joachim Vogt, available from the author), and also in the comprehensive data analysis software QSAS, available at http://www.sp.ph.ic.ac.uk/csc-web/QSAS/.

Bibliography

Chanteur, G., 1998, Spatial Interpolation for Four Spacecraft: Theory, in *Analysis Methods for Multi-Spacecraft Data*, edited by G. Paschmann and P. W. Daly, no. SR-001 in ISSI Scientific Reports, chap. 14, pp. 349–369, ESA Publ. Div., Noordwijk, Netherlands.

Chanteur, G., 2000, Accuracy of field gradient estimations by Cluster: Explanation of its dependency upon elongation and planarity of the tetrahedron, in *Cluster-II Workshop: Multiscale/Multipoint Plasma Measurements*, edited by R. A. Harris, ESA SP-449, pp. 265–268, ESA Publ. Div., Noordwijk, Netherlands.

Chanteur, G. and Harvey, C. C., 1998, Spatial Interpolation for Four Spacecraft: Application to Magnetic Gradients, in *Analysis Methods for Multi-Spacecraft Data*, edited by G. Paschmann and P. W. Daly, no. SR-001 in ISSI Scientific Reports, chap. 15, pp. 371–393, ESA Publ. Div., Noordwijk, Netherlands.

Cornilleau-Wehrlin, N., Chanteur, G., Perraut, S., Rezeau, L., Robert, P., Roux, A., de Villedary, C., Canu, P., Maksimovic, M., de Conchy, Y., Hubert, D., Lacombe, C., Lefeuvre, F., Parrot, M., Pinçon, J. L., Décréau, P. M. E., Harvey, C. C., Louarn, P., Santolik, O., Alleyne, H. S. C., Roth, M., Chust, T., LeContel, O., and STAFF team, 2003, First results obtained by the Cluster STAFF experiment, *Ann. Geophys.*, **21**, 437–456, http://www.ann-geophys.net/21/437/2003/.

De Keyser, J., Darrouzet, E., Dunlop, M. W., and Décréau, P. M. E., 2007, Least-squares gradient calculation from multi-point observations of scalar and vector fields: methodology and applications with Cluster in the plasmasphere, *Ann. Geophys.*, **25**, 971–987, http://www.ann-geophys.net/25/971/2007/.

Dunlop, M. W., Southwood, D. J., Glassmeier, K.-H., and Neubauer, F. M., 1988, Analysis of multipoint magnetometer data, *Adv. Space Res.*, **8**, 273–1177.

Harvey, C. C., 1998, Spatial Gradients and the Volumetric Tensor, in *Analysis Methods for Multi-Spacecraft Data*, edited by G. Paschmann and P. W. Daly, no. SR-001 in ISSI Scientific Reports, chap. 12, pp. 307–322, ESA Publ. Div., Noordwijk, Netherlands.

Ju, T., Liepa, P., and Warren, J., 2007, A general geometric construction of coordinates in a convex simplicial polytope, *Comput. aided geom. des.*, **24**, 161–178.

Neubauer, F. M. and Glassmeier, K.-H., 1990, Use of an array of satellites as a wave telescope, *J. Geophys. Res.*, **95**, 19 115–19 122.

Robert, P., Dunlop, M. D., Roux, A., and Chanteur, G., 1998a, Accuracy of Current Density Estimation, in *Analysis Methods for Multi-Spacecraft Data*, edited by G. Paschmann and P. W. Daly, no. SR-001 in ISSI Scientific Reports, chap. 16, pp. 395–418, ESA Publ. Div., Noordwijk, Netherlands.

Robert, P., Roux, A., Harvey, C. C., Dunlop, M. W., Daly, P. W., and Glassmeier, K.-H., 1998b, Tetrahedron Geometric Factors, in *Analysis Methods for Multi-Spacecraft Data*, edited by G. Paschmann and P. W. Daly, no. SR-001 in ISSI Scientific Reports, chap. 13, pp. 323–348, ESA Publ. Div., Noordwijk, Netherlands.

Rosenqvist, L., Buchert, S., Opgenoorth, H., Vaivads, A., and Lu, G., 2006, Magnetospheric energy budget during huge geomagnetic activity using Cluster and ground-based data, *J. Geophys. Res.*, **111**, A10211, doi: 10.1029/2006JA011608.

Runov, A., Nakamura, R., Baumjohann, W., Treumann, R. A., Zhang, T. L., Volwerk, M., Vörös, Z., Balogh, A., Glaßmeier, K.-H., Klecker, B., Rème, H., and Kistler, L., 2003, Current sheet structure near magnetic X-line observed by Cluster, *Geophys. Res. Lett.*, **30**, 33–1.

Runov, A., Sergeev, V. A., Baumjohann, W., Nakamura, R., Apatenkov, S., Asano, Y., Volwerk, M., Vörös, Z., Zhang, T. L., Petrukovich, A., Balogh, A., Sauvaud, J.-A., Klecker, B., and Rème, H., 2005a, Electric current and magnetic field geometry in flapping magnetotail current sheets, *Ann. Geophys.*, **23**, 1391–1403, http://www.ann-geophys.net/23/1391/2005/.

Runov, A., Sergeev, V. A., Nakamura, R., Baumjohann, W., Zhang, T. L., Asano, Y., Volwerk, M., Vörös, Z., Balogh, A., and Rème, H., 2005b, Reconstruction of the magnetotail current sheet structure using multi-point Cluster measurements, *Planet. Space Sci.*, **53**, 237–243, doi:10.1016/j.pss.2004.09.049.

Runov, A., Sergeev, V. A., Nakamura, R., Baumjohann, W., Apatenkov, S., Asano, Y., Takada, T., Volwerk, M., Vörös, Z., Zhang, T. L., Sauvaud, J.-A., Rème, H., and Balogh, A., 2006, Local structure of the magnetotail current sheet: 2001 Cluster observations, *Ann. Geophys.*, **24**, 247–262, http://www.ann-geophys.net/24/247/2006/.

Shen, C., Li, X., Dunlop, M., Liu, Z. X., Balogh, A., Baker, D. N., Hapgood, M., and Wang, X., 2003, Analyses on the geometrical structure of magnetic field in the current sheet based on cluster measurements, *J. Geophys. Res.*, **108**, 1168, doi:10.1029/2002JA009612.

Vaivads, A., Santolík, O., Stenberg, G., André, M., Owen, C. J., Canu, P., and Dunlop, M., 2007, Source of whistler emissions at the dayside magnetopause, *Geophys. Res. Lett.*, **34**, L09106, doi:10.1029/2006GL029195.

Vallat, C., Dandouras, I., Dunlop, M., Balogh, A., Lucek, E., Parks, G. K., Wilber, M., Roelof, E. C., Chanteur, G., and Rème, H., 2005, First current density measurements in the ring current region using simultaneous multi-spacecraft CLUSTER-FGM data, *Ann. Geophys.*, **23**, 1849–1865, http://www.ann-geophys.net/23/1849/2005/.

Vogt, J. and Paschmann, G., 1998, Accuracy of Plasma Moment Derivatives, in *Analysis Methods for Multi-Spacecraft Data*, edited by G. Paschmann and P. W. Daly, no. SR-001 in ISSI Scientific Reports, chap. 17, pp. 419–447, ESA Publ. Div., Noordwijk, Netherlands.

— 5 —

Multi-Spacecraft Methods of Wave Field Characterisation

JEAN-LOUIS PINÇON
LPCE/CNRS
Orléans, France

KARL-HEINZ GLASSMEIER
Institut für Geophysik und extraterrestrische Physik
Braunschweig, Germany

5.1 Introduction

Space plasmas are collisionless and thus waves play a major role in the collective interaction between particles. Also, space plasmas are subject to a variety of instabilities, generating a plethora of different plasma wave modes. Thus, for many physical processes the role of waves and turbulence is likely to be predominant. The simultaneous four-point measurements available from the Cluster mission enable spatio-temporal effects in data sets to be resolved, which is mandatory for the unambiguous identification of waves and plasma turbulence. The two main methodologies that have been used for wave field characterisation in the frame of Cluster are the k-filtering/wave-telescope technique and the phase differencing technique. Important new results obtained through the applications of both techniques to Cluster data have been presented in numerous studies. The purpose of this chapter is not to discuss the scientific results obtained, but to serve as a guide for the interested reader as to what has been learned regarding wave identification methods using multi-spacecraft data and where to find it.

The following is a brief outline of the chapter. In Sections 5.2 and 5.3, respectively, the basic principles of k-filtering/wave-telescope and phase differencing techniques are presented. Section 5.4 describes the main problems and limitations encountered by applying the methods to real data. In Section 5.5 the most recent developments of the k-filtering and phase differencing techniques are presented and the future of wave field characterisation through multi-spacecraft methods is briefly discussed.

5.2 k-filtering — wave-telescope technique

The k-filtering technique, also called the wave-telescope technique when applied to magnetic field fluctuations, is described in Chapter 3 of ISSI SR-001 [*Pinçon and Motschmann*, 1998]. The technique is an adaptation of methods used in geophysics for analysing seismic waves from seismographs distributed over the globe [*Capon*, 1969]. The three-dimensional generalisation to space plasmas was introduced by *Pinçon and Lefeuvre* [1991]; *Pinçon and Lefeuvre* [1992]. It is a method to characterise stationary fluctuations in space plasmas in terms of the field energy distribution in the frequency and wave vector space.

It is based on simultaneous multi-point measurements of the electromagnetic wave field components, where a filter bank is used to enhance the spatial resolution.

The k-filtering/wave-telescope technique was applied for the first time to fluxgate magnetometer data from the Cluster FGM instrument by *Glassmeier et al.* [2001], to the search-coil magnetometer data from the Cluster STAFF instrument by *Sahraoui et al.* [2003], and to combined Cluster electric field and magnetometer data from the EFW and STAFF instruments by *Tjulin et al.* [2005]. The basic principles of the technique are as follows: Let $\boldsymbol{A}(t, \boldsymbol{r}_\alpha)$ be the measured wave field at positions $\boldsymbol{r}_\alpha$ ($\alpha = 1, 2, \ldots$). Assuming that the measured field is described as a superposition of plane waves, the general expression is given by:

$$\boldsymbol{A}(t, \boldsymbol{r}_\alpha) = \sum_\omega \sum_k \boldsymbol{A}_{\omega,k} \exp i\,(\boldsymbol{k} \cdot \boldsymbol{r}_\alpha - \omega t) + c.c. \tag{5.1}$$

where $\boldsymbol{A}_{\omega,k}$ is the amplitude of the wave at frequency ω and wave vector $\boldsymbol{k}$, and $c.c.$ denotes the complex conjugate. The fields are assumed to be stationary in time and homogeneous in space, conditions that in reality are met only approximately. These assumptions may be relaxed by assuming that the fields are translation invariant on spatial scales larger than their wavelengths and stationary on temporal scales greater than the wave period. Moreover, the wave field should not contain waves of a length shorter than the inter-spacecraft separation, otherwise aliasing generates spurious results.

The correlation matrix between the measurements at two positions, $\boldsymbol{r}_\alpha$, $\boldsymbol{r}_\beta$, obeys the frequency representation

$$\mathsf{M}(\omega, \boldsymbol{r}_\alpha, \boldsymbol{r}_\beta) = \langle \boldsymbol{A}(\omega, \boldsymbol{r}_\alpha)\, \boldsymbol{A}^\dagger(\omega, \boldsymbol{r}_\beta) \rangle \tag{5.2}$$

where $\langle ... \rangle$ denotes the time (or ensemble) average. Spatial homogeneity allows linking the correlation matrix $\mathsf{M}(\omega, \boldsymbol{r}_{\alpha\beta})$ to the energy distribution matrix $\mathsf{P}(\omega, \boldsymbol{k})$ by

$$\mathsf{M}(\omega, \boldsymbol{r}_{\alpha\beta}) = \int \mathsf{P}(\omega, \boldsymbol{k})\, e^{i\boldsymbol{k}\cdot\boldsymbol{r}_{\alpha\beta}}\, d\boldsymbol{k} \tag{5.3}$$

where $\boldsymbol{r}_{\alpha\beta} = \boldsymbol{r}_\alpha - \boldsymbol{r}_\beta$. Inversion of Eqn. 5.3, i.e., estimating $\mathsf{P}(\omega, \boldsymbol{k})$ from $\mathsf{M}(\omega, \boldsymbol{r}_{\alpha\beta})$, is a difficult task since usually the data are spatially undersampled. Managing this crucial problem by constructing a series of non-linear filters is the fundamental goal of k filtering. Each filter is steered to a different $(\omega, \boldsymbol{k})$ pair and extracts from the data only the energy associated with frequency ω and wave vector $\boldsymbol{k}$. This k-filtering process can also be viewed at as a generalised minimum variance analysis [*Motschmann et al.*, 1996].

When constructing the filters, any other useful known information can be exploited. The problem of filter determination can be solved with the help of Lagrange multipliers (see Chapter 3 [*Pinçon and Motschmann*, 1998] in ISSI SR-001) yielding the following expression for the field energy distribution function $P(\omega, \boldsymbol{k})$:

$$P(\omega, \boldsymbol{k}) = \mathrm{Tr}\Big\{\mathsf{P}(\omega, \boldsymbol{k})\Big\} = \mathrm{Tr}\Big\{\Big[\mathsf{H}^\dagger(\boldsymbol{k})\, \mathsf{M}(\omega)^{-1}\, \mathsf{H}(\boldsymbol{k})\Big]^{-1}\Big\} \tag{5.4}$$

where $\mathsf{H}(\boldsymbol{k})$ is a geometrical matrix depending on the positions of the four satellites. $\mathsf{M}(\omega)$ is a matrix containing all correlation matrices $\mathsf{M}(\omega, \boldsymbol{r}_{\alpha\beta})$ constructed from the Cluster quartet, as shown in Eqn. 3.7 in Chapter 3 of ISSI SR-001. The fact that the output of

this method is an energy distribution, rather than just a single number, enables the finding of more than one wave field energy maximum at each measured frequency. In contrast to previous methods such as minimum variance analysis, this method can thus be used for wave mode identification in plasmas where several wave modes may occur at each frequency. This is a very important advantage of the k-filtering/wave-telescope technique since space plasmas usually contain a large number of wave modes that may have the same frequency. Once the various frequencies and wave vectors associated with wave field energy maxima are identified, then, as shown by *Glassmeier et al.* [1995]; *Vocks et al.* [1999]; *Motschmann et al.* [1998], a detailed discrimination of wave modes can be obtained using additional constraints (by e.g. the MHD equations).

5.3 Phase differencing

Phase differencing is a dispersion-based method relying on phase relations between the data sets obtained from different satellites. It can be applied when simultaneous data from two or more closely spaced satellite are available. A comprehensive description of the method can be found elsewhere [*Balikhin et al.*, 1997a, b; *Dudok de Wit et al.*, 1995]. This method is essentially a generalisation of the phase slowness vector method already mentioned by *Born and Wolf* [1975] and commonly used in seismology. In what follows a brief description is given.

The basic assumption of the phase differencing method is that the observed wave field can be described as:

$$\boldsymbol{A}(\boldsymbol{r},t) = \sum_{\omega} \boldsymbol{A}_{\omega} \exp i\,(\boldsymbol{k}\cdot\boldsymbol{r} - \omega t) + c.c. \tag{5.5}$$

where $\boldsymbol{A}_{\omega}$ is the Fourier wave amplitude, $\mathbf{k}$ the wave vector ($\boldsymbol{k}$ and ω are related through the wave dispersion relation), and $c.c.$ denotes the complex conjugate. As for the k-filtering technique, the wave field should ideally be stationary in time and homogeneous in space, but the same relaxation of those conditions discussed for the k filtering is assumed, and the same aliasing constraint applies as well. Contrary to the k-filtering technique, the phase differencing technique is limited to the determination of one wave vector per frequency. This limits its validity to plasma wave field for which most of the wave energy is confined to one particular mode.

Frequency decomposition of the signals $\boldsymbol{A}(\boldsymbol{r},t)$ is performed by wavelet decomposition techniques using a Morlet wavelet. This ensures good frequency resolution at the low frequencies that are of interest and a large number of frequency spectra that are used to increase the statistical robustness of the technique [*Dudok de Wit et al.*, 1995]. Hence this method can be used successfully for short periods of data. However, for best results the lowest frequency considered should ensure that there are at least 4–6 wave periods within the data period being analysed.

If the same quantity is measured by two closely spaced satellites α and β, the phase difference at a particular frequency between the two data sets is given by

$$\begin{aligned} \Delta\psi(\omega) &= \psi_{\alpha}(\omega) - \psi_{\beta}(\omega) \\ &= (\boldsymbol{k}\cdot\boldsymbol{r}_{\alpha} - \omega t) - (\boldsymbol{k}\cdot\boldsymbol{r}_{\beta} - \omega t) \\ &= |\boldsymbol{k}||\boldsymbol{r}_{\alpha\beta}|\cos(\theta_{kr}) \end{aligned} \tag{5.6}$$

where $\boldsymbol{r}_{\alpha\beta}$ is the known separation vector between the two satellites and θ_{kr} is the angle between the wave vector and satellite separation vector.

The dependence of the phase difference $\Delta\psi$ on (ω) gives the projection of the wave vector along the separation vector $\mathbf{r}_{\alpha\beta}$ as a function of frequency. With the advent of the Cluster mission, data are now available that are measured at four closely separated points in space. This enables the projection of the wave vector to be determined along three independent baselines. It is then possible to reconstruct the original $\boldsymbol{k}$ vector.

5.4 Method successes and limitations

The capabilities of the k-filtering/wave-telescope technique for multiple plasma wave mode identification have been successfully demonstrated in many key areas of the terrestrial environment: near Earth solar wind [*Glassmeier et al.*, 2001; *Narita et al.*, 2003], foreshock [*Eastwood et al.*, 2003; *Narita et al.*, 2004], through the bow shock [*Narita and Glassmeier*, 2005; *Narita et al.*, 2006a], magnetosheath near the magnetopause [*Sahraoui et al.*, 2003, 2004b; *Narita and Glassmeier*, 2006], high-altitude polar cusp [*Grison et al.*, 2005]. Not only the wave propagation direction and the wave number spectrum could be reconstructed, but also complete wave dispersion analyses or Friedrichs diagram reconstruction were accomplished using the k-filtering/wave-telescope technique [*Narita et al.*, 2003; *Schäfer et al.*, 2005]. As shown by *Sahraoui et al.* [2003], a successful identification of wave-field energy peaks actually due to aliasing can be achieved by comparing the observed wave dispersion relations with the theoretical ones.

The new technique has also been applied with remarkable success to the characterisation of the ULF turbulent magnetic fluctuations observed in the magnetosheath close to the magnetopause [*Sahraoui et al.*, 2004a, 2006] and in the terrestrial foreshock region [*Narita et al.*, 2006b]. The results obtained provide strong arguments for a weak turbulence approach [*Belmont et al.*, 2006]. A crucial point for turbulence theories is to determine the scaling law, which describes how the energy is transferred across spatial scales. Cluster estimates of the wave vector spectra associated with quasi-homogeneous magnetic field turbulence in the magnetosheath suggest that a turbulent cascade is occurring. However, due to aliasing, information about spatial scales smaller than the Cluster inter-spacecraft distance cannot be derived. At the same time, no useful information can be obtained for spatial scales much larger than the mean Cluster inter-spacecraft distance either: it can be shown that in such a case the relative uncertainty for the field energy distribution and the spatial scales are related by $\delta P/P \approx \delta\lambda/\lambda \times d/\lambda$ where d is the mean inter-spacecraft distance. As a consequence, a single tetrahedron mission like Cluster can only cover a limited range of spatial scales at a given time, typically one decade. The investigation of a turbulent cascade, from the injection to the dissipation scale, requires a broader coverage of scales. The only way to cover the various plasma fundamental scales with Cluster is by combining wave vector spectra obtained from k-filtering technique using magnetic field data sets performed at different times and for different plasma parameters and solar wind conditions. Any physical conclusion derived from these combined spectra is necessarily linked to very restrictive assumptions.

Initially, the k-filtering technique was applied to measurements of the magnetic field by the FGM and STAFF-SC instruments on Cluster. More recently, these data sets have been supplemented with EFW electric field measurements [*Tjulin et al.*, 2005]. The primary

reason behind the inclusion of the electric field data within the k-filtering technique is to obtain a better estimate of the wave-field energy distribution. This also enables some comparisons between the wave electric and magnetic field contributions to the wave energy density. These comparisons are useful for basic investigations of the polarisation of the waves. The extended technique has been applied successfully to Cluster data from the magnetosheath and the foreshock. However, its use and the interpretation of the results require an intimate knowledge of the Cluster experiments since there are a large number of problems that require solving before the electric and magnetic field measurements can be combined effectively.

From Cluster data, the phase differencing method was successfully used to identify the mode of plasma waves observed in the magnetosheath [*Balikhin et al.*, 2003a] and in the vicinity of the terrestrial bow shock [*Balikhin et al.*, 2003b]. It has been also applied to Cluster observations of foreshock waves [*Hobara et al.*, 2007a] and solitary structures [*Hobara et al.*, 2007b]. A comparison of both k filtering and phase differencing is presented in *Walker et al.* [2004]. The results show that both analysis techniques identify the same dominant wave mode in the data and the corresponding $\boldsymbol{k}$ vectors determined are in reasonable agreement. Using a wavelet transform, the dispersion based method can produce good clear results on a shorter period of data than the k-filtering technique. The phase differencing method is applied to scalar values measured at different locations such as a component of a vector (e.g., B_x or E_y) or oscillations observed in the density. This is in contrast to the k-filtering method which requires vectors measured at a minimum of four locations. It was shown that the phase differencing method works best when only one wave mode is present or when one wave mode dominates the wave environment. Multiple modes result in a number of dispersion curves and so the wave-vector directions are currently unresolvable. In contrast, the k-filtering technique can resolve multiple waves within the plasma (see Figure 5.1).

5.5 Outlook

The latest development of the phase differencing technique is its application to EFW internal burst data sets. These data sets usually contain the four individual probe potentials sampled up to 9 kHz for a period of 10–11 seconds. Thus, by analysing the phase differences observed in the electric fields on either side of the satellite it is possible to identify waves whose spatial scales are of the order of 100 m or less. This method has been used successfully by *Balikhin et al.* [2005]. The phase differencing technique can also be used to investigate the polarisation of the waves when it is applied to two perpendicular components of the electric field. This addition to the methodology was used by *Walker et al.* [2007] to distinguish between circularly polarised whistler mode waves and linearly polarised lower hybrid waves at the front of a quasi-perpendicular bow shock.

A very interesting development of the k-filtering/wave-telescope technique can be found by *Constantinescu et al.* [2006, 2007]. The new tool, called the spherical wave telescope, consists of an extension of the previous technique to spherical waves representation. It provides information about the local curvature of the wave fronts passing through the Cluster satellites. This information is then used to determine the location of the wave source. Another generalisation is presented by *Plaschke* [2007], who demonstrated that more complex phase front structures such as field-line resonances [*Glassmeier et al.*, 1999] can be incorporated into the wave-telescope technique.

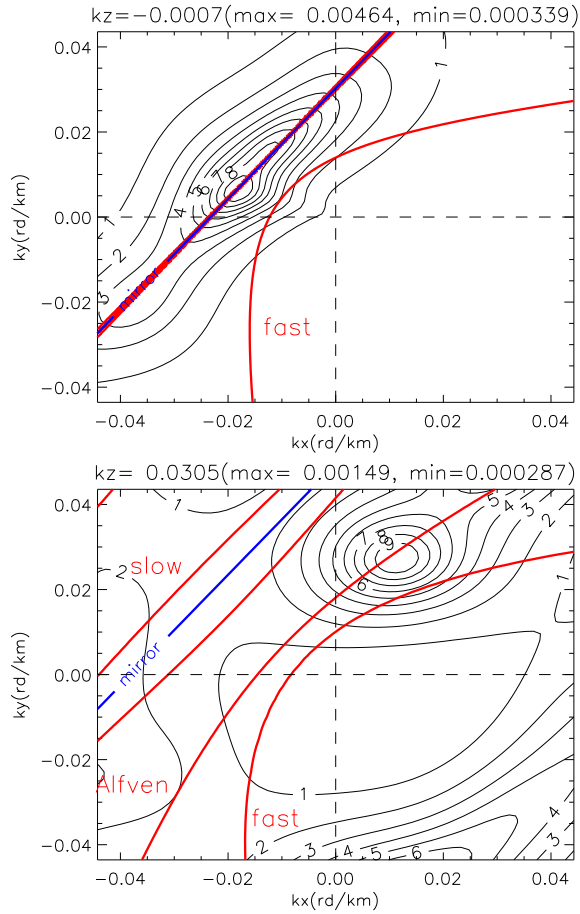

Figure 5.1: Illustration of the plasma wave mode identification capability of the k-filtering technique. In this example, the technique is applied to magnetic field fluctuations in the magnetosheath near the magnetopause, measured by the STAFF instruments on the four Cluster spacecraft. The figure displays the inferred magnetic energy (thin black lines), for a given frequency, in the (k_x, k_y) plane, at two distinct values of k_z. The coloured thick lines are the theoretical dispersion relations of the low-frequency modes. The blue line is the Doppler shift $\omega = \boldsymbol{k} \cdot \boldsymbol{v}$. Two main peaks are identified: a mirror mode (top panel) and an Alfvén wave (bottom panel). From *Walker et al.* [2004].

.

The recent results from Cluster, and particularly the $\boldsymbol{k}$ spectra determined thanks to the k-filtering/wave-telescope technique, demonstrate that future missions will have to be multi-spacecraft in order to produce new insights into the turbulent nature of space plasmas. Spacecraft separations will have to be short enough with respect to the wavelength of the maximum energy fluctuations to remove the aliasing problem. This is already planned for projects like MMS (Magnetospheric Multi-Scale Mission). Information

on larger scales will be provided by projects such as NASA'a five-spacecraft THEMIS mission. In a more distant future, projects of more sophisticated spacecraft clusters, such as the Cross-Scale project proposed in the frame of ESA's Cosmic Vision, would provide information on the various important scales simultaneously.

Bibliography

Balikhin, M., Walker, S., Treumann, R., Alleyne, H., Krasnoselskikh, V., Gedalin, M., André, M., Dunlop, M., and Fazakerley, A., 2005, Ion sound wave packets at the quasiperpendicular shock front, *Geophys. Res. Lett.*, **32**, L24106, doi:10.1029/2005GL024660.

Balikhin, M. A., Dudok de Wit, T., Alleyne, H. S. C. K., Woolliscroft, L. J. C., Walker, S. N., Krasnosel'skikh, V., Mier-Jedrzejeowicz, W. A. C., and Baumjohann, W., 1997a, Experimental determination of the dispersion of waves observed upstream of a quasi-perpendicular shock, *Geophys. Res. Lett.*, **24**, 787–790.

Balikhin, M. A., Woolliscroft, L. J. C., Alleyne, H. S. C., Dunlop, M., and Gedalin, M. A., 1997b, Determination of the dispersion of low frequency waves downstream of a quasiperpendicular collisionless shock, *Ann. Geophys.*, **15**, 143–151, http://www.ann-geophys.net/15/143/1997/.

Balikhin, M. A., Pokhotelov, O. A., Walker, S. N., Amata, E., André, M., Dunlop, M., and Alleyne, H. S. C. K., 2003a, Minimum variance free wave identification: Application to Cluster electric field data in the magnetosheath, *Geophys. Res. Lett.*, **30**, 1508, doi:10.1029/2003GL016918.

Balikhin, M. A., Pokhotelov, O. A., Walker, S. N., and André, M., 2003b, Identification of low frequency waves in the vicinity of the terrestrial bow shock, *Planet. Space Sci.*, **51**, 693–702, doi:10.1016/S0032-0633(03)00104-1.

Belmont, G., Sahraoui, F., and Rezeau, L., 2006, Measuring and understanding space turbulence, *Adv. Space Res.*, **37**, 1503–1515, doi:10.1016/j.asr.2005.01.074.

Born, M. and Wolf, E., 1975, *Principles of Optics*, Pergamon Press, Oxford.

Capon, J., 1969, High-resolution frequency- wavenumber spectrum analysis, *Proc. IEEE*, **57**, 1408–1418.

Constantinescu, O. D., Glassmeier, K.-H., Motschmann, U., Treumann, R., Fornaçon, K.-H., and Fränz, M., 2006, Plasma wave source location using CLUSTER as a spherical wave telescope, *J. Geophys. Res.*, **111**, A09221, doi:10.1029/2005JA011550.

Constantinescu, O. D., Glassmeier, K.-H., Décréau, P. M. E., Fränz, M., and Fornaçon, K.-H., 2007, Low frequency wave sources in the outer magnetosphere, magnetosheath, and near Earth solar wind, *Ann. Geophys.*, **25**, 2217–2228, http://www.ann-geophys.net/25/2217/2007/.

Dudok de Wit, T., Krasnosel'skikh, V. V., Bale, S. D., Dunlop, M. W., Lühr, H., Schwartz, S. J., and Woolliscroft, L. J. C., 1995, Determination of dispersion relations in quasi-stationary plasma turbulence using dual satellite data, *Geophys. Res. Lett.*, **22**, 2653–2656.

Eastwood, J. P., A., A. B. E., and Lucek, 2003, On the existence of Alfvén waves in the terrestrial foreshock, *Ann. Geophys.*, **21**, 1457–1465, http://www.ann-geophys.net/21/1457/2003/.

Glassmeier, K. H., Motschmann, U., and von Stein, R., 1995, Mode recognition of MHD wave fields at incomplete dispersion measurements, *Ann. Geophys.*, **13**, 76–83, http://www.ann-geophys.net/13/76/1995/.

Glassmeier, K.-H., Othmer, C., Cramm, R., et al., 1999, Magnetospheric Field Line Resonances: A Comparative Planetology Approach, *Surveys in Geophys.*, **20**, 61–109.

Glassmeier, K.-H., Motschmann, U., Dunlop, M., Balogh, A., Acuña, M. H., Carr, C., Musmann, G., Fornaçon, K.-H., Schweda, K., Vogt, J., Georgescu, E., and Buchert, S., 2001, Cluster as a wave telescope—first results from the fluxgate magnetometer, *Ann. Geophys.*, **19**, 1439–1447, http://www.ann-geophys.net/19/1439/2001/.

Grison, B., Sahraoui, F., Lavaud, B., Chust, T., Cornilleau-Wehrlin, N., Rème, H., Balogh, A., and André, M., 2005, Wave particle interactions in the high-altitude polar cusp: a Cluster case study, *Ann. Geophys.*, **23**, 3699–3713, http://www.ann-geophys.net/23/3699/2005/.

Hobara, Y., Walker, S. N., Balikhin, M., Pokhotelov, O. A., Dunlop, M., Nilsson, H., and Rème, H., 2007a, Characteristics of terrestrial foreshock ULF waves: Cluster observations, *J. Geophys. Res.*, **112**, A07202, doi:10.1029/2006JA012142.

Hobara, Y., Walker, S. N., Balikhin, M., Pokhotelov, O. A., Gedalin, M., Krasnoselskikh, V., Hayakawa, M., André, M., Dunlop, M., Rème, H., and Fazakerley, A., 2007b, Cluster observations of electrostatic solitary waves near the Earth's bow shock, *J. Geophys. Res.*, submitted.

Motschmann, U., Woodward, T. I., Glassmeier, K. H., Southwood, D. J., and Pinçon, J. L., 1996, Wavelength and direction filtering by magnetic measurements at satellite arrays: Generalized minimum variance analysis, *J. Geophys. Res.*, **101**, 4961–4966, doi:10.1029/95JA03471.

Motschmann, U., Glassmeier, K. H., and Pinçon, J. L., 1998, Multi-Spacecraft Filtering: Plasma Mode Recognition, in *Analysis Methods for Multi-Spacecraft Data*, edited by G. Paschmann and P. W. Daly, no. SR-001 in ISSI Scientific Reports, chap. 4, pp. 79–89, ESA Publ. Div., Noordwijk, Netherlands.

Narita, Y. and Glassmeier, K. H., 2005, Dispersion analysis of low-frequency waves through the terrestrial bow shock, *J. Geophys. Res.*, **110**, A12215, doi:10.1029/2005JA011256.

Narita, Y. and Glassmeier, K. H., 2006, Propagation pattern of low frequency waves in the terrestrial magnetosheath, *Ann. Geophys.*, **24**, 2441–2444, http://www.ann-geophys.net/24/2441/2006/.

Narita, Y., Glassmeier, K. H., S. Schäfer, U. M., Sauer, K., Dandouras, I., Fornaçon, K.-H., Georgescu, E., and Rème, H., 2003, Dispersion analysis of ULF waves in the foreshock using cluster data and the wave telescope technique, *Geophys. Res. Lett.*, **30**, 1710, doi:10.1029/2003GL017432.

Narita, Y., Glassmeier, K. H., Motschmann, S. S. U., Fränz, M., Dandouras, I., Fornaçon, K.-H., Georgescu, E., Korth, A., Rème, H., and Richter, I., 2004, Alfven waves in the foreshock propagating upstream in the plasma rest frame: statistics from Cluster observations, *Ann. Geophys.*, **22**, 2315–2323, http://www.ann-geophys.net/22/2315/2004/.

Narita, Y., Glassmeier, K. H., Fornaçon, K.-H., Richter, I., Schäfer, S., Motschmann, U., Dandouras, I., Rème, H., and Georgescu, E., 2006a, Low-frequency wave characteristics in the upstream and downstream regime of the terrestrial bow shock, *J. Geophys. Res.*, **111**, A01203, doi:10.1029/2005JA011231.

Narita, Y., Glassmeier, K. H., and Treumann, R. A., 2006b, Wave-Number Spectra and Intermittency in the Terrestrial Foreshock Region, *Phys. Rev. Lett.*, **97**, 191101, doi:10.1103/PhysRevLett.97.191101.

Pinçon, J.-L. and Lefeuvre, F., 1991, Local characterization of homogeneous turbulence in a space plasma from simultaneous measurements of field components at several points in space, *J. Geophys. Res.*, **96**, 1789–1802.

Pinçon, J. L. and Lefeuvre, F., 1992, The application of the generalized Capon method to the analysis of a turbulent field in space plasma: experimental constraints, *J. Atmos. Terr. Phys.*, **54**, 1237–1247.

Pinçon, J. L. and Motschmann, U., 1998, Multi-Spacecraft Filtering: General Framework, in *Analysis methods for multi-spacecraft data*, edited by G. Paschmann and P. W. Daly, ISSI SR-001, pp. 65–78, ESA Publication Division.

Plaschke, F., 2007, *Charakterisierung von Feldlinienresonanzen mit dem Wellenteleskop*, Master's thesis, TU Braunschweig.

Sahraoui, F., Pinçon, J.-L., Belmont, G., Rezeau, L., Cornilleau-Wehrlin, N., Robert, P., Mellul, L., Bosqued, J.-M., Balogh, A., Canu, P., and Chanteur, G., 2003, ULF wave identification in the magnetosheath: The k-filtering technique applied to cluster II data, *J. Geophys. Res.*, **108**, 1335, doi:10.1029/2002JA009587.

Sahraoui, F., Belmont, G., Pinçon, J.-L., Rezeau, L., Balogh, A., Robert, P., and Cornilleau-Wehrlin, N., 2004a, Magnetic turbulent spectra in the magnetosheath: new insights, *Ann. Geophys.*, **22**, 2283–2288, http://www.ann-geophys.net/22/2283/2004/.

Sahraoui, F., Pinçon, J.-L., Belmont, G., Rezeau, L., Cornilleau-Wehrlin, N., Robert, P., Mellul, L., Bosqued, J.-M., Balogh, A., Canu, P., and Chanteur, G., 2004b, Correction to "ULF wave identification in the magnetosheath: The k-filtering technique applied to cluster II data", *J. Geophys. Res.*, **109**, A04222, doi:10.1029/2004JA010469.

Sahraoui, F., Belmont, G., Rezeau, L., Cornilleau-Wehrlin, N., Pinçon, J.-L., and Balogh, 2006, Anisotropic Turbulent Spectra in the Terrestrial Magnetosheath as Seen by the Cluster Spacecraft, *Phys. Rev. Lett.*, **96**, 075002, doi:10.1103/PhysRevLett.96.075002.

Schäfer, S., Glassmeier, K.-H., Narita, Y., Fornaçon, K. H., Dandouras, I., and Fränz, M., 2005, Statistical phase propagation and dispersion analysis of low frequency waves in the magnetosheath, *Ann. Geophys.*, **23**, 3339–3349, http://www.ann-geophys.net/23/3339/2005/.

Tjulin, A., Pinçon, J.-L., Sahraoui, F., André, M., and Cornilleau-Wehrlin, N., 2005, Anisotropic Turbulent Spectra in the Terrestrial Magnetosheath as Seen by the Cluster Spacecraft, *J. Geophys. Res.*, **110**, A11224, doi:10.1029/2005JA011125.

Vocks, C., Motschmann, U., and Glassmeier, K.-H., 1999, A mode filter for plasma waves in the Hall-MHD approximation, *Ann. Geophys.*, **17**, 712–722, http://www.ann-geophys.net/17/712/1999/.

Walker, S., Sahraoui, F., Balikhin, M., Belmont, G., Pinçon, J.-L., Rezeau, L., Cornilleau-Wehrlin, N., and André, M., 2004, A comparison of wave mode identification techniques, *Ann. Geophys.*, **22**, 3021–3032, http://www.ann-geophys.net/22/3021/2004/.

Walker, S. N., Balikhin, M. A., Alleyne, H. S. C. K., Hobara, Y., André, M., and Dunlop, M., 2007, Lower hybrid waves at the shock front: A reassessment, *Ann. Geophys.*, submitted.

— 6 —

Multi-Spacecraft Turbulence Analysis Methods

TIM S. HORBURY AND KAREEM T. OSMAN
Blackett Laboratory, Imperial College London
London, United Kingdom

6.1 Introduction

Turbulence is ubiquitous in space plasmas, from the solar wind to supernova remnants, and on scales from the electron gyroradius to interstellar separations. Turbulence is responsible for transporting energy across space and between scales and plays a key role in plasma heating, particle acceleration and thermalisation downstream of shocks. Just as with other plasma processes such as shocks or reconnection, turbulence results in complex, structured and time-varying behaviour which is hard to measure with a single spacecraft. However, turbulence is a particularly hard phenomenon to study because it is usually broadband in nature: it covers many scales simultaneously. One must therefore use techniques to extract information on multiple scales in order to quantify plasma turbulence and its effects.

The Cluster orbit takes the spacecraft through turbulent regions with a range of characteristics: the solar wind, magnetosheath, cusp and magnetosphere. In each, the nature of the turbulence (strongly driven or fully evolved; dominated by kinetic effects or largely on fluid scales), as well as characteristics of the medium (thermalised or not; high or low plasma β; sub- or super-Alfvénic) mean that particular techniques are better suited to the analysis of Cluster data in different locations. In this chapter, we consider a range of methods and how they are best applied to these different regions.

Perhaps the most studied turbulent space plasma environment is the solar wind, see *Bruno and Carbone* [2005]; *Goldstein et al.* [2005] for recent reviews. This is the case for a number of reasons: it is scientifically important for cosmic ray and solar energetic particle scattering and propagation, for example. However, perhaps the most significant motivations for studying solar wind turbulence are pragmatic: large volumes of high quality measurements are available; the stability of the solar wind on the scales of hours makes it possible to identify statistically stationary intervals to analyse; and, most important of all, the solar wind speed, $\boldsymbol{V}_{SW}$, is much higher than the local MHD wave speeds. This means that a spacecraft time series is essentially a 'snapshot' spatial sample of the plasma along the flow direction, so we can consider measurements at a set of times t_i to be at a set of locations in the plasma given by $\boldsymbol{x}_i = \boldsymbol{x}_0 - \boldsymbol{V}_{SW} \cdot t_i$. This approximation, known as Taylor's hypothesis, greatly simplifies the analysis of the data. In contrast, in the magnetosheath the flow speed is lower than the wave speed and therefore temporal changes at the spacecraft are due to a complex combination of the plasma moving over the spacecraft and the turbulent fluctuations propagating in the plasma frame. This is also the case for ion and electron kinetic scale turbulence in the solar wind and dramatically complicates

the analysis of the data. As a result, the application of multi-spacecraft techniques such as k filtering to Cluster data (see Chapter 5, which make it possible to disentangle the effects of flow and wave propagation, have probably resulted in the greatest increase in our understanding of magnetosheath turbulence rather than in the solar wind.

We can therefore summarise the key advantages for plasma turbulence analysis of multi-spacecraft data sets such as those from Cluster, compared to single spacecraft data. Multiple sampling points allow us to measure how the turbulence varies in many directions, and on a range of scales, simultaneously, enabling the study of anisotropy in ways that have not previously been possible. They also allow us to distinguish between the motion of fluctuations in the plasma and motion of the plasma itself, enabling the study of turbulence in highly disturbed environments such as the magnetosheath. A number of authors have studied turbulence with Cluster data, using different techniques, the choice of which is motivated by the characteristics of the plasma environment in which they are interested. The complexity of both the Cluster data and the problem of turbulence meant that progress early in the mission was rather limited, although in the last few years several key results have been obtained and it is now a rapidly evolving topic.

At this point, it is worth noting briefly the scope of this chapter: we discuss multi-spacecraft Cluster results and methods regarding turbulence at fluid, ion and electron scales, with the emphasis on the methods more than the physical significance of the results, but we do not consider more wave-like phenomena such as those in the foreshock. This is an entirely artificial distinction, both in terms of the physics and the analysis methods. Nevertheless, this chapter is intended to be largely self-contained and we refer the reader to other chapters in this book for more information about these related topics. We also stress that this chapter is not in any way intended to be an introduction to, or overview of, the analysis and theory of space plasma turbulence, or even of Cluster results in general: instead, references to review articles are provided where appropriate. *Belmont et al.* [2006] discussed the application of k filtering to turbulence studies in much greater depth than is presented here and we refer the reader to that paper for more details. Single spacecraft analysis of Cluster data is revealing important information about turbulent anisotropy [e.g., *Mangeney et al.*, 2006; *Lacombe et al.*, 2006], dissipation processes [e.g., *Bale et al.*, 2005] and even evidence for reconnection triggered by turbulence [e.g., *Retinò et al.*, 2007] but again, we do not discuss these results further here: our emphasis is on multi-spacecraft analysis methods.

After fifty years of spacecraft measurements of turbulent space plasmas, many significant questions remain unanswered. Perhaps the three most important, both for our fundamental understanding of plasma turbulence as a process and for quantifying its large scale effects, are: anisotropy due to the presence of a background magnetic field; the nature of the dissipation process; and the origin of the spatial inhomogeneity known as intermittency. All three of these issues have been addressed using Cluster data. We discuss each briefly here in order to provide the context for the methods and results presented in later sections.

6.1.1 Anisotropy

Neutral fluid turbulence is in general isotropic. In contrast, the presence of a background magnetic field in a plasma results in anisotropy of the turbulence with respect to this direction. It has long been known that this results in fluctuations that tend to be per-

pendicular to this direction [*Belcher and Davis*, 1971], known as '2-D'. On MHD scales, the turbulent cascade is expected to preferentially transfer energy into wave vectors perpendicular to the magnetic field [see, e.g. *Oughton and Matthaeus*, 2005, for a review of these topics], resulting in longer correlation lengths along the field than those perpendicular to it, as has sometimes been observed [e.g., *Matthaeus et al.*, 1990]. This has important consequences for energetic particle transport. However, much remains unclear about this energy transfer process and the resulting 3-D structure of the magnetic field in a turbulent plasma. Cluster, by providing multiple sampling points, allows us to measure this structure in new and powerful ways.

6.1.2 Dissipation

Turbulence typically transfers energy to progressively smaller scales (higher wave numbers) until, ultimately, it is dissipated as heat. As ever, this process in collisionless plasmas is much more complex than in a collisional neutral fluid. Several mechanisms have been proposed (proton cyclotron damping, kinetic Alfvén wave damping, or even electron scale processes such as whistler damping [e.g. *Stawicki et al.*, 2001]) but at this time, the answer is not known, although wave-particle interactions are clearly involved. Ion and electron scale fluctuations can propagate much faster than MHD waves, invalidating Taylor's hypothesis and making them harder to study. It is also clear that anisotropy plays a role on these scales. Therefore, k-filtering techniques, which make it possible in principle uniquely to identify individual wave modes in the plasma, allow us to study dissipation processes in new ways.

6.1.3 Intermittency

It has long been recognised that turbulent fluctuations in neutral fluids are not spatially homogeneous. Rather, they are bursty, as anyone who has been kept awake on a stormy night can attest. This burstiness is commonly known as intermittency and is now recognised as a fundamental property of turbulence [e.g. *Frisch*, 1996]. It has been extensively studied in neutral fluids, where its effects are at least relatively well understood: by producing some regions with large velocity shears on a particular scale and others with only small ones, it results in spatial variations in the energy transfer rate. Its spontaneous origin in a turbulent fluid, as well as its 3-D structure, is much less well understood but is clearly a fundamental aspect of hydrodynamic turbulence. It is now also well established in space plasmas [*Bruno and Carbone*, 2005] but in this case its effects are less clear since there is not such a simple relationship between velocity shear and energy transfer as in neutral fluids. Since intermittency is related to spatial variability, multi-spacecraft Cluster data are a unique resource for studying this important phenomenon.

6.2 The k-filtering technique

The k-filtering technique was described in Chapters 3 and 4 of ISSI SR-001, and Chapter 5 of the present book describes its success in identifying wave phenomena. It is this method which has produced the most dramatic results in turbulence studies, since it makes

it possible to measure the power held in discrete wave vectors within the plasma, independent of any assumption of Taylor's hypothesis. It has been used widely to analyse waves in a range of locations and we refer the reader to Chapter 5 of this book for more details. However, it has also been used very successfully to study turbulent magnetosheath fluctuations and it is these results on which we concentrate here.

The magnetosheath [*Lucek et al.*, 2005] is composed of plasma which has recently passed through the Earth's bow shock. As a result, it is very variable and highly disturbed with large variations in velocity, magnetic field and density. This is in contrast to the solar wind, where density variations are rather small. One would therefore expect a more dominant role for compressive fluctuations in the magnetosheath than the solar wind. The sheath is also a much harder medium to study than the solar wind because the plasma wave speeds are comparable with, or larger than, the flow past the spacecraft. This means that variations at a single spacecraft are a combination of fluctuations being convected past the spacecraft and those fluctuations themselves propagating and changing. As a result, single spacecraft analysis of magnetosheath turbulence has been rather limited and Cluster offers the opportunity to make considerable progress in understanding this medium. The k-filtering method is ideal for this purpose and it has been very successfully applied by *Sahraoui et al.* [2006] in studying magnetosheath turbulence.

These authors analysed turbulence in the magnetosheath near the magnetopause. In this case, there are therefore three physically important directions: the plasma flow vector; the local magnetic field direction; and the normal to the magnetopause, along which one might expect the plasma to be compressed. *Sahraoui et al.* [2006] studied an interval with large amplitude variations in both the magnetic field amplitude and direction. They showed that the interval was marginally unstable to the mirror instability and, using k filtering to identify power at particular wave vectors, that mirror mode fluctuations were present at relatively large scales (low spacecraft frequencies). For the first time, using k filtering, *Sahraoui et al.* could recover the power spectrum as a function of wave vector in the three important directions and showed that there was essentially no cascade along the magnetic field direction, as has been predicted by some theories of plasma turbulence. In contrast, there appeared to be a strong cascade along the flow direction. *Sahraoui et al.* concluded that the mirror instability generated variations which then cascaded to smaller scales (smaller than an ion gyroradius) along the flow direction, and to a lesser extent the magnetopause normal direction. Interestingly, the power scales with flow-parallel wave number as $k^{-8/3}$, with an exponent considerably larger (and hence a steeper spectrum) than that predicted by theory. *Sahraoui et al.* argued that directions such as the magnetic field vector and the magnetopause normal constrain the development of the turbulent cascade, limiting the energy transfer in those directions, while energy cascaded freely along the flow direction. The results of *Sahraoui et al.* [2006] could only be obtained using data from four spacecraft and analysing them with k filtering. This is an example of the large amounts of information that can be retrieved from spacecraft data using this method.

The k-filtering technique is also of use in other environments. Recently, *Tjulin et al.* [2007] applied k filtering to unusually large amplitude broadband waves around a solar wind discontinuity which had previously been shown to be affected by reconnection. They exploited the enhancement to k filtering developed by *Tjulin et al.* [2005] which combines magnetic and electric field data to further constrain the possible results, and also recovers polarisation results. *Tjulin et al.* measured the plasma frame wave vector spectrum of the waves and showed that there were two main components. One, a left handed long

wavelength shear Alfvén wave, was propagating along the background magnetic field. The other, a fast magnetosonic right-handed wave, was propagating along the normal to the discontinuity. The remarkably detailed information retrieved by *Tjulin et al.* is a testament to the power of the k-filtering technique in characterising plasma fluctuations using multi-spacecraft data.

Narita et al. [2007] used k filtering to study broadband fluctuations in a number of environments: the solar wind, foreshock, magnetosheath and cusp. In particular, they distinguished 'Alfvénic' (wave vectors parallel to $\boldsymbol{B}$), '2-D' (wave vectors perpendicular to $\boldsymbol{B}$) and 'compressive' fluctuations, and measured the spectrum of each. In common with much earlier work, they found a predominance of 2-D fluctuations in solar wind turbulence, and a much lower level of compressive fluctuations. They found a spectral index of around -1.9, rather steeper than the consensus -5/3 value, for MHD-scale fluctuations and even steeper at higher wave vectors. Fluctuation levels increased dramatically in the magnetosheath behind the shock, and *Narita et al.* [2007] concluded that this could not come simply from compression, but needed an additional source such as mirror modes.

The foreshock itself was studied in more detail by *Narita et al.* [2006] who again used k filtering. While the relatively dynamically mature turbulence in the solar wind has long been studied, the foreshock has perhaps been the subject of less work—and is also interesting because it is dynamically young, being generated locally by wave-particle interactions. *Narita et al.* [2006] showed that even in this case, the turbulence was in many ways similar to that in the solar wind, being highly anisotropic and with a -5/3 spectral index. They also argued that the fluctuations were intermittent, and that they were probably an example of weak turbulence.

Given the success of k filtering in measuring power at different wave vectors, why then would one use any other technique? In practice, like every technique, k filtering has its limitations. In particular, *Tjulin et al.* [2005] pointed out that there is a fundamental limit to the number of wave vectors that can be resolved at a given spacecraft frequency, given by $(NL-1)$, where N is the number of spacecraft and L is the number of parameters used in the analysis, and in practice is typically 3 for a vector such as the magnetic field. For Cluster, this therefore results in a limit of 11 wave vectors. This is ample when analysing discrete waves, but when a broadband turbulent spectrum is present, it may limit what can be analysed in practice. *Tjulin et al.* [2005] also pointed out that there must be enough points in the analysed time series to provide a reliable power estimate at an acceptable frequency resolution—in practice, this is typically a few thousand points.

A further limitation of the k-filtering method, which is common to all the multi-spacecraft techniques discussed in this paper, is that it is restricted to scales (or, equivalently, wave vectors) close to those of the spacecraft separations: one cannot probe variations on scales much smaller, or much larger, than this.

6.3 Phase differencing

In addition to k filtering, other methods can be used to determine the properties of waves in the magnetosheath. In their study of magnetosheath fluctuations, *Balikhin et al.* [2003] used the 'phase-differencing' method which is essentially a technique to determine the relative time at which wavefronts pass the four Cluster spacecraft. By using wavelets to filter the data to various frequencies, they constructed a dispersion curve for the fluctua-

tions and concluded that they were mirror modes. However, a key restriction of the phase differencing method is that it can only be used when there is one dominant wave vector at each spacecraft frequency, in contrast to k filtering which can in principle measure power in many wave vectors simultaneously. *Walker et al.* [2004] have compared the k filtering and phase differencing approaches in detail with an example interval of magnetosheath fluctuations.

6.4 Correlation-based methods

In addition to the spectral-based methods of k filtering and phase differencing, methods based on cross-correlations between spacecraft have been used. *Matthaeus et al.* [2005] used data from Cluster, as well as the ACE and Wind spacecraft, to measure the correlation function of the solar wind magnetic field on a huge range of scales, from 150 km to 350 R_E. By cross-correlating time series from two spacecraft a distance r apart, *Matthaeus et al.* [2005] were able to measure the spatial correlation function at that separation. Assuming isotropy, and using many intervals of data from different spacecraft pairs, they constructed the plasma frame correlation function. They then used this to estimate two key parameters of the turbulence. One is the 'outer' or correlation scale which they found to be around 186 R_E. The second, the 'inner' or Taylor microscale, is related to the characteristic scale of the spatial derivatives of the magnetic field fluctuations and can be measured from the curvature of the correlation function as it approaches zero separation. From these two values, *Matthaeus et al.* estimated the effective Reynolds number of solar wind turbulence to be around 230,000—this large value is consistent with the highly turbulent nature of the solar wind. By using zero time lag cross-correlations, *Matthaeus et al.* were immune to any finite wave propagation speed effects—in other words, the breakdown of Taylor's hypothesis. In practice, as we have seen this is not an issue in the solar wind, but this method could be used in other regions such as the magnetosheath where Taylor's hypothesis is not well satisfied.

While *Matthaeus et al.* [2005] combined data from several spacecraft, they did not consider the issue of anisotropy with respect to the magnetic field direction. *Horbury* [2000] described a method to recover information about anisotropy by using cross-correlations between spacecraft at varying time lags. If two spacecraft, 1 and 2, are separated by a vector $\boldsymbol{r}_{12}$, then the zero time lag cross-correlation corresponds to a plasma frame separation of $\boldsymbol{r}_{12}$, as used by *Matthaeus et al.* [2005]. However, non-zero time lags Δt correspond to different separations in the plasma frame $\boldsymbol{x}(\Delta t) = \boldsymbol{r}_{12} - \boldsymbol{V}_{SW} \cdot \Delta t$ where $-\boldsymbol{V}_{SW}$ is the solar wind velocity relative to the spacecraft. Since the two spacecraft will in general not be separated exactly along the flow direction, this allows us to measure variations in the plasma in directions perpendicular to the flow. Four spacecraft provide 6 pairs between which to compare. If one assumes axi-symmetry of the turbulence with respect to the local magnetic field direction—a commonly-used assumption, without which it is difficult to make progress—then one can measure the plasma frame autocorrelation function at a reasonable range of scales and directions relative to the field, making it possible to measure the shape of the function. In particular, it is then possible to study the anisotropy of the fluctuations.

For such inter-spacecraft comparisons, *Horbury* [2000] pointed out that Taylor's hypothesis becomes a slightly more complex condition than for the single spacecraft case,

with it being better satisfied for some time lags, but worse for others. A detailed description is given by *Osman and Horbury* [2007]. In the solar wind, for reasonable spacecraft formations, the condition is in practice almost always satisfied. As with k filtering, in practice the correlation method only provides 3-D information on scales comparable to the spacecraft separation. In order to study inertial range fluctuations, one needs to have data when the spacecraft are considerably further apart than the proton gyroradius. In 2006, the Cluster dayside separation was 10,000 km, which is sufficient for these studies.

Osman and Horbury [2007] recently implemented the *Horbury* [2000] method to study Cluster solar wind data from 2006 and demonstrated that it can be used to recover information about the turbulent fluctuations. In particular, they showed that, with judicious selection of scales and time lags, they could retrieve the plasma frame autocorrelation function over a wide range of angles relative to the local magnetic field direction and hence estimate the level of anisotropy. As expected, and in agreement with earlier work, this showed a significantly longer correlation length along the field than across it, consistent with an anisotropic turbulence cascade.

One key advantage of this method is that one can construct an estimate of the plasma frame autocorrelation function, as a function of both angle and scale, with a short data set: Osman and Horbury used intervals of around 40 minutes, effectively limited only by the need to have enough data points to adequately reduce errors in the cross-correlation estimates. This makes it possible to take 'snapshots' of the turbulent anisotropy in different regions, such as corotating interaction regions, fast and slow wind, or within coronal mass ejections. Indeed, Osman and Horbury analysed several intervals and found unexpected variations in the anisotropy properties, which did not seem to be correlated with variations in other solar wind parameters such as speed or plasma β.

The correlation method, then, is rather different from k filtering. Some differences are practical: the correlations are very rapid to calculate, while k filtering is computationally intensive. Some, however, are more subtle. The k-filtering method assumes that the fluctuations can be described by a population of plane waves with discrete ω and $\boldsymbol{k}$, while the correlation method does not. This may prove advantageous in turbulence studies in particular, where the fluctuations are broadband, nonlinear and indeed for strong turbulence, perhaps not wave-like at all.

6.5 Other techniques

In addition to the 'formal' techniques such as k filtering and cross-correlations, the complexity and fine scale structure of turbulent plasmas has motivated a number of studies which use rather more pragmatic ways to combine data from more than one spacecraft to extract information about turbulent space plasmas.

Alexandrova et al. [2006] used multi-spacecraft data in a rather different manner in order to elucidate the nature of discrete structures that they identified in the magnetosheath at frequencies near the ion cyclotron frequency. Using Morlet wavelets to filter out other signals from the time series, they showed that the enhanced power at these frequencies was composed of discrete structures—that is, it was intermittent. By finding the relative times at which these structures passed the four spacecraft, *Alexandrova et al.* deduced that these structures were Alfvénic 'vortex filaments', cylindrical structures approximately parallel to the magnetic field and propagating perpendicular to it. *Alexandrova et al.* argued that

these structures are an important element in magnetosheath turbulence. This is an excellent example of where a combination of techniques, wavelet filtering plus relatively simple timing analysis, can be used with multi-spacecraft data to reveal additional information about turbulence than can be recovered with a single spacecraft.

The Earth's plasma sheet is a highly structured and dynamic environment, which is strongly influenced by processes such as reconnection occurring in other locations in the magnetosphere. It is often highly turbulent, but this turbulence is hard to study because of rapidly varying plasma flows and wave speeds that are comparable in magnitude to these motions. *Vörös et al.* [2007] have recently used statistical techniques to study intermittency in the plasma sheet. In particular, by taking advantage of a situation when one spacecraft was within the bulk flow of the plasma sheet while another was at the boundary, they argued that strong velocity shear at the edges of the plasma flows rapidly redistributes energy via turbulent non-local couplings, a process which is theoretically expected but not previously observed in the magnetosphere.

The cusp is another structured and dynamic near-Earth environment that is hard to study with single spacecraft data. *Nykyri et al.* [2003] studied waves near the proton cyclotron frequency in the high-altitude cusp: by considering the different power levels present at various spacecraft, they could place an upper limit on the spatial extent of the wave region. *Nykyri et al.* presented one interval where large power variations occurred between spacecraft only 100 km apart. Good correlation between spacecraft only occurred when they were approximately aligned along a field line, demonstrating that the waves were located on particular flux tubes. *Nykyri et al.* [2003] concluded that these waves, occurring in regions of strong shear, were highly filamentary and structured.

Sundkvist et al. [2005] also studied the cusp plasma and used electric and magnetic field data from several Cluster spacecraft to argue that Drift-Kinetic Alfvén (DKA) vortices were present, on scales of the ion gyroradius, about 25km in this case. DKA vortices are predicted to form in non-uniform environments, such as the cusp, under certain plasma conditions and can have an important effect on plasma transport. *Sundkvist et al.* identified the vortices by comparing the field profiles at several nearby spacecraft with those of a model vortex: this is another example of the use of multi-spacecraft data in a less formalised method which can still reveal important information about the turbulent nature of the plasma.

6.6 Summary and prospects for the future

It is clear from the studies discussed here that, as with many other aspects of multi-spacecraft analysis, progress can be made through a combination of techniques, some sophisticated and some much less so: one must choose the best tool for the purpose at hand.

Studies of turbulence using multi-spacecraft data are in their infancy. The k-filtering method holds great promise and has been applied to a wide range of turbulent regions, although much remains to be done in retrieving physical parameters of interest. Work on constraining the results with multiple data sets and other physical requirements may prove useful, for example in probing the helicity of turbulent fluctuations. The much cruder correlation method is much less developed. It remains to be seen whether this will offer significant benefits over other methods or simply a complementary viewpoint. The funda-

mental constraint on multi-spacecraft techniques, of being limited to spatial scales close to the spacecraft separation, can only be alleviated by identifying spacecraft data sets with the required separation. It is encouraging that work is beginning using this approach in the solar wind on much larger scales than the Cluster separation. More advanced techniques will hopefully be applied to these data in the future.

Finally, further in the future, a multi-spacecraft mission such as the Cross-Scale project, proposed in the frame of ESA's Cosmic Vision, offers the prospect of measuring, for the first time, the properties of turbulent fluctuations over many orders of magnitude in scale simultaneously. Only in this way can we hope to quantify the broadband nonlinear coupling between scales that is the key characteristic, and still poorly understood controlling influence, of plasma turbulence and all its effects.

Acknowledgements

This work was supported by the Science and Technology Funding Council. The authors are grateful to Elizabeth Lucek for useful discussions regarding this review.

Bibliography

Alexandrova, O., Mangeney, A., Maksimovic, M., Cornilleau-Wehrlin, N., Bosqued, J.-M., and André, M., 2006, Alfvén vortex filaments observed in magnetosheath downstream of a quasi-perpendicular bow shock, *J. Geophys. Res.*, **111**, A12208, doi:10.1029/2006JA011934.

Bale, S. D., Kellogg, P. J., Mozer, F. S., Horbury, T. S., and Rème, H., 2005, Measurement of the Electric Fluctuation Spectrum of Magnetohydrodynamic Turbulence, *Phys. Rev. Lett.*, **94**, 215002, doi:10.1103/PhysRevLett.94.215002.

Balikhin, M. A., Pokhotelov, O. A., Walker, S. N., Amata, E., André, M., Dunlop, M., and Alleyne, H. S. C. K., 2003, Minimum variance free wave identification: Application to Cluster electric field data in the magnetosheath, *Geophys. Res. Lett.*, **30**, 1508, doi:10.1029/2003GL016918.

Belcher, J. W. and Davis, L., Jr., 1971, Large-amplitude Alfvén waves in the interplanetary medium, 2., *J. Geophys. Res.*, **76**, 3534–3563.

Belmont, G., Sahraoui, F., and Rezeau, L., 2006, Measuring and understanding space turbulence, *Adv. Space Res.*, **37**, 1503–1515, doi:10.1016/j.asr.2005.01.074.

Bruno, R. and Carbone, V., 2005, The Solar Wind as a Turbulence Laboratory, *Living Reviews in Solar Physics*, **2**, 4.

Frisch, U., 1996, *Turbulence*, Turbulence, by Uriel Frisch, pp. 310. ISBN 0521457130. Cambridge, UK: Cambridge University Press, January 1996.

Goldstein, M. L., Eastwood, J. P., Treumann, R. A., Lucek, E. A., Pickett, J., and Décréau, P., 2005, The Near-Earth Solar Wind, *Space Sci. Rev.*, **118**, 7–39, doi:10.1007/s11214-005-3823-4.

Horbury, T. S., 2000, Cluster II Analysis of Turbulence using Correlation Functions, in *Cluster-II Workshop: Multiscale/Multipoint Plasma Measurements*, edited by R. A. Harris, ESA SP-449, p. 89, ESA Publ. Div., Noordwijk, Netherlands.

Lacombe, C., Samsonov, A. A., Mangeney, A., Maksimovic, M., Cornilleau-Wehrlin, N., Harvey, C. C., Bosqued, J.-M., and Trávníček, P., 2006, Cluster observations in the magnetosheath—Part 2: Intensity of the turbulence at electron scales, *Ann. Geophys.*, **24**, 3523–3531, http://www.ann-geophys.net/24/3523/2006/.

Lucek, E. A., Constantinescu, D., Goldstein, M. L., Pickett, J., Pinçon, J. L., Sahraoui, F., Treumann, R. A., and Walker, S. N., 2005, The Magnetosheath, *Space Sci. Rev.*, **118**, 95–152, doi:10.1007/s11214-005-3825-2.

Mangeney, A., Lacombe, C., Maksimovic, M., Samsonov, A. A., Cornilleau-Wehrlin, N., Harvey, C. C., Bosqued, J.-M., and Trávníček, P., 2006, Cluster observations in the magnetosheath—Part 1: Anisotropies of the wave vector distribution of the turbulence at electron scales, *Ann. Geophys.*, **24**, 3507–3521, http://www.ann-geophys.net/24/3507/2006/.

Matthaeus, W. H., Goldstein, M. L., and Roberts, D. A., 1990, Evidence for the presence of quasi-two-dimensional nearly incompressible fluctuations in the solar wind, *J. Geophys. Res.*, **95**, 20 673–20 683.

Matthaeus, W. H., Dasso, S., Weygand, J. M., Milano, L. J., Smith, C. W., and Kivelson, M. G., 2005, Spatial Correlation of Solar-Wind Turbulence from Two-Point Measurements, *Phys. Rev. Lett.*, **95**, 231101, doi:10.1103/PhysRevLett.95.231101.

Narita, Y., Glassmeier, K.-H., and Treumann, R. A., 2006, Wave-Number Spectra and Intermittency in the Terrestrial Foreshock Region, *Phys. Rev. Lett.*, **97**, 191101, doi:10.1103/PhysRevLett.97.191101.

Narita, Y., Glassmeier, K.-H., Goldstein, M. L., and Treumann, R. A., 2007, Cluster observations of shock-turbulence interactions, in *Turbulence and Nonlinear Processes in Astrophysical Plasmas*, edited by D. Shaikh and G. P. Zank, 6th Annual International Astrophysical Conference, pp. 215–220, Am. Inst. Phys.

Nykyri, K., Cargill, P. J., Lucek, E. A., Horbury, T. S., Balogh, A., Lavraud, B., Dandouras, I., and Rème, H., 2003, Ion cyclotron waves in the high altitude cusp: CLUSTER observations at varying spacecraft separations, *Geophys. Res. Lett.*, **30**, 2263, doi:10.1029/2003GL018594.

Osman, K. T. and Horbury, T. S., 2007, Multispacecraft Measurement of Anisotropic Correlation Functions in Solar Wind Turbulence, *Astrophys. J.*, **654**, L103–L106, doi:10.1086/510906.

Oughton, S. and Matthaeus, W. H., 2005, Parallel and perpendicular cascades in solar wind turbulence, *Nonlin. Proc. Geophys.*, **12**, 299–310, http://www.nonlin-processes-geophys.net/12/299/2005/.

Retinò, A., Sundkvist, D., Vaivads, A., Mozer, F., André, M., and Owen, C. J., 2007, In situ evidence of magnetic reconnection in turbulent plasma, *Nature Physics*, **3**, 236–238, doi:10.1038/nphys574.

Sahraoui, F., Belmont, G., Rezeau, L., Cornilleau-Wehrlin, N., Pinçon, J. L., and Balogh, A., 2006, Anisotropic Turbulent Spectra in the Terrestrial Magnetosheath as Seen by the Cluster Spacecraft, *Phys. Rev. Lett.*, **96**, 075002, doi:10.1103/PhysRevLett.96.075002.

Stawicki, O., Gary, S. P., and Li, H., 2001, On magnetic fluctuation spectra in the solar wind and the influence of mode dispersion, in *International Cosmic Ray Conference*, vol. 8 of *International Cosmic Ray Conference*, p. 3322.

Sundkvist, D., Krasnoselskikh, V., Shukla, P. K., Vaivads, A., André, M., Buchert, S., and Rème, H., 2005, In situ multi-satellite detection of coherent vortices as a manifestation of Alfvénic turbulence, *Nature*, **436**, 825–828, doi:10.1038/nature03931.

Tjulin, A., Pinçon, J.-L., Sahraoui, F., André, M., and Cornilleau-Wehrlin, N., 2005, The k-filtering technique applied to wave electric and magnetic field measurements from the Cluster satellites, *J. Geophys. Res.*, **110**, A011224, doi:10.1029/2005JA011125.

Tjulin, A., Lucek, E. A., and Dandouras, I., 2007, Characterization of waves in the vicinity of an interplanetary directional discontinuity, *J. Geophys. Res.*, **112**, A12104, doi:10.1029/2007JA012471.

Vörös, Z., Baumjohann, W., Nakamura, R., Runov, A., Volwerk, M., Takada, T., Lucek, E. A., and Rème, H., 2007, Spatial structure of plasma flow associated turbulence in the Earth's plasma sheet, *Ann. Geophys.*, **25**, 13–17, http://www.ann-geophys.net/25/13/2007/.

Walker, S., Sahraoui, F., Balikhin, M., Belmont, G., Pinçon, J., Rezeau, L., Alleyne, H., Cornilleau-Wehrlin, N., and André, M., 2004, A comparison of wave mode identification techniques, *Ann. Geophys.*, **22**, 3021–3032, http://www.ann-geophys.net/22/3021/2004/.

— 7 —

Proper Frame Determination and Walén Test

GÖTZ PASCHMANN
Max-Planck-Institut für extraterrestrische Physik
Garching, Germany

BENGT U. Ö. SONNERUP
Thayer School of Engineering, Dartmouth College
Hanover, New Hampshire, USA

7.1 Introduction

To study structures, such as current sheets, flux ropes, or fully three-dimensional configurations, it is desirable to examine them in their proper (co-moving) frame, in which they appear as time stationary as the data permit. And it is important to establish the frame velocity so that their physical dimensions can be determined. In the present chapter, we discuss methods for finding the velocity of the proper frame, mostly from single spacecraft data. The so-called Walén test is also discussed in the chapter. Its purpose is to identify one-dimensional Alfvénic structures from single-spacecraft data, usually in the context of magnetic field reconnection geometries or interplanetary discontinuities.

The simplest situation is one where the electric field in the proper frame is negligibly small. When such is the case, the co-moving frame is called the deHoffmann-Teller (HT) frame. It was first applied by *de Hoffmann and Teller* [1950] in a theoretical study of the one-dimensional structure of MHD shocks. In this application, the HT frame was specified by the requirement that the electric field on both sides of the shock, but not necessarily in the middle of it, was zero. In other words, the plasma flow on the two sides was field-aligned, when viewed in the HT frame. The component of the frame velocity, $\boldsymbol{V}_{\mathrm{HT}}$, along the direction normal to a one-dimensional layer represents the motion of the layer, while the tangential component represents what has been called the field-line velocity. Important applications of the HT frame include the study of particle reflection and acceleration at shocks (see Section 8.2.1), at the magnetopause, and in the geomagnetic tail current sheet. It is also used in the Grad-Shafranov reconstruction methods presented in Chapter 9.

The concept of an HT frame is not limited to one-dimensional structures. Such a frame can exist for some two- and three-dimensional objects as well. But there are also structures which possess an intrinsic electrostatic field that cannot be transformed away . An example is the standard two-dimensional reconnection configuration, which, in its proper frame (the frame moving with the X-line), has a remnant electric field along the invariant (axial) direction. Determination of the magnitude of this reconnection-generated field is an important goal. To reach it, a high-quality determination of the proper frame is required.

The procedure, first developed in *Sonnerup et al.* [1987], for obtaining the HT frame velocity and, if so desired, its acceleration, from data measured by a single spacecraft was described in Chapter 9 of ISSI SR-001 [*Khrabrov and Sonnerup*, 1998]. Comments on the procedure and applications are given in Section 7.2 below. The more general situations, in which no HT frame exists, i.e., where the structures have an intrinsic remaining electrostatic field in their proper frame are discussed in Section 7.3.

7.2 The deHoffmann-Teller frame

As shown in Chapter 9 of ISSI SR-001, the procedure for determining a HT frame consists of finding the transformation velocity, $\boldsymbol{V}_{\mathrm{HT}}$, from the spacecraft frame to the HT frame that minimises the residual electric field in the least-squares sense. This is accomplished by minimising the object function

$$D(\boldsymbol{V}) = \langle |\boldsymbol{E}'|^2 \rangle = \langle |\boldsymbol{E} + \boldsymbol{V} \times \boldsymbol{B}|^2 \rangle \tag{7.1}$$

with respect to the frame velocity, $\boldsymbol{V}$. Here the angle brackets $\langle \dots \rangle$ denote the average over the data set used in the calculation. The minimum corresponds to $\boldsymbol{V} = \boldsymbol{V}_{\mathrm{HT}}$. In other words, $\boldsymbol{V}_{\mathrm{HT}}$ is determined from least-squares fitting of $-\boldsymbol{V}_{\mathrm{HT}} \times \boldsymbol{B}^i$ to the measured electric field vectors $\boldsymbol{E}^i$. The components of $\boldsymbol{V}_{\mathrm{HT}}$ satisfy the equation $\langle \boldsymbol{E}' \times \boldsymbol{B} \rangle$=0, where the electric field in the co-moving frame is $\boldsymbol{E}' = \boldsymbol{E} + \boldsymbol{V} \times \boldsymbol{B}$. In matrix form, the equations for the frame velocity components become

$$\begin{pmatrix} \langle B_y^2 + B_z^2 \rangle & \langle -B_x B_y \rangle & \langle -B_x B_z \rangle \\ \langle -B_x B_y \rangle & \langle B_x^2 + B_z^2 \rangle & \langle -B_y B_z \rangle \\ \langle -B_x B_z \rangle & \langle -B_y B_z \rangle & \langle B_x^2 + B_y^2 \rangle \end{pmatrix} \begin{pmatrix} V_x \\ V_y \\ V_z \end{pmatrix} = \begin{pmatrix} \langle E_y B_z - E_z B_y \rangle \\ \langle E_z B_x - E_x B_z \rangle \\ \langle E_x B_y - E_y B_x \rangle \end{pmatrix} \tag{7.2}$$

The uncertainties in the $\boldsymbol{V}_{\mathrm{HT}}$ determination are discussed in detail in Chapter 9 of ISSI SR-001.

If only the electric field components in the spacecraft spin plane are measured, but not the spin-axis component, one commonly used procedure is to calculate the spin-axis component by use of the assumption $\boldsymbol{E}^i \cdot \boldsymbol{B}^i = 0$, although this procedure is not always physically justified and also gives problems when $\boldsymbol{B}$ lies near the spin plane. Another option is described in Section 7.3.1.

In case no direct electric field measurements are available, but plasma velocities are, the $\boldsymbol{E}^i$ vectors are replaced by $-\boldsymbol{v}^i \times \boldsymbol{B}^i$. Using $-\boldsymbol{v}^i \times \boldsymbol{B}^i$ as proxy for the electric field has been the standard procedure in the past, commonly based on ion bulk velocities.

If reliable electron bulk velocities are available, they offer a considerable advantage, as pointed out in Chapter 9 of ISSI SR-001 and by *Puhl-Quinn and Scudder* [2000]. Ion and electron bulk velocities will differ as soon as there are significant electric currents, $\boldsymbol{j} = ne(\boldsymbol{v}_i - \boldsymbol{v}_e)$. In this case, the use of the electron velocities is the better choice, because the magnetic field lines are more closely tied to the electron fluid. In terms of the generalised Ohm's law, it implies that the Hall electric field, which can be significant, is incorporated in the analysis.

As discussed in Section 9.2 of ISSI SR-001, the HT frame participates in the motion of a boundary or other discontinuity. Thus $\boldsymbol{V}_{\mathrm{HT}} \cdot \hat{\boldsymbol{n}}$ represents the velocity of motion of the discontinuity along its normal, assuming a good normal vector is known (see also

Section 10.5.5 [*Schwartz*, 1998] of ISSI SR-001). In Chapter 1 of the present volume, methods for determining normals are discussed, and so are other methods to determine discontinuity speeds from single spacecraft measurements, such as the Minimum Faraday Residue (MFR) and Minimum Mass-flux Residue (MMR) methods.

7.3 General proper frame

Here we discuss the more general situation where no ideal HT frame exists, but where a proper frame (in which the structure is time independent but has an intrinsic electrostatic field distribution) does exist: it is this frame that one wants to find.

7.3.1 One-dimensional structures

In one-dimensional structures such as shocks, rotational and tangential discontinuities there can be, and probably often is, an intrinsic electric field, E_n, along the normal within the layer itself. The presence of such an electric field can adversely influence the quality of the determination of the proper velocity from the standard HT algorithm. And this intrinsic field, with its associated electric potential, is itself of importance in understanding some of the physical processes operating in the layer. Therefore it is desirable to properly incorporate the intrinsic field in the analysis. Perhaps the simplest way to achieve this goal is to manually exclude data points within the layer and simply apply the standard HT algorithm to electric field data or to $-\boldsymbol{v} \times \boldsymbol{B}$ data taken on the two sides. After $\boldsymbol{V}_{\rm HT}$ has been found in this manner, transforming the electric field within the layer to the HT frame should produce the desired intrinsic field and potential. Ideally this electric field should come from direct three-dimensional field measurements. By then examining the portions contributed separately by $-\boldsymbol{v} \times \boldsymbol{B}$ and by $-\boldsymbol{v}_e \times \boldsymbol{B}$, one can assess the individual contributions in Ohm's law from the convection electric field, from the Hall field, and from the electron pressure gradient.

An alternate approach (as yet untested) is to transform the measured electric field near and within the layer to a frame of reference in which only the tangential part of the electric field is minimised. The appropriate object function for minimisation with respect to the three components of the frame velocity, $\boldsymbol{V}$, is then

$$D(\boldsymbol{V}) = \langle |\hat{\boldsymbol{n}} \times (\boldsymbol{E} + \boldsymbol{V} \times \boldsymbol{B}|^2 \rangle \tag{7.3}$$

Here $\hat{\boldsymbol{n}}$ is the normal vector, assumed known, and, as before, the angle brackets $\langle \dots \rangle$ denote the average over the data set. Using a right-handed coordinate system, defined by a set of unit vectors $(\hat{\boldsymbol{x}}_1, \hat{\boldsymbol{x}}_2, \hat{\boldsymbol{x}}_3)$, with $\hat{\boldsymbol{n}} = \hat{\boldsymbol{x}}_3$, the minimisation leads to the following matrix equation for the velocity components:

$$\begin{pmatrix} \langle B_3 B_3 \rangle & 0 & -\langle B_1 B_3 \rangle \\ 0 & \langle B_3 B_3 \rangle & -\langle B_2 B_3 \rangle \\ -\langle B_1 B_3 \rangle & -\langle B_2 B_3 \rangle & \langle B_1^2 + B_2^2 \rangle \end{pmatrix} \begin{pmatrix} V_1 \\ V_2 \\ V_3 \end{pmatrix} = \begin{pmatrix} \langle E_2 B_3 \rangle \\ -\langle E_1 B_3 \rangle \\ \langle E_1 B_2 - E_2 B_1 \rangle \end{pmatrix} \tag{7.4}$$

In the frame of reference moving with velocity $\boldsymbol{V}$, the electric field should then be zero, or close to zero, except for an intrinsic electric field within the layer, directed along $\hat{\boldsymbol{n}}$. This field can then be integrated to give the electric potential distribution and net potential jump.

The two tangential velocity components, V_1 and V_2, become undefined for a perfect tangential discontinuity (TD), i.e., for $B_3 = 0$. For this case, Eqn. 7.4 then gives $V_3 = \langle E_1 B_2 - E_2 B_1 \rangle / \langle B_1^2 + B_2^2 \rangle$. Regardless of the values of V_1 and V_2, the electric field remaining in any frame that has its velocity component along the normal equal to this value of V_3, is directed purely along $\hat{\boldsymbol{n}}$, but is generally not zero outside the discontinuity layer. However, the two velocity components V_1 and V_2 can be determined in a separate step, as described by *Paschmann* [1985], to give zero electric field on the two sides of the discontinuity layer. After transformation to the frame of reference moving in this manner, only the intrinsic electric field within the layer remains, directed along $\hat{\boldsymbol{n}}$. The velocity V_3 replaces $\boldsymbol{V}_{\rm HT}$ as the estimate of the current sheet motion along the normal.

As pointed out to us by A. Vaivads [private communication, 2007], there is also an entirely different application of Eqn. 7.4, namely, to the determination of a proper frame velocity V, from electric field components, E_1 and E_2, measured in the spin plane of a spacecraft that lacks the ability to measure the spin-axis component, E_3. Eqn. 7.4 can be derived from the corresponding formula for regular HT analysis (Eqn. 7.2 above; see also Eqn. 9.12 in ISSI SR-001, with K_0 defined as the average of the matrix $\mathsf{K}_{\mu\nu}^{(m)}$ in Eqn. 9.11) by letting $\left\langle E_z' B_y \right\rangle = \left\langle E_z' B_x \right\rangle = 0$, where $\boldsymbol{E}' = \boldsymbol{E} + \boldsymbol{V} \times \boldsymbol{B}$ is the electric field in the co-moving frame. These two conditions are not exactly satisfied in the HT frame, obtained from Eqn. 7.2. In the latter frame, one has instead that $\left\langle E_z' B_y \right\rangle = \left\langle E_y' B_z \right\rangle$ and $\left\langle E_z' B_x \right\rangle = \left\langle E_x' B_z \right\rangle$. Therefore, the frame velocity derived from the spin-plane application of Eqn. 7.4, is not identical to the regular HT velocity, except if $\boldsymbol{E}' = 0$, as it is in a perfect HT frame, or if the four above correlations between components of $\boldsymbol{E}'$ and $\boldsymbol{B}$ happen to vanish. However, if a good HT frame does exist, the difference between $\boldsymbol{V}_{\rm HT}$ and the frame velocity $\boldsymbol{V}$ from Eqn. 7.4 is expected to be small. The procedure again fails if $\langle B_3^2 \rangle$ is close to zero.

7.3.2 Two-dimensional structures

Two-dimensional, time-independent but moving structures in a plasma have the property (from Faraday's law) that, in their proper frame, the electric field along the invariant direction is constant throughout the structure. This property can in some cases be used to determine both the direction and the motion of the invariant axis from single-spacecraft data. This possibility was mentioned in Chapter 9 of ISSI SR-001 but no convenient method for actually obtaining the orientation and motion was available at the time. A least-squares method for this purpose has now been developed [*Sonnerup and Hasegawa*, 2005] and, to a limited extent, tested with actual spacecraft data. In brief, the method again leads to an eigenvalue problem, in which the sought-after invariant axis, $\boldsymbol{k}$, is predicted as the eigenvector $\boldsymbol{k}_3$ corresponding to the smallest eigenvalue, λ_3, of the system

$$(\mathsf{M}_0 - \lambda \mathsf{I}) \cdot \boldsymbol{k} = 0 \tag{7.5}$$

where I is the identity matrix and the symmetric 3×3 matrix M_0 is defined by

$$\mathsf{M}_0 = -\mathsf{M}^{EB} \cdot \mathsf{M}^{-BB} \cdot \mathsf{M}^{BE} + \mathsf{M}^{EE} \tag{7.6}$$

Here the matrices M^{EB}, M^{BB}, M^{BE}, and M^{EE}, are co-variance matrices, e.g., $\mathsf{M}_{ij}^{EB} = \langle \delta E_i \delta B_j \rangle$, and M^{-BB} is the inverse of the magnetic co-variance matrix $\mathsf{M}_{ij}^{BB} = \langle \delta B_i \delta B_j \rangle$.

As before, the symbol δ denotes deviation from the average, e.g., $\delta B_i = B_i - \langle B_i \rangle$ and $\langle ... \rangle$ denotes the average over the data set used in the calculation. Assuming $\boldsymbol{k}$ to be normalised, $|\boldsymbol{k}|^2 = 1$, the velocity of motion of the invariant axis is given by

$$\boldsymbol{V}_0 = \boldsymbol{k} \times (\mathsf{M}^{-BB} \cdot \mathsf{M}^{BE} \cdot \boldsymbol{k}) \tag{7.7}$$

and the constant electric-field component along the invariant axis, evaluated in the system moving with velocity $\boldsymbol{V}_0$, is

$$E_0 = \langle \boldsymbol{E} \rangle \cdot \boldsymbol{k} + \langle \boldsymbol{B} \rangle \cdot (\boldsymbol{k} \times \boldsymbol{V}_0) \tag{7.8}$$

The method fails if M^{BB} is not invertible and if a perfect deHoffmann-Teller (HT) frame exists. In a perfect HT frame, the electric field is identically zero and therefore cannot contain any information about axis orientation. To date, applications of the method presented above are limited but indicate that the technique can work well for some flux transfer events at Earth's magnetopause [*Sonnerup and Hasegawa*, 2005; *Hasegawa et al.*, 2006]. For ordinary magnetopause traversals it seldom gives believable results, usually because of poor separation of the two smallest eigenvalues of M_0.

Various multi-spacecraft methods for finding axis orientation (and motion) have been developed [*Shi et al.*, 2005, 2006; *Xiao et al.*, 2004; *Zhou et al.*, 2006a, b] and applied to Cluster data (see also Chapter 2).

7.3.3 Three-dimensional structures.

Except for the special case where an acceptably good HT frame exists, there appears to be no obvious way to find the motion of a fully three-dimensional, time-independent structure from single-spacecraft data. However, if the Cluster spacecraft separation is sufficiently small compared to the size of the structure, one may use the gradient-based method developed by *Shi et al.* [2006] on the measured magnetic field. An alternate, as yet untested, approach is to use Cluster's curlometer capability (see Chapter 2) to search for a frame of reference moving at velocity $\boldsymbol{V}$ such that the object function

$$D(\boldsymbol{V}) = \left\langle |\nabla \times (\boldsymbol{E} + \boldsymbol{V} \times \boldsymbol{B})|^2 \right\rangle \tag{7.9}$$

obtained from Faraday's law, written in the co-moving frame where $\partial B/\partial t = 0$, is minimised. If a perfect proper frame exists, the object function will be exactly zero. The resulting set of linear equations for the components of $\boldsymbol{V}$ is lengthy and is not given here. As is the case for the gradient-based method [*Shi et al.*, 2006], the Faraday-based approach would be applicable, not only to three-dimensional structures, but to one- and two-dimensional ones as well.

7.4 Walén relation

As plasma flows across an ideal rotational discontinuity (RD), the components of the plasma velocity, $\boldsymbol{v}$, tangential to that layer change in response to the $\boldsymbol{j} \times \boldsymbol{B}_n$ force ($B_n = \boldsymbol{B} \cdot \hat{\boldsymbol{n}}$). In the spacecraft frame, this implies that

$$\Delta \boldsymbol{v} = \pm \Delta \boldsymbol{v}_A \tag{7.10}$$

where the symbol Δ refers to changes relative to some upstream state, for example, and $\boldsymbol{v}_A$ is the local Alfvén velocity, corrected for the effect of pressure anisotropy,

$$\boldsymbol{v}_A = \boldsymbol{B}[(1-\alpha)/\mu_0\rho]^{0.5} \tag{7.11}$$

with $\alpha = (p_\parallel - p_\perp)\mu_0/B^2$. Eqn. 7.10 is the so-called Walén relation expressed in the spacecraft frame.

In spite of the fact that the flow acceleration $\Delta\boldsymbol{v}$ is due to the $\boldsymbol{j} \times \boldsymbol{B}_n$ force, the Walén relation does not contain B_n. This is because for an RD, as for any planar Alfvén wave, v_n is proportional to B_n. Thus the smaller B_n, the smaller the inflow velocity, and thus the less mass to accelerate. Of course, this independence of B_n means that a successful Walén test does not say anything about the reconnection rate, which is proportional to B_n. On the other hand, it does imply that B_n was non-zero because otherwise the $\boldsymbol{j} \times \boldsymbol{B}_n$ force would be zero, i.e., there would be no tangential acceleration of the plasma. This is no small feat because the expected B_n is so small, compared with the total B, that to experimentally determine that its value, $\boldsymbol{B} \cdot \hat{\boldsymbol{n}}$, is significantly different from zero requires a very nearly one-dimensional structure and knowledge of the direction, $\hat{\boldsymbol{n}}$, normal to it with an accuracy rarely available (see Chapter 1).

The positive (negative) sign in the Walén relation applies if the normal components of the magnetic field and plasma velocity, B_n and v_n have the same (opposite) signs.

When formulated as a jump relation, the test requires selection of the times between which the jumps in $\boldsymbol{v}$ and $\boldsymbol{v}_A$ are to be compared. This problem is partially overcome if, after selection of an upstream reference state, one produces a time-series plot, where the velocities predicted by the Walén relation are overplotted on the observed velocities [e.g., *Phan et al.*, 2004]. Since there is the issue of the a-priory unknown sign in the Walén relation, one can overplot the predicted velocities, once with the $+$ sign and a second time with the $-$ sign. Such time-series plots have the advantage of showing, for example, whether the relation is fulfilled during only part of the discontinuity crossing.

As discussed in Section 9.3.3 of ISSI SR-001, the HT frame provides a convenient frame for testing the Walén relation. In the HT frame, the Walén relation has a much simpler formulation. As the plasma velocity in this frame becomes $\boldsymbol{v}' = (\boldsymbol{v} - \boldsymbol{V}_{\mathrm{HT}})$, the Walén relation reduces to

$$\boldsymbol{v}' = \pm\boldsymbol{v}_A \tag{7.12}$$

In the HT frame, testing of the Walén relation thus consists of a component-by-component scatter plot of the plasma velocities and the Alfvén velocities measured across the discontinuity. There is no need for selecting reference values for $\boldsymbol{v}$ and $\boldsymbol{v}_A$. When applied to an ideal RD, the scatter plot should show a correlation coefficient and a slope of ± 1. A scatter plot destroys the time-order of the measurements. If one wants to preserve this order, one can alternatively overplot $(\boldsymbol{v} - \boldsymbol{V}_{\mathrm{HT}})$ and $\pm\boldsymbol{v}_A$.

If the Walén test is used on a slow-mode shock, the flow speed and Alfvén speed are no longer equal: the upstream Alfvén number is larger than the downstream value and the former is <1, except for a switch-off shock, for which it is equal to 1. On the other hand, an intermediate shock has upstream Alfvén number > 1 while its downstream Alfvén number remains < 1. If the test is used on a reconnection configuration, consisting of an exhaust jet sandwiched between two slow-mode shocks, such as might occur in the geomagnetic tail, the scatter plot should show two branches, one with positive and one with negative correlation. This behaviour would unambiguously indicate plasma inflow from both sides

of the wedge. This result is more convincing than a direct determination of the normal flow by projection of the flow vectors in the HT frame onto the normal vector. The direction of the latter would have to be obtained by use of one of the methods described in Chapter 1 and such normals have notoriously large uncertainties.

A final remark is that the existence of an HT frame is a necessary but not a sufficient condition for the identification of a discontinuity as a one-dimensional RD. This statement holds even when data points within the layer are included in the HT analysis. For example, one can imagine a perfect tangential discontinuity (TD) where no intrinsic electric field along the normal direction is present within the discontinuity. Such a TD would possess a perfect HT frame but would not be an RD.

7.5 Recent applications

Use of the HT frame has become widespread, either as the frame in which moving structures are conveniently discussed [*Hasegawa et al.*, 2004, 2005, 2006; *Sonnerup et al.*, 2004; *Sonnerup and Hasegawa*, 2005; *Nykyri et al.*, 2006], or to estimate the speed of a discontinuity as the normal component of the transformation velocity, $\boldsymbol{V}_{\mathrm{HT}} \cdot \hat{\boldsymbol{n}}$ [*Haaland et al.*, 2004; *Khotyaintsev et al.*, 2004; *Sonnerup et al.*, 2006, 2007; *Retinò et al.*, 2006], or as the convenient frame in which to test the Walén-relation [*Puhl-Quinn and Scudder*, 2000; *Eriksson et al.*, 2004a, b; *Phan et al.*, 2004; *Paschmann et al.*, 2005; *Gosling et al.*, 2005; *Nykyri et al.*, 2006].

In all the cited applications, the HT frame determination was based on the measured ion bulk velocities and magnetic fields, with the exception of *Khotyaintsev et al.* [2004], where the measured electric field was used directly. Electric field data have been used only rarely because the Cluster electric field measurements are only two-dimensional. To our knowledge, the only paper where electron bulk velocities were used is *Puhl-Quinn and Scudder* [2000].

7.6 Summary

In this chapter, the topics of the deHoffmann-Teller (HT) frame and the Walén relation from Chapter 9 of ISSI SR-001 have been revisited. In particular, the HT frame is now viewed as a special case of the more general concept of a 'proper frame', i.e., a frame co-moving with a plasma/field structure, in which frame the structure is assumed to be approximately time independent but may posses an intrinsic remnant electrostatic field distribution. The structure studied may be one-, two-, or three-dimensional and the HT frame corresponds to the case where the intrinsic electric field is zero, or negligibly small. In using these tools, it is important to keep in mind some of the following pitfalls and unexplained features.

The velocity of a one-dimensional discontinuity along the normal direction is, in principle, given by $\boldsymbol{V}_{\mathrm{HT}} \cdot \hat{\boldsymbol{n}}$. But in many applications, e.g., at the magnetopause, $\boldsymbol{V}_{\mathrm{HT}}$ is a large velocity that is nearly perpendicular to the normal vector $\hat{\boldsymbol{n}}$, the result being that the usually much smaller normal velocity component is very sensitive to errors both in frame velocity and in normal direction. These errors are not only of a statistical nature. They may have large contributions from geometrical substructures and from a lack of time stationar-

ity. Limited insight into these uncertainties can be gained by repeated determinations of $\boldsymbol{V}_{\mathrm{HT}}$ and $\hat{\boldsymbol{n}}$, using nested data segments. For two-dimensional structures where a reliable invariant direction has been found, a more reliable estimate of the normal motion may be $\boldsymbol{V}_{\mathrm{HT}\perp} \cdot \hat{\boldsymbol{n}}$, where $\boldsymbol{V}_{\mathrm{HT}\perp}$ is the portion of the HT velocity perpendicular to the invariant axis.

One persistent problem with the Walén test, encountered in its application at the magnetopause, is that plasma mass densities, ρ and pressure anisotropies, α, measured at, and near, the magnetopause, do not follow the MHD-based theoretical prediction for a rotational discontinuity, namely that $\rho(1-\alpha)$ should remain constant within the layer. The reason for this discrepancy is not understood. Inclusion of data from magnetospheric regions, in which the plasma has not yet interacted with the magnetopause, could be a contributing factor. In such regions the plasma velocity is small and the Alfvén speed large. It has been found that the quality of the Walén test usually improves, if, by use of the above MHD-based prediction, one replaces the measured plasma density within the layer by $\rho = \rho_1(1-\alpha_1)/(1-\alpha)$, where the subscript one denotes the upstream condition [*Paschmann et al.*, 1986; *Phan et al.*, 2004; *Retinò et al.*, 2005].

In applications to the magnetopause [e.g., *Paschmann et al.*, 2005] and also to solar-wind discontinuities [e.g., *Neugebauer*, 2006], the directional changes of the plasma velocity are often found to be in good agreement with the corresponding changes of the Alfvén velocity, while the magnitude of the velocity changes are usually considerably smaller than those of the Alfvén speed. The agreement of the directional changes is consistent with the presence of magnetic connection across the layer; the disagreement of the magnitude changes indicates that some unknown contributions to the tangential stress balance are present but not accounted for.

There are several possible explanations for the noted discrepancies in the Walén test. For example, cold particle populations or heavier ions may have been missed in the measurements so that the actual Alfvén speed is smaller than that used in the test. The presence of gradients tangential to the discontinuity surface of plasma pressure and guide field may also change the tangential stress balance so that the purely one-dimensional structure assumed in the Walén test becomes invalid. If the reconnection jets are confined to a narrow longitude segment, i.e., if the X-line is short, the plasma in the jets may be magnetically coupled to adjoining regions where no reconnection occurs. The presence of such three-dimensional effects cannot be excluded. Another possibility is that, in some crossings, the Walén relation may be rendered invalid in the interior of the magnetopause by non-gyrotropic plasma behaviour such as the presence of some form of gyro-viscosity [e.g., *Hau and Sonnerup*, 1991].

Note that incident, transmitted, reflected, and trapped particle populations, all contribute to the tangential stress balance and therefore should be included in the Walén test, their effects being accounted for via their contribution to both the total density and the pressure anisotropy factor. It has been reported by *Retinò et al.* [2005] that the quality of the Walén test can be improved significantly by removing a beam-like, counter-streaming, secondary particle population that is sometimes seen within (but not outside) the magnetopause current layer, in addition to the transmitted beam. The reasons for the presence of this secondary beam, or for not including it in the tangential stress balance, are not understood at present.

Software implementation

Software for the determination of the HT frame and for testing the Walén relation is included in QSAS, available at http://www.sp.ph.ic.ac.uk/csc-web/QSAS/.

Acknowledgements

The work by B.U.Ö.S. was supported by the National Aeronautics and Space Administration under Cluster Theory Guest Investigator Grant NNG-05-GG26G to Dartmouth College.

Bibliography

de Hoffmann, F. and Teller, E., 1950, Magneto-Hydrodynamic Shocks, *Phys. Rev.*, **80**, 692–703, doi:10.1103/PhysRev.80.692.

Eriksson, S., Elkington, S. R., Phan, T. D., Petrinec, S. M., Rème, H., Dunlop, M. W., Wiltberger, M., Balogh, A., Ergun, R. E., and André, M., 2004a, Global control of merging by the interplanetary magnetic field: Cluster observations of dawnside flank magnetopause reconnection, *J. Geophys. Res.*, **109**, A12203, doi:10.1029/2003JA010346.

Eriksson, S., Øieroset, M., Baker, D. N., Mouikis, C., Vaivads, A., Dunlop, M. W., Rème, H., Ergun, R. E., and Balogh, A., 2004b, Walén and slow-mode shock analyses in the near-Earth magnetotail in connection with a substorm onset on 27 August 2001, *J. Geophys. Res.*, **109**, A10212, doi:10.1029/2004JA010534.

Gosling, J. T., Skoug, R. M., McComas, D. J., and Smith, C. W., 2005, Direct evidence for magnetic reconnection in the solar wind near 1 AU, *J. Geophys. Res.*, **110**, A01107, doi:10.1029/2004JA010809.

Haaland, S., Sonnerup, B., Dunlop, M., Balogh, A., Georgescu, E., Hasegawa, H., Klecker, B., Paschmann, G., Puhl-Quinn, P., Rème, H., Vaith, H., and Vaivads, A., 2004, Four-spacecraft determination of magnetopause orientation, motion and thickness: comparison with results from single-spacecraft methods, *Ann. Geophys.*, **22**, 1347–1365, http://www.ann-geophys.net/22/1347/2004/.

Hasegawa, H., Sonnerup, B., Dunlop, M., Balogh, A., Haaland, S., Klecker, B., Paschmann, G., Lavraud, B., Dandouras, I., and Rème, H., 2004, Reconstruction of two-dimensional magnetopause structures from Cluster observations: verification of method, *Ann. Geophys.*, **22**, 1251–1266, http://www.ann-geophys.net/22/1251/2004/.

Hasegawa, H., Sonnerup, B. U. Ö., Klecker, B., Paschmann, G., Dunlop, M. W., and Rème, H., 2005, Optimal reconstruction of magnetopause structures from Cluster data, *Ann. Geophys.*, **23**, 973–982, http://www.ann-geophys.net/23/973/2005/.

Hasegawa, H., Sonnerup, B. U. Ö., Owen, C. J., Klecker, B., Paschmann, G., Balogh, A., and Rème, H., 2006, The structure of flux transfer events recovered from Cluster data, *Ann. Geophys.*, **24**, 603–618, http://www.ann-geophys.net/24/603/2006/.

Hau, L.-N. and Sonnerup, B. U. O., 1991, Self-consistent gyroviscous fluid model of rotational discontinuities, *J. Geophys. Res.*, **96**, 15 767.

Khotyaintsev, Y., Buchert, S., Stasiewicz, K., Vaivads, A., Savin, S., Papitashvili, V. O., Farrugia, C. J., Popielawska, B., and Tung, Y.-K., 2004, Transient reconnection in the cusp during strongly negative IMF By, *J. Geophys. Res.*, **109**, A04204, doi:10.1029/2003JA009908.

Khrabrov, A. V. and Sonnerup, B. U. Ö., 1998, DeHoffmann-Teller Analysis, in *Analysis Methods for Multi-Spacecraft Data*, edited by G. Paschmann and P. W. Daly, no. SR-001 in ISSI Scientific Reports, chap. 9, pp. 221–248, ESA Publ. Div., Noordwijk, Netherlands.

Neugebauer, M., 2006, Comment on the abundances of rotational and tangential discontinuities in the solar wind, *J. Geophys. Res.*, **111**, A04103, doi:10.1029/2005JA011497.

Nykyri, K., Otto, A., Lavraud, B., Mouikis, C., Kistler, L. M., Balogh, A., and Rème, H., 2006, Cluster observations of reconnection due to the Kelvin-Helmholtz instability at the dawnside magnetospheric flank, *Ann. Geophys.*, **24**, 2619–2643, http://www.ann-geophys.net/24/2619/2006/.

Paschmann, G., 1985, Comment on 'Electric field measurements at the magnetopause. I—Observation of large convective velocities at rotational magnetopause discontinuities' by T. L. Aggson, P. J. Gambardella, and N. C. Maynard, *J. Geophys. Res.*, **90**, 7629.

Paschmann, G., Baumjohann, W., Sckopke, N., Papamastorakis, I., and Carlson, C. W., 1986, The magnetopause for large magnetic shear—AMPTE/IRM observations, *J. Geophys. Res.*, **91**, 11 099–11 115.

Paschmann, G., Haaland, S., Sonnerup, B. U. Ö., Hasegawa, H., Georgescu, E., Klecker, B., Phan, T. D., Rème, H., and Vaivads, A., 2005, Characteristics of the near-tail dawn magnetopause and boundary layer, *Ann. Geophys.*, **23**, 1481–1497, http://www.ann-geophys.net/23/1481/2005/.

Phan, T., Dunlop, M., Paschmann, G., Klecker, B., Bosqued, J., Rème, H., Balogh, A., Twitty, C., Mozer, F., Carlson, C., Mouikis, C., and Kistler, L., 2004, Cluster observations of continuous reconnection at the magnetopause under steady interplanetary magnetic field conditions, *Ann. Geophys.*, **22**, 2355–2367, http://www.ann-geophys.net/22/2355/2004/.

Puhl-Quinn, P. A. and Scudder, J. D., 2000, Systematics of ion Walén analysis of rotational discontinuities using E/Z measurements, *J. Geophys. Res.*, **105**, 7617–7628, doi:10.1029/1999JA000314.

Retinò, A., Bavassano Cattaneo, M. B., Marcucci, M. F., Vaivads, A., André, M., Khotyaintsev, Y., Phan, T., Pallocchia, G., Rème, H., Möbius, E., Klecker, B., Carlson, C. W., McCarthy, M., Korth, A., Lundin, R., and Balogh, A., 2005, Cluster multispacecraft observations at the high-latitude duskside magnetopause: implications for continuous and component magnetic reconnection, *Ann. Geophys.*, **23**, 461–473, http://www.ann-geophys.net/23/461/2005/.

Retinò, A., Vaivads, A., André, M., Sahraoui, F., Khotyaintsev, Y., Pickett, J. S., Bavassano Cattaneo, M. B., Marcucci, M. F., Morooka, M., Owen, C. J., Buchert, S. C., and Cornilleau-Wehrlin, N., 2006, Structure of the separatrix region close to a magnetic reconnection X-line: Cluster observations, *Geophys. Res. Lett.*, **33**, L06101, doi:10.1029/2005GL024650.

Schwartz, S. J., 1998, Shock and Discontinuity Normals, Mach Numbers, and Related Parameters, in *Analysis Methods for Multi-Spacecraft Data*, edited by G. Paschmann and P. W. Daly, no. SR-001 in ISSI Scientific Reports, chap. 10, pp. 249–270, ESA Publ. Div., Noordwijk, Netherlands.

Shi, Q. Q., Shen, C., Pu, Z. Y., Dunlop, M. W., Zong, Q.-G., Zhang, H., Xiao, C. J., Liu, Z. X., and Balogh, A., 2005, Dimensional analysis of observed structures using multipoint magnetic field measurements: Application to Cluster, *Geophys. Res. Lett.*, **32**, L012105, doi:10.1029/2005GL022454.

Shi, Q. Q., Shen, C., Dunlop, M. W., Pu, Z. Y., Zong, Q.-G., Liu, Z. X., Lucek, E., and Balogh, A., 2006, Motion of observed structures calculated from multi-point magnetic field measurements: Application to Cluster, *Geophys. Res. Lett.*, **33**, L08109, doi:10.1029/2005GL025073.

Sonnerup, B. U. Ö. and Hasegawa, H., 2005, Orientation and motion of two-dimensional structures in a space plasma, *J. Geophys. Res.*, **110**, A06208, doi:10.1029/2004JA010853.

Sonnerup, B. U. O., Papamastorakis, I., Paschmann, G., and Luehr, H., 1987, Magnetopause properties from AMPTE/IRM observations of the convection electric field—Method development, *J. Geophys. Res.*, **92**, 12 137–12 159.

Sonnerup, B. U. Ö., Hasegawa, H., and Paschmann, G., 2004, Anatomy of a flux transfer event seen by Cluster, *Geophys. Res. Lett.*, **31**, L11803, doi:10.1029/2004GL020134.

Sonnerup, B. U. Ö., Haaland, S., Paschmann, G., Dunlop, M. W., Rème, H., and Balogh, A., 2006, Orientation and motion of a plasma discontinuity from single-spacecraft measurements: Generic residue analysis of Cluster data, *J. Geophys. Res.*, **111**, A05203, doi:10.1029/2005JA011538.

Sonnerup, B. U. Ö., Haaland, S., Paschmann, G., Dunlop, M. W., Rème, H., and Balogh, A., 2007, Correction to "Orientation and motion of a plasma discontinuity from single-spacecraft measurements: Generic residue analysis of Cluster data", *J. Geophys. Res.*, **112**, A04201, doi:10.1029/2007JA012288.

Xiao, C. J., Pu, Z. Y., Ma, Z. W., Fu, S. Y., Huang, Z. Y., and Zong, Q. G., 2004, Inferring of flux rope orientation with the minimum variance analysis technique, *J. Geophys. Res.*, **109**, A011218, doi:10.1029/2004JA010594.

Zhou, X.-Z., Zong, Q.-G., Pu, Z. Y., Fritz, T. A., Dunlop, M. W., Shi, Q. Q., Wang, J., and Wei, Y., 2006a, Multiple Triangulation Analysis: another approach to determine the orientation of magnetic flux ropes, *Ann. Geophys.*, **24**, 1759–1765, http://www.ann-geophys.net/24/1759/2006/.

Zhou, X.-Z., Zong, Q.-G., Wang, J., Pu, Z. Y., Zhang, X. G., Shi, Q. Q., and Cao, J. B., 2006b, Multiple triangulation analysis: application to determine the velocity of 2-D structures, *Ann. Geophys.*, **24**, 3173–3177, http://www.ann-geophys.net/24/3173/2006/.

— 8 —

Plasma Kinetics

PATRICK W. DALY
Max-Planck-Institut für Sonnensystemforschung
Katlenburg-Lindau, Germany

STEVEN J. SCHWARTZ AND BERTRAND LEFEBVRE
Blackett Laboratory, Imperial College London
London, United Kingdom

8.1 Concepts of plasma kinetics

In Chapter 7 of ISSI SR-001, *Schwartz et al.* [1998] explain the basic ideas of analysis by means of plasma kinetics: Liouville mapping and finite gyroradius effects.

Liouville mapping can be used to relate features of distribution functions such as heating, anisotropies or beams, to the field variations. It is based on the conservation of phase space density along particle trajectories in collisionless plasmas, and therefore requires that particle trajectories (or at least their initial and final states) can be accurately approximated. This requirement generally relies on invariants of the particle motion such as the energy and adiabatic invariants and some knowledge of the electromagnetic fields along the trajectories.

The *large gyroradius* of energetic ions has the consequence that ions detected at different directions are actually probing conditions at considerable distances around the spacecraft. Density gradients then appear as gyrophase anisotropies in the angular distributions. This effect was first employed by *Kaufmann and Konradi* [1973] to probe the magnetopause. Section 7.5 of *Schwartz et al.* [1998] explain how it can be used to remotely sense sharp boundaries in ion densities. In particular, see Figures 7.4 and 7.6 in that chapter for a graphical demonstration.

For a historical perspective on these topics, see also the classic paper by *Northrop and Teller* [1960] on the motion of charged particles in the Earth's magnetic field. In addition, *Whipple et al.* [1998] present an alternative framework that builds on the underlying concepts, while *Whipple et al.* [1986] describe extensions to the classic adiabatic theory that apply even in regions of strong gradients.

8.2 Applications of Liouville mapping

Several studies have exploited the multi-spacecraft configuration of Cluster together with Liouville mapping techniques to good effect. Some of these are summarised here. See the full papers for more details.

8.2.1 Liouville mapping for the determination of the electrostatic potential within the bow shock

Liouville mapping based on conservation of energy in the appropriate (deHoffmann-Teller) reference frame (see Chapter 9 of ISSI SR-001 and Chapter 7 of the present volume) and of the first adiabatic invariant may be employed at quasi-perpendicular shocks to predict several important characteristics of the downstream electron velocity distributions from those of upstream one. *Lefebvre et al.* [2007] have applied this technique to shock crossings by Cluster, comparing the predicted electron distribution to that observed by the PEACE instrument at various pitch angles. On one such crossing, the Cluster configuration allowed the upstream and downstream distributions to be monitored simultaneously at locations that were relatively well connected magnetically, minimising the possible problems associated with temporal and spatial variations during the crossing. The predictions were generally found to match the observations, with some discrepancies that imply the non-strict conservation of energy and magnetic moment.

Based on this agreement at zero order, the technique was used to estimate the electric potential across the shock by finding the potential that yields the best fit between the predicted and observed distributions. The cross-shock potential is an important quantity, controlling in great part the ion reflection and some particle acceleration processes, but it is very difficult to estimate from direct electric field measurements. The deHoffmann-Teller potential derived from this method was found to follow a profile similar to that of the magnetic field. However, there are some indications that the potential could exhibit slightly steeper gradients in the shock ramp, thereby partly invalidating the assumptions underlying the mapping concept. Instruments with higher time resolution may be needed to settle this question.

This is illustrated in Figure 8.1, which shows comparisons between cuts of the measured and mapped distributions at different pitch-angles, and in Figure 8.2 where electron guiding-centre trajectories based on conservation laws are compared with the measured phase-space density.

8.2.2 Liouville mapping downstream of the bow shock: the source of electron temperature anisotropy

Electron velocity distributions in the Earth's magnetosheath exhibit a number of non-equilibrium characteristics, including a flat-topped shape at thermal energies and anisotropies relative to the magnetic field, with $T_{\perp e} > T_{\parallel e}$. These features are related to processes at the bow shock and within the magnetosheath, but the process(es) responsible for the anisotropy are unknown. *Masood and Schwartz* [2008] used Cluster's multi-spacecraft capabilities to compare simultaneous electron distributions at different distances behind the bow shock. Such studies remove the temporal ambiguities introduced by single-spacecraft analyses. That comparison showed that the electron velocity space distributions just behind the bow shock are nearly isotropic with a slight $T_{\parallel e} > T_{\perp e}$ anisotropy whereas deeper into the magnetosheath the electrons exhibit a significant $T_{\perp e} > T_{\parallel e}$ anisotropy.

They found a clear decrease of suprathermal electrons at 0° and 180° pitch angles, suggesting that this population suffers losses, e.g., into the upstream region, related to the mobility of electrons in the global configuration provided by the magnetosheath. Additionally, the 90° pitch angle suprathermal electron population increased in width with distance

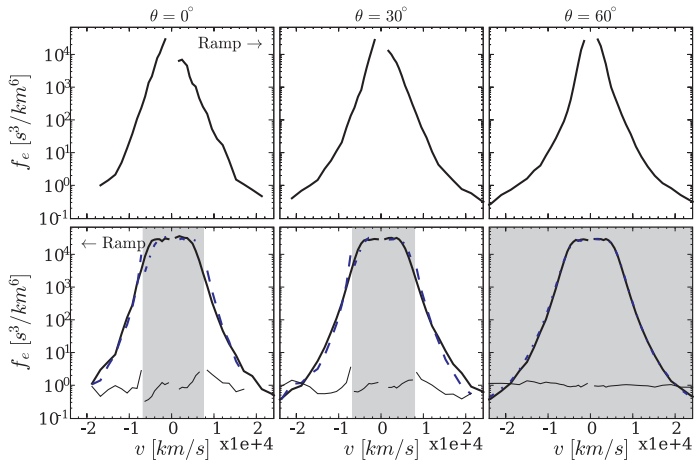

Figure 8.1: Cuts at 0, 30 and 60° pitch-angles of the electron velocity distributions upstream (top) and downstream (bottom) of a quasi-perpendicular shock on March 19, 2005, measured by the PEACE instrument on Cluster. Cuts of the downstream distribution (solid line) are compared with the Liouville-mapped upstream distributions simultaneously measured by an upstream spacecraft (dashed line). The area shaded in grey corresponds to electrons which cannot cross the shock, assuming conservation of their energy and magnetic moment in the deHoffmann-Teller (HT) frame. This part of the distribution is compared with the reflected distribution, mirrored around $v = 0$ in the HT frame (dotted line). The thin line at the bottom of the plot is the ratio of the mapped to observed distributions, showing that the most notable discrepancies occur at low energies near the separatrix between passing and non-passing electrons. Adapted from *Lefebvre et al.* [2007].

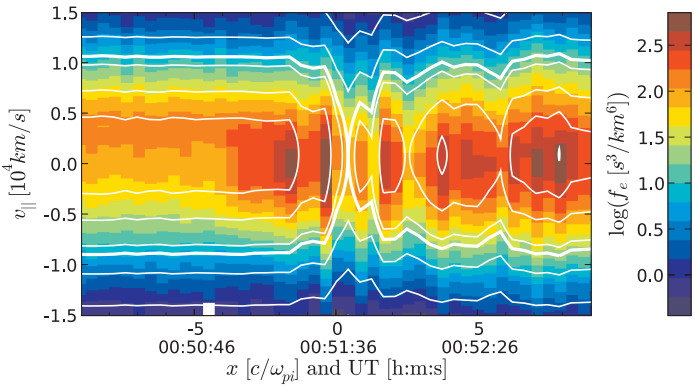

Figure 8.2: Electron phase-space density (colour) for a given magnetic moment ($\mu = 5T_{e\perp u}/B_u$). The white lines correspond to electron guiding-centre trajectories derived from conservation of energy and magnetic moment in the observed magnetic field and estimated electric potential. If these hypotheses were perfectly valid for all electrons, each of these trajectories should follow contours of the distribution. Adapted from *Lefebvre et al.* [2007].

into the magnetosheath.

Masood and Schwartz [2008] then applied the Liouville mapping techniques based on magnetic moment and energy constants of particle motion to determine the extent to which the systematic increase in perpendicular anisotropy might be related to adiabatic evolution. The mapping clearly shows that other processes must be operating in the magnetosheath to inflate the perpendicular pitch angles, and that the loss of field-aligned suprathermals is very rapid. The study is a good example of how multipoint measurements can be used to remove temporal variability, and of how the details of the particle distributions can be used in conjunction with Liouville's Theorem to make strong conclusions about the physical processes that are, and are not, occurring.

8.2.3 Application of Liouville concepts to flux transfer events

Another application of Liouville's Theorem in its widest sense (mapping of plasma distributions between different regions) is in the analysis of flux transfer events (FTEs). These are localised flux tubes penetrating the magnetopause, allowing magnetosheath and magnetospheric plasmas to mix and disperse. One important aspect of such studies is the 'connectivity' of the event, meaning whether the flux tube joins to the northern or southern hemisphere. Generally the location above or below the magnetic equator indicates this, but there are exceptions, especially if the connection point has crossed the equator. A more reliable determination is given by the pitch angle of the energetic ions as they escape from out of the magnetosphere: northerly connected events will have ions moving predominantly anti-parallel to the magnetic field.

In a recent study of FTE motion [*Fear et al.*, 2007], RAPID ion data have been used to make just such an unambiguous determination of magnetic connectivity. In this case, where the field is oriented generally north-south, the missing RAPID data at 90° (see below) are unimportant, since it is the 0° and 180° directions that are of interest.

8.3 Applications of remote sensing of boundaries

A number of papers have exploited the remote sensing technique to study various plasma boundaries. Again, see the full texts for more details.

8.3.1 Remote sensing with ions at foreshock cavities

Foreshock cavities are brief (less than a minute) depressions in the interplanetary magnetic field, accompanied by enhanced fluxes of energetic ions seen upstream of the Earth's bow shock [*Sibeck et al.*, 2004, and references therein]. Foreshock cavities, if sufficiently common, may play significant roles in triggering magnetospheric events. Such cavities are believed to be formed when an isolated collection of interplanetary magnetic field lines connect to quasi-parallel regions of the Earth's bow shock, allowing shock-associated energetic ions to flow upstream and excavate a local cavity. Observations by the Cluster spacecraft reported by *Schwartz et al.* [2006] show precisely this configuration. The suprathermal ions can be seen just outside the edges of the cavity within a restricted range of gyrophases, consistent with their gyromotion tangential to the layer containing the cavity.

8.3.2 Remote sensing of the magnetopause

The method of using gyrophase asymmetries in the ion distributions to determine the orientation and distance from an absorbing boundary has also been applied to monitoring the motion of the dayside magnetopause. *Oksavik et al.* [2002] employed this technique to the energetic ions from the RAPID experiment on three Cluster spacecraft (the unit on the 4th spacecraft was not operational at the time) very early in the mission, on January 14, 2001, during an outbound pass through the magnetopause. The width of the 'hole' in the gyrophase distribution yields the distance from the spacecraft to the absorbing boundary (magnetopause) from 0 to 2 gyroradii while the centre of the hole is 90° to the boundary normal. For 60 keV protons in a field of 15 nT the gyroradius is 2400 km. In spite of the small spacecraft separations of 500–600 km, considerable differences were observed among them. The magnetopause was seen to approach and retreat, with the different spacecraft measuring different distances, consistent with the expected magnetopause orientation and geometry of the spacecraft constellation. Magnetopause velocities of up to 30 km/s were recorded.

A more detailed analysis of this event has been carried out by *Zong et al.* [2004], who use the derived distances to the absorbing boundary to measure the density gradients of magnetosheath plasma and of energetic particle flux inside the magnetopause. They establish that the plasma falls off exponentially with distance, with an e-folding length of ∼1000 km. The energetic ion flux increases linearly over 2 gyroradii; however, electron fluxes are uniform.

It is unfortunate that this very promising method for remote sensing of particle boundaries will find very limited application with the RAPID data on Cluster since the ion detector that looks into the ecliptic plane deteriorated within a few weeks of operations on all 4 spacecraft. This failure is likely due to photo-electrons swamping one of the multichannel plates used for the time-of-flight determination. But it is precisely this detector that sees 90° particles when the magnetic field is oriented north-south. The January 14, 2001 event can be studied because at this time all 3 detectors were still functioning. Remote sensing of the plasma sheet in the geomagnetic tail remains a possibility, however.

Software implementation

The Liouville mapping of electron measurements from Cluster is implemented in QPEACE software, available at http://www.sp.ph.ic.ac.uk/csc-web/QPEACE/.

Acknowledgements

The work of B.L. and S.J.S. was funded by a grant from the Science and Technology Funding Council.

Bibliography

Fear, R. C., Milan, S. E., Fazakerley, A. N., Owen, C. J., Asikainen, T., Taylor, M. G. G. T., Lucek, E. A., Rème, H., Dandouras, I., and Daly, P. W., 2007, Motion of flux transfer events: a test of the Cooling model, *Ann. Geophys.*, **25**, 1669–1690, http://www.ann-geophys.net/25/1669/2007/.

Kaufmann, R. L. and Konradi, A., 1973, Speed and Thickness of the Magnetopause, *J. Geophys. Res.*, **78**, 6549–6568.

Lefebvre, B., Schwartz, S. J., Fazakerley, A. N., and Décréau, P., 2007, Electron dynamics and cross-shock potential at the quasi-perpendicular Earth's bow shock, *J. Geophys. Res.*, **112**, A09212, doi:10.1029/2007JA012277.

Masood, W. and Schwartz, S. J., 2008, Observations of the development of electron temperature anisotropies in the Earth's magnetosheath, *J. Geophys. Res.*, doi:10.1029/2007JA012715, in press.

Northrop, T. G. and Teller, E., 1960, Stability of the Adiabatic Motion of Charged Particles in the Earth's Field, *Phys. Rev.*, **117**, 215.

Oksavik, K., Fritz, T. A., Zong, Q.-G., Søraas, F., and Wilken, B., 2002, Three-dimensional energetic ion sounding of the magnetopause using Cluster/RAPID, *Geophys. Res. Lett.*, **29**, 1347, doi:10.1029/2001GL014265.

Schwartz, S. J., Daly, P. W., and Fazakerley, A. N., 1998, Multi-Spacecraft Analysis of Plasma Kinetics, in *Analysis Methods for Multi-Spacecraft Data*, edited by G. Paschmann and P. W. Daly, no. SR-001 in ISSI Scientific Reports, chap. 7, pp. 159–183, ESA Publ. Div., Noordwijk, Netherlands.

Schwartz, S. J., Sibeck, D., Wilber, M., Meziane, K., and Horbury, T. S., 2006, Kinetic aspects of foreshock cavities, *Geophys. Res. Lett.*, **33**, L12103, doi:10.1029/2005GL025612.

Sibeck, D., Kudela, K., Mukai, T., Nemecek, Z., and Safrankova, J., 2004, Radial dependence of foreshock cavities: a case study, *Ann. Geophys.*, **22**, 4143–4151, http://www.ann-geophys.net/22/4143/2004/.

Whipple, E. C., Northrop, T. G., and Birmingham, T. J., 1986, Adiabatic theory in regions of strong field gradients, *J. Geophys. Res.*, **91**, 4149–4156.

Whipple, E. C., Halekas, J. S., Scudder, J. D., Paterson, W. R., Frank, L. A., Sheldon, R. B., Maynard, N. C., Weimer, D. R., Russell, C. T., Tsuruda, K., Hayakawa, H., and Yamamoto, T., 1998, Identification of magnetospheric particles that travel between spacecraft and their use to help obtain magnetospheric potential distributions, *J. Geophys. Res.*, **103**, 93–102, doi:10.1029/97JA02195.

Zong, Q.-G., Fritz, T. A., Spence, H., Oksavik, K., Pu, Z.-Y., Korth, A., and Daly, P. W., 2004, Energetic particle sounding of the magnetopause: A contribution by Cluster/RAPID, *J. Geophys. Res.*, **109**, A04207, doi:10.1029/2003JA009929.

— 9 —

Grad-Shafranov and MHD Reconstructions

BENGT U. Ö. SONNERUP AND WAI-LEONG TEH
Thayer School of Engineering, Dartmouth College
Hanover, New Hampshire, USA

HIROSHI HASEGAWA
Institute of Space and Astronautical Science, JAXA
Sagamihara, Kanagawa, Japan

Since the publication of the multi-spacecraft data analysis book ISSI SR-001, new methods have been developed that allow field and plasma structures traversed by one or more spacecraft to be reconstructed in a region surrounding the spacecraft path from the measured data. Maps of field and plasma properties are created with the aid of various versions of the MHD equations, under the assumption that the structures can be treated as two-dimensional ($\partial/\partial z \simeq 0$), and as approximately time-independent in their proper (i.e., co-moving) frame of reference. Reconstruction of this type is not to be confused with numerical simulation. The former generates a time-stationary set of maps, the latter a description of the time evolution of a structure from some given initial state. In this chapter, we describe briefly four different reconstruction methods.

9.1 Magneto-hydrostatic structures

The first attempt to recover two-dimensional (2-D), time-independent magnetic-field structures from data taken by a single spacecraft as it traverses the structures was made by *Sonnerup and Guo* [1996]. Their approach was to integrate, as a spatial initial-value problem, the classical Grad-Shafranov (GS) equation governing 2-D magneto-hydrostatic structures in a plasma. This approach was brought to a useful form and applied to AMPTE-IRM observations of the dayside magnetopause by *Hau and Sonnerup* [1999]. It has now been successfully applied to a number of events at the magnetopause, in the geomagnetic tail, and in the solar wind (for a set of relevant references, see *Sonnerup et al.* [2006] and, additionally, *Hasegawa et al.* [2007b, a]; *Zhang et al.* [2007]; *De Keyser et al.* [2005]). For Cluster applications, it has also been modified to allow for the ingestion into the analysis of data from more than one spacecraft. A brief description of the method follows.

9.1.1 Integration procedure

Since the structures to be reconstructed usually move past the spacecraft at substantial speed, the first step is to find the proper frame, in which they appear approximately time-independent. To date, the deHoffmann-Teller (HT) frame (see Chapter 9 of ISSI SR-001 and also Chapter 7 of the present volume) has been used as the proper frame. In

cases where this frame is poorly determined, the method described in Section 7.3.2, which also provides the invariant (z) axis, may be tried, although this method is not always successful. Time delays between the passage of a structure past two or more observing spacecraft, as well as other multi-spacecraft methods, can in favourable circumstances also be used (see Section 9.1.2). In the proper frame, the spacecraft path through the structure, projected onto the reconstruction (xy) plane, i.e., the plane perpendicular to the invariant axis, becomes the x-axis. By use of the x-component of the frame velocity, the time series of measured magnetic field and other quantities can then be converted to spatial distributions along the x-axis. These distributions are used as initial values for the integration of the GS equation, which governs 2-D magneto-hydrostatic equilibria

$$\partial^2 A/\partial x^2 + \partial^2 A/\partial y^2 = -\mu_0 j_z = -\mu_0 dP_t/dA \tag{9.1}$$

Here $A(x, y)\hat{z}$ is the vector potential describing the field components in the reconstruction plane so that $(B_x, B_y) = (\partial A/\partial y, -\partial A/\partial x)$, from which follows that curves defined by $A(x, y) = const.$ describe field lines, projected onto the xy-plane. The transverse pressure $P_t(A) = (p + B_z^2/2\mu_0)$ is a function of A only, because both the plasma pressure $p(A)$ and the field component $B_z(A)$ are constant along field lines; they are called field-line invariants. Eqn. 9.1 expresses the force balance in the xy-plane and perpendicular to the field, while $p = p(A)$ and $B_z = B_z(A)$ express the force balance along field lines in the xy-plane and along the z-axis, respectively. Use of the GS equation 9.1 requires the structures to be approximately 2-D, time-independent, and magneto-hydrostatic, i.e., inertia forces associated with any plasma flows remaining in the proper frame must be sufficiently small to be neglected.

The values $A(x, 0)$ of the vector potential on the x-axis are obtained from the measured magnetic field component $B_y(x, 0) = -\partial A(x, 0)/\partial x$ by integration. The result is used for two purposes. First, the values $A(x, 0)$ provide the spatial initial values for the integration. Second, the plasma pressure $p(x, 0)$ and $B_z(x, 0)$ are both measured along the x-axis so that $P_t(x, 0)$ is also known there. By use of $A(x, 0)$, these quantities can be expressed as the functions $p(A)$, $B_z(A)$, and $P_t(A)$. They are then known, not only on the x-axis, but in the entire part of the xy-plane threaded by field lines that intersect the x-axis and were encountered by the spacecraft during the data interval used in the reconstruction. In those portions of the reconstruction domain not magnetically connected to the x-axis, the functions must be represented by suitable extrapolations. The curves representing the field-line invariants as functions of A, may have more than one branch. If so, suitable criteria for switching branches in the integration are needed. For example, in magnetopause applications two branches are commonly present, one applicable in the magnetosphere and one in the magnetosheath. In this case, the location where B_x changes sign has been used for the switch [*Hu and Sonnerup*, 2003], but other criteria are also possible.

The integration consists of taking small steps $\pm\Delta y$ away from the x-axis, in each step using the Taylor series

$$A(x, y \pm \Delta y) = A(x, y) \pm \Delta y(\partial A(x, y)/\partial y) + \frac{1}{2}(\Delta y)^2(\partial^2 A(x, y)/\partial y^2) \tag{9.2}$$

to obtain new A-values. Here $\partial A(x, y)/\partial y = B_x(x, y)$ is known and $\partial^2 A(x, y)/\partial y^2 = -\partial^2 A(x, y)/\partial x^2 - \mu_0 dP_t/dA$ is taken from the GS equation. Similarly, we use

$$B_x(x, y \pm \Delta y) = B_x(x, y) \pm \Delta y(\partial B_x(x, y)/\partial y) \tag{9.3}$$

to obtain new B_x values. In this expression, $\partial B_x(x, y)/\partial y = \partial^2 A(x, y)/\partial y^2$, which is again taken from the GS equation. This simple integration method can be extended by carrying more terms in the series expansions 9.2 and 9.3 [*Sonnerup et al.*, 2006], one result being that the integration will now require use of, not only the first derivative $dP_t(A)/dA$, but also higher derivatives, $d^2P_t(A)/dA^2$, etc.. Even so, the procedure remains mathematically unstable. However, validations against known exact solutions of the GS equation have demonstrated that, by use of simple low-pass filtering [*Hau and Sonnerup*, 1999] and suitable nudging to suppress the build-up of total-pressure peaks [*Hu and Sonnerup*, 2003], the integration can be carried out with small errors over a substantial range of y-values centred around $y = 0$. The resulting reconstruction domain is rectangular, with its long sides parallel to the x-axis. The maximum aspect ratio to stay within a 2% error (say) varies from one benchmark test to another but is typically in the range 1/4 to 1/5.

In applications to single-spacecraft data, the errors cannot be quantified. The decision concerning how far to extend the integration domain in the y-direction is then a subjective one, based on the field behaviour in the map at its upper and lower edges.

9.1.2 Invariant axis and map optimisation

One of the most difficult steps in single-spacecraft applications is to find the orientation of the invariant axis. Various methods have been attempted: (i) obtaining, by trial and error, well defined functions $P_t(A)$, $p(A)$, and $B_z(A)$ with minimal scatter of the measured values around one or more branches of suitable polynomial representations [*Hau and Sonnerup*, 1999] ; (ii) optimising, by trial and error, the agreement between values of these field-line invariants obtained for field lines that intersect the x-axis more than once, a method that appears effective for flux ropes where each field line is encountered twice by the spacecraft as it moves along the x-axis [*Hu and Sonnerup*, 2002]; (iii) using the method described in Section 7.3.2.

In multi-spacecraft applications, the following procedure has been developed: The data set from each spacecraft is used to obtain a reconstructed field map that is then used to predict the field values at points along the paths of the other spacecraft in the reconstruction plane. The correlation coefficient between predicted and actually measured field components along these paths is then maximised by trial and error to find the optimal axis orientation [*Hasegawa et al.*, 2004; *Sonnerup et al.*, 2004]. Experience indicates that, at least in some applications, a good starting point for the search is the intermediate variance direction from minimum variance analysis of the magnetic-field data (MVAB; see Chapter 8 of ISSI SR-001). Other multi-spacecraft methods for obtaining the invariant axis and its motion are the gradient-based method [*Shi et al.*, 2005, 2006], applicable for small spacecraft separations, and the triangulation method [*Zhou et al.*, 2006a, b], applicable for larger separations.

As a further step in producing an optimal axis orientation and map, the following method has been developed to merge reconstructed field maps of the same structure, observed by several spacecraft into a single map [*Hasegawa et al.*, 2005]: A suitably chosen Gaussian weight distribution in y is applied to the $A(x,y)$ distribution of each individual map, with maximum weight on the spacecraft path from which it was generated. The weighted $A(x,y)$ distributions of the maps from all spacecraft are then super-imposed to produce a combined map. The correlation between the field components predicted by the composite map and those actually measured by the various spacecraft can then be further

optimised by making small adjustments to the orientation of the invariant axis. The combined map does not satisfy the GS equation exactly but the deviations are usually small. In a few applications of this technique at the magnetopause, with Cluster spacecraft separations of 2000-3000 km, correlation coefficients (cc) between predicted and measured field components have exceeded 0.99 and not uncommonly have been ≥ 0.98. An illustration is shown in Figure 9.1. A warning is in order here: when the spacecraft separation is small compared to the size of the reconstructed object, the cc tends to be very high and not a valid measure of overall map quality.

9.2 Structures with field-aligned flow

It can be shown [*Sonnerup et al.*, 2006] that the inclusion of field-aligned flows (such as commonly occur in the HT frame) in the description of 2-D time-independent structures also leads to a GS-like equation, namely

$$\nabla\cdot[(1-M_A^2)\nabla A] = \mu_0\rho[TdS/dA - dH/dA] - B_z dC_z/dA - (B^2/2\mu_0\rho)dG^2/dA \quad (9.4)$$

in which $M_A = (v/B)\sqrt{\mu_0\rho}$ is the Alfvén-Mach number based on the flow speed v. There are now four field-line (and streamline) invariants: the entropy $S(A) = c_v \ln(T/\rho^{(\gamma-1)})$; the total enthalpy $H(A) = h + v^2/2 = c_p T + v^2/2$; the mass-flux invariant $G(A) = \mu_0\rho v/B = M_A\sqrt{\mu_0\rho}$; and the axial-momentum invariant $C_z(A) = (1 - M_A^2)B_z$. As before, the GS equation expresses the force balance transverse to the field in the reconstruction plane; $S(A)$, $H(A)$, and $G(A)$ together describe isentropic, compressible, field-aligned flow, with $1/B$ in $G(A)$ playing the role of cross-sectional area of a flux and flow tube; and $C_z(A)$ expresses the axial momentum balance.

In the limit $v \to 0$, we see that $M_A \to 0$, $C_z(A) \to B_z(A)$, and $G(A) \to 0$, while the enthalpy and entropy invariants give $T \to T(A)$ and $\rho \to \rho(A)$, from which follows that $p = p(A)$. In this limit, Eqn. 9.4 reduces to 9.1, with field-line invariants T, ρ, p, and B_z: As expected, the system returns to the magneto-hydrostatic case.

The GS-like equation 9.4 has complications arising from the presence of quantities such as M_A, T, ρ, B_z, B^2, which are not field-line invariants and therefore must be advanced separately in the integration. The procedure can be cast in matrix form as $\mathsf{M}\cdot\boldsymbol{X}^T = \boldsymbol{Y}^T$, where the derivatives needed at each step of the integration are contained in the vector

$$\boldsymbol{X} = [(\partial T/\partial y), (\partial\rho/\partial y), (\partial v^2/\partial y), (\partial M_A^2/\partial y), (\partial B_z/\partial y), (\partial B^2/\partial y), (\partial^2 A/\partial y^2)] \quad (9.5)$$

The vector $\boldsymbol{Y}$ and the 7×7 matrix M were given by *Sonnerup et al.* [2006]; they contain only quantities that are known before each new step is taken. The matrix M is sparse and the system can be readily reduced to size 4×4. It must be inverted at each grid point in the integration. The inversion poses no problem, except when the matrix becomes singular, which occurs whenever the field-aligned flow speed becomes equal to one of the MHD wave speeds. Such a situation may arise in the study of reconnection events in which Alfvénic, or nearly Alfvénic, field-aligned flow is expected in the HT frame. Suitable events for application of the method should be such that a high-quality HT frame exists.

A numerical code for this type of reconstruction has been developed by *Teh* [2007] and *Teh et al.* [2007]. It has been successfully benchmarked by use of an exact axi-symmetric solution of Eqn. 9.4 and then used to reconstruct a magnetopause encounter by Cluster that

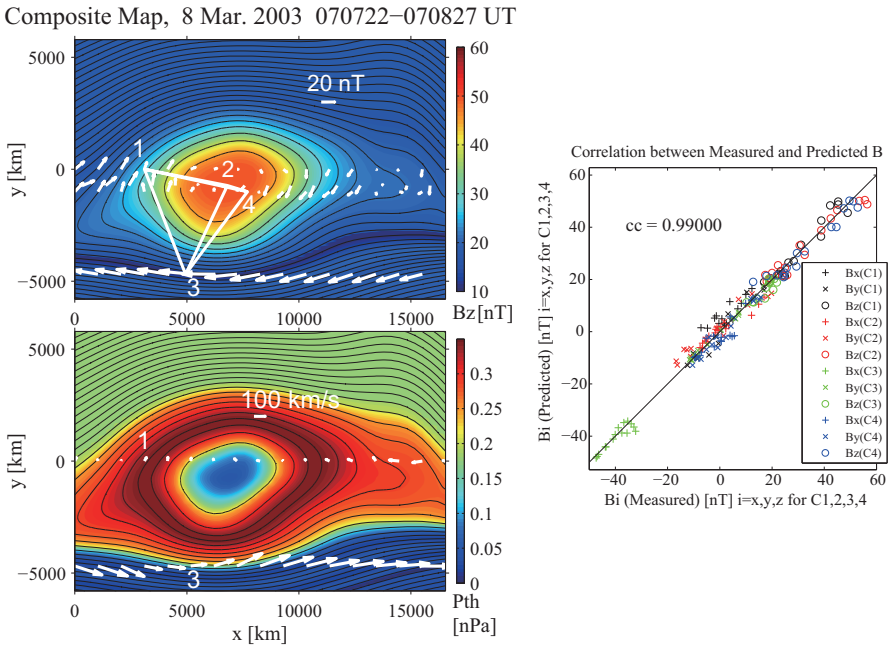

Figure 9.1: Magneto-hydrostatic GS reconstruction of flux transfer event (FTE) from Cluster data. The upper left panel shows projection of field lines onto the reconstruction (xy) plane as black curves, with the axial (z) field in colour. The white tetrahedron is the spacecraft configuration, which moves rapidly from left to right; the white arrows represent the measured magnetic field vectors, projected onto the xy plane. The magnetosphere is at bottom; tailward is left. The FTE signature was created by a flux rope, embedded in the magnetopause layer and moving tailward past the spacecraft. In the lower left panel, colours show plasma pressure; white arrows represent measured plasma velocity vectors, after transformation to the reconstruction frame (the HT frame; see Chapter 7), which moves at nearly the magnetosheath plasma flow speed so that velocities are small in the magnetosheath and flux rope, but are large in the magnetosphere. The right panel shows the correlation between measured field components and those predicted from the field map. The map is a composite of four maps, each created from magnetic data measured by an individual spacecraft. Orientation of invariant (z) axis was obtained by optimisation of the correlation coefficient (cc). Adapted from *Sonnerup et al.* [2004] and *Hasegawa et al.* [2006].

had been previously studied in the magneto-hydrostatic approximation [*Hasegawa et al.*, 2004, 2005]. The qualitative agreement was found to be good but a new phenomenon, namely supersonic field-aligned flow in the HT frame, could now be described.

9.3 Plasma flow transverse to the magnetic field

It can be shown [*Sonnerup et al.*, 2006] that plasma flow transverse to a unidirectional (but non-constant) magnetic field, $\boldsymbol{B} = B(x, y)\hat{\boldsymbol{z}}$, also is governed by a GS-like equation, namely

$$\nabla \cdot [(1/\rho)\nabla\psi] = \rho[d\tilde{H}/d\psi - TdS/d\psi] - [\rho^2/(2\mu_0)]dF^2/d\psi \tag{9.6}$$

where $\psi(x, y)$ is the compressible stream-function, i.e., $\rho\boldsymbol{v} = \nabla\psi \times \hat{\boldsymbol{z}}$, and the streamline invariants are: the entropy $S(\psi) = c_v \ln(T/\rho^{(\gamma-1)})$; the modified total enthalpy $\tilde{H}(\psi) = h + v^2/2 + B^2/(\mu_0\rho)$; and the frozen-flux invariant $F(\psi) = B/\rho$. Note that a field-aligned flow component of the form $v_z = v_z(\psi)$ has no influence on the force balance and therefore can be included, at will.

The integration is advanced by inversion of the 5×5 matrix equation $\mathsf{M} \cdot \boldsymbol{X}^T = \boldsymbol{Y}^T$, where the required derivatives are contained in the vector

$$\boldsymbol{X} = [(\partial T/\partial y), (\partial\rho/\partial y), (\partial B/\partial y), (\partial v^2/\partial y), (\partial^2\psi/\partial y^2)] \tag{9.7}$$

while M and $\boldsymbol{Y}$ contain quantities that are known at each step of the integration (for details, see *Sonnerup et al.* [2006]). The system can be easily reduced to size 3×3. The matrix is singular when $v_y^2 = (c_s^2 + v_A^2)$, where c_s and v_A are the local speed of sound and Alfvén speed, respectively. In other words, singular behaviour occurs when v_y reaches the fast-mode MHD wave speed.

A numerical code for this type of reconstruction has been developed [*Hasegawa et al.*, 2007b] and benchmarked, both with an exact, axi-symmetric solution of Eqn. 9.6 and with simulation of a time-evolving Kelvin-Helmholtz vortex. In spite of the time dependence, as a result of which the streamline invariants are in fact not even nearly constant along streamlines, the reconstruction is able to well describe the actual instantaneous velocity field in the vortex. In their paper, *Hasegawa et al.* [2007b] also applied the technique to Geotail observations in the low-latitude flank boundary layer, just earthward of the magnetopause. Streamlines indicating the presence of a chain of vortices were obtained from the reconstruction.

The experience to date with this kind of reconstruction is limited but indications are that multi-spacecraft information is needed to find the proper frame of the flow structures and to determine an optimal invariant direction in situations where the magnetic field is not completely unidirectional, as, in practice, it essentially never is.

9.4 General two-dimensional MHD structures

Recently, it has been shown that, rather than being restricted to GS-like systems, reconstruction from single-spacecraft data is in principle possible for any 2-D time-independent ideal MHD structure [*Sonnerup and Teh*, 2008]. The magnetic field is again described as

$\boldsymbol{B}(x, y) = \nabla A(x, y) \times \hat{\boldsymbol{z}} + B_z(x, y)\hat{\boldsymbol{z}}$, while the velocity field, which is no longer necessarily aligned with $\boldsymbol{B}$ (as it was in Section 9.2), or transverse to it (as it was in Section 9.3), is described by $\boldsymbol{v}(x, y) = (1/\rho)\nabla\psi(x, y) \times \hat{\boldsymbol{z}} + v_z(x, y)\hat{\boldsymbol{z}}$. One streamline invariant still exits, namely the entropy $S(\psi) = c_v \ln(T/\rho^{\gamma-1}$. As before, the integration procedure is expressible in terms of a matrix equation of the form $\mathsf{M} \cdot \boldsymbol{X}^T = \boldsymbol{Y}^T$, where the derivatives needed to advance the integration are contained in the vector

$$\boldsymbol{X} = [(\partial\rho/\partial y), (\partial p/\partial y), (\partial v_z/\partial y), (\partial B_z/\partial y), (\partial^2\psi/\partial y^2), (\partial^2 A/\partial y^2)] \tag{9.8}$$

and the 6×6 matrix M, as well as the vector $\boldsymbol{Y}$, contain only quantities that are known at each step of the integration. The matrix is invertible, except when the plasma velocity component v_y reaches one of the MHD wave speeds along the y-direction. The advantage of reconstruction directly from the MHD equations is that it can be applied to situations where flow effects are important but where no HT frame exists. An example is magnetic-field reconnection, viewed in the frame of reference in which the reconnection site (the X-line) is stationary. At locations well away from this site, a good HT frame may exist so that GS reconstruction with field-aligned flow (Section 9.2) can be used. But the price paid is that, in such a frame, the X-line moves away, often at a high speed, and also that the separatrices at the boundaries of a wedge of reconnected field lines appear to be receding from each other. In other words, the configuration appears time dependent.

For single-spacecraft applications, the orientation and motion of the invariant axis (e.g., the X-line in a reconnection event) can in principle be determined from the method described in Section 7.3.2. If this method fails, one may need information from more than one spacecraft in order to find a reliable orientation and motion. One condition to be satisfied, to the extent permitted by the data, is the constancy of the axial electric field (e.g., the reconnection electric field) in the proper frame. The measured initial velocities and magnetic fields (at points along the x-axis) usually are not such as to meet this condition exactly. Even if the initial axial electric field is constant, the integration procedure in its simplest form does not strictly enforce the constancy of this field throughout the map. How to optimally deal with these difficulties may vary from case to case. In some events one may be able to 'sanitise' the initial values so that the axial electric field at x=0 becomes constant. In other events this step may not be practical. In either case, it may be desirable to introduce nudging toward a constant axial electric field in each step of the integration.

A numerical code to perform the integration has been developed and successfully benchmarked, using an exact axi-symmetric solution of the ideal MHD equations [see *Sonnerup and Teh*, 2008]. Applications to events seen by Cluster and other spacecraft are underway.

9.5 Discussion

Reconstruction methods of the type discussed in this chapter represent a logical extension of earlier qualitative or semi-quantitative data interpretation methods. For example, a bipolar signature in the magnetic-field component along the vector normal to the magnetopause, first observed by *Russell and Elphic* [1978] and referred to as a Flux Transfer Event (FTE), was initially, and correctly, interpreted in terms of a flux-rope like structure moving along the magnetopause past the observing spacecraft. Later on, more quantitative models of flux ropes having circular or elliptical symmetry with certain free parameters

have been fitted to the observations. A natural further development toward a quantitative description that contains no assumptions about the cross section of the flux rope is to seek the aid of various forms of the MHD equations, as is done in the reconstruction methods described here. A stumbling block is that these methods are mathematically ill-posed: integration as a spatial initial-value problem, i.e., as a Cauchy problem, is intrinsically unstable and ultimately causes the solution to be dominated by spurious, rapidly growing parts. Nevertheless, benchmarking against exact solutions has shown that, by suppressing such parts in each step of the integration, a field of view of substantial width around the spacecraft trajectory can be gained in which the reconstructions have only small errors (see the work by *Hu and Sonnerup* [2003]). For example, magneto-hydrostatic reconstructions of a set of FTEs [*Hasegawa et al.*, 2006] almost certainly have sufficient accuracy to unambiguously establish that the FTE signatures were caused by swellings of the magnetopause layer associated with embedded flux ropes (see Figure 9.1) and not by undulations associated with surface waves, as has also been proposed.

A difficulty, common to all but the first of the methods described in this chapter, is that the initial data usually are not fully consistent with the functional representations chosen for the various field-line or streamline invariants. As long as the deviations are reasonably small, this problem can be dealt with by making modifications of ('sanitising') the initial values of some of the non-invariant quantities appearing in the equations so that they become consistent. The procedure is outlined in the appendix of the paper by *Hasegawa et al.* [2007b]. Such corrections may also be made by a nudging process applied in each step of the integration to assure that the invariants remain strictly invariant. In magneto-hydrostatic GS reconstruction, these problems do not arise, because, in this case, only the functional representation of the field-line invariant on the right side of the GS equation, i.e., the axial current density, enters into the integration; in the other three methods, the equations also contain various non-conserved coefficients.

A related difficulty associated with the invariants is that, on field lines and/or streamlines encountered more than once by the spacecraft on which the map is based, the value of an invariant may not be the same at all encounters. This is usually an indication of deviations from the model assumptions of time-independence, and/or two-dimensionality. For small inconsistencies, one may simply use an average value of the invariant; for more significant ones, a better map may in some cases be obtained by using more than one branch of the curve relating the value of the invariant to the corresponding value of the vector potential or stream function. A suitable criterion for the switch of branches in the integration must then be adopted.

To use the reconstruction methods, the field and/or flow structures have to be two-dimensional, or at least have substantial elongation in one direction, and they have to be approximately time independent in their proper frame. Numerical experimentation using synthetic data from numerical simulations have indicated that, at least in some cases, violations of time stationarity present in the initial data [*Hasegawa et al.*, 2007b] still allows reasonably accurate reconstruction of flow (or field) but not the spatial distribution of various other plasma properties. A similar experiment, using synthetic data from a numerical simulation of three-dimensional, guide-field reconnection, has shown that the reconstructed field map again provides a qualitatively correct representation of the actual instantaneous field distribution in the reconstruction plane, namely, in this particular case, a circular field pattern indicating a concentration of current perpendicular to the reconstruction plane. Interpretation of the map in terms of a quasi two-dimensional structure,

namely a flux rope, is tempting but would be seriously misleading since no such elongated structure is evident in the actual three-dimensional simulation results [*Hasegawa et al.*, 2007a].

The reconstruction methods described here are fairly advanced data analysis tools. How well they work depends on how well the model assumptions are met and how well the invariant axis and its motion have been determined. Multi-spacecraft information is of great importance in determining these parameters and in assessing the quality of the reconstruction results. It must be remembered that, once the initial conditions (at $y = 0$) are set, the integration will usually produce a map. Whether this map is physically meaningful or not must be carefully assessed in each individual case. Therefore, these methods are not suited for mass application. Indeed, the more sophisticated the reconstruction method, the harder it is to find events for which it is well suited. The simplest and most robust of the four methods described here is the magneto-hydrostatic GS reconstruction, followed by GS reconstruction of streamlines in flow perpendicular to a unidirectional magnetic field.

The reconstruction methods have not yet been developed to include effects outside of ideal MHD (an exception is the case of double-polytropic field-aligned flow [*Sonnerup et al.*, 2006]. In particular, the Hall effect and the effects of finite resistivity are not included, although the general MHD reconstruction described in Section 9.4 can be modified to include such effects. On the whole, the data analysis tools described here are still in their infancy. More experience with them, more validation of them to explore their limitations, and perhaps a better integration technique, are all needed. Finally, we note that there may be other structures in space, in the environment, or in the laboratory, governed by significantly different physical processes, that can be reconstructed by approaches similar to those presented here.

Acknowledgement

Writing of this chapter was supported by National Aeronautics and Space Administration under Cluster Theory Guest Investigator Grant NNG-05-GG26G to Dartmouth College.

Bibliography

De Keyser, J., Dunlop, M. W., Owen, C. J., Sonnerup, B. U. Ö., Haaland, S. E., Vaivads, A., Paschmann, G., Lundin, R., and Rezeau, L., 2005, *Magnetopause and Boundary Layer*, vol. 20 of *Space Science Series of ISSI*, chap. 8, pp. 231–320, Springer Verlag, Berlin, reprinted from Space Sci. Rev., 118, Nos. 1-4, 2005.

Hasegawa, H., Sonnerup, B., Dunlop, M., Balogh, A., Haaland, S., Klecker, B., Paschmann, G., Lavraud, B., Dandouras, I., and Rème, H., 2004, Reconstruction of two-dimensional magnetopause structures from Cluster observations: verification of method, *Ann. Geophys.*, **22**, 1251–1266, http://www.ann-geophys.net/22/1251/2004/.

Hasegawa, H., Sonnerup, B. U. Ö., Klecker, B., Paschmann, G., Dunlop, M. W., and Rème, H., 2005, Optimal reconstruction of magnetopause structures from Cluster data, *Ann. Geophys.*, **23**, 973–982, http://www.ann-geophys.net/23/973/2005/.

Hasegawa, H., Sonnerup, B. U. Ö., Owen, C. J., Klecker, B., Paschmann, G., Balogh, A., and Rème, H., 2006, The structure of flux transfer events recovered from Cluster data, *Ann. Geophys.*, **24**, 603–618, http://www.ann-geophys.net/24/603/2006/.

Hasegawa, H., Nakamura, R., Fujimoto, M., Sergeev, V. A., Lucek, E. A., Rème, H., and Khotyaintsev, Y., 2007a, Reconstruction of a bipolar magnetic signature in an earthward jet in the tail: Flux rope or 3D guide-field reconnection?, *J. Geophys. Res.*, **112**, A11206, doi:10.1029/2007JA012492.

Hasegawa, H., Sonnerup, B. U. Ö., Fujimoto, M., Saito, Y., and Mukai, T., 2007b, Recovery of streamlines in the flank low-latitude boundary layer, *J. Geophys. Res.*, **112**, A04213, doi:10.1029/2006JA012101.

Hau, L.-N. and Sonnerup, B. U. Ö., 1999, Two-dimensional coherent structures in the magnetopause: Recovery of static equilibria from single-spacecraft data, *J. Geophys. Res.*, **104**, 6899–6918, doi:10.1029/1999JA900002.

Hu, Q. and Sonnerup, B. U. Ö., 2002, Reconstruction of magnetic clouds in the solar wind: Orientations and configurations, *J. Geophys. Res.*, **107**, 1142, doi:10.1029/2001JA000293.

Hu, Q. and Sonnerup, B. U. Ö., 2003, Reconstruction of two-dimensional structures in the magnetopause: Method improvements, *J. Geophys. Res.*, **108**, 1011, doi:10.1029/2002JA009323.

Russell, C. T. and Elphic, R. C., 1978, Initial ISEE magnetometer results—Magnetopause observations, *Space Sci. Rev.*, **22**, 681–715.

Shi, Q. Q., Shen, C., Pu, Z. Y., Dunlop, M. W., Zong, Q.-G., Zhang, H., Xiao, C. J., Liu, Z. X., and Balogh, A., 2005, Dimensional analysis of observed structures using multipoint magnetic field measurements: Application to Cluster, *Geophys. Res. Lett.*, **32**, L012105, doi:10.1029/2005GL022454.

Shi, Q. Q., Shen, C., Dunlop, M. W., Pu, Z. Y., Zong, Q.-G., Liu, Z. X., Lucek, E., and Balogh, A., 2006, Motion of observed structures calculated from multi-point magnetic field measurements: Application to Cluster, *Geophys. Res. Lett.*, **33**, L08109, doi:10.1029/2005GL025073.

Sonnerup, B. U. Ö. and Guo, M., 1996, Magnetopause transects, *Geophys. Res. Lett.*, **23**, 3679–3682, doi:10.1029/96GL03573.

Sonnerup, B. U. Ö. and Teh, W.-L., 2008, Reconstruction of two-dimensional MHD structures in a space plasma: The theory, *J. Geophys. Res.*, **113**, in press, doi:10.1029/2007JA012718.

Sonnerup, B. U. Ö., Hasegawa, H., and Paschmann, G., 2004, Anatomy of a flux transfer event seen by Cluster, *Geophys. Res. Lett.*, **31**, L11803, doi:10.1029/2004GL020134.

Sonnerup, B. U. Ö., Hasegawa, H., Teh, W.-L., and Hau, L.-N., 2006, Grad-Shafranov reconstruction: An overview, *J. Geophys. Res.*, **111**, A09204, doi:10.1029/2006JA011717.

Teh, W.-L., 2007, *A study of two-dimensional magnetopause structure based on Grad-Shafranov reconstruction method*, Ph.D. thesis, Institute of Space Science, National Central Univ., Jhongli, Taiwan, R. O. C.

Teh, W.-L., Sonnerup, B. U. Ö., and Hau, L.-N., 2007, Grad-Shafranov reconstruction with field-aligned flow: First results, *Geophys. Res. Lett.*, **34**, L05109, doi:10.1029/2006GL028802.

Zhang, Y. C., Liu, Z. X., Shen, C., Fazakerley, A., Dunlop, M., Réme, H., Lucek, E., Walsh, A. P., and Yao, L., 2007, The magnetic structure of an earthward-moving flux rope observed by Cluster in the near-tail, *Ann. Geophys.*, **25**, 1471–1476, http://www.ann-geophys.net/25/1471/2007/.

Zhou, X.-Z., Zong, Q.-G., Pu, Z. Y., Fritz, T. A., Dunlop, M. W., Shi, Q. Q., Wang, J., and Wei, Y., 2006a, Multiple Triangulation Analysis: another approach to determine the orientation of magnetic flux ropes, *Ann. Geophys.*, **24**, 1759–1765, http://www.ann-geophys.net/24/1759/2006/.

Zhou, X.-Z., Zong, Q.-G., Wang, J., Pu, Z. Y., Zhang, X. G., Shi, Q. Q., and Cao, J. B., 2006b, Multiple triangulation analysis: application to determine the velocity of 2-D structures, *Ann. Geophys.*, **24**, 3173–3177, http://www.ann-geophys.net/24/3173/2006/.

— 10 —

Empirical Reconstruction

JOHAN DE KEYSER
Belgian Institute for Space Astronomy
Brussels, Belgium

10.1 Introduction

Empirical reconstruction methods attempt to interpret *in situ* observations of the magnetospheric boundary in terms of time-stationary structures that are convected past the spacecraft. The ever-changing position of the boundary is considered an unknown of the problem. Once the motion of the boundary is found, empirical reconstruction produces spatial maps showing how physical quantities vary as a function of position relative to the boundary. For a planar boundary moving at a constant speed, for instance, the time scale can be linearly transformed into a distance scale. While useful for short-duration magnetopause crossings (up to tens of seconds), a more powerful way of establishing boundary motion over a long time interval (hours, a whole boundary pass) is needed. A pioneering technique was proposed by *Paschmann et al.* [1990]. More advanced techniques have been developed since then. This chapter presents a generalised description of these methods and discusses their application.

Consider K spacecraft whose position x_{sc}^{k} ($k = 1, \ldots, K$) in space is given. Spacecraft k measures the local plasma velocity $\boldsymbol{v}(t_i^{k,v})$ at times $t_i^{k,v}$ identified by the subscript i, and provides magnetic field data $\boldsymbol{B}(t_i^{k,B})$ at times $t_i^{k,B}$. Inter-calibrated observations $f^l(t_i^{k,l})$ at sample times $t_i^{k,l}$ are assumed to be available for a set of $l = 1, \ldots, L$ physical variables, such as plasma component densities or temperatures, magnetic field strength, etc. Not all the spacecraft have to provide the same types of data. The number of measurements, as well as their timing, can differ from spacecraft to spacecraft.

10.2 Dimensionality and initial reference frame

The dimensionality of the structure can be determined through minimum variance analysis of $\boldsymbol{n}(t_i^{k,B}) = \boldsymbol{B}(t_i^{k,B}) \times \Delta\boldsymbol{B}(t_i^{k,B})/|\boldsymbol{B}(t_i^{k,B}) \times \Delta\boldsymbol{B}(t_i^{k,B})|$, where $\Delta\boldsymbol{B}(t_i) = \boldsymbol{B}(t_{i+1}) - \boldsymbol{B}(t_{i-1})$, i.e., of the local normal direction assuming the boundary is magnetic field aligned [*De Keyser et al.*, 2002]. The variances $\sigma_x^2, \sigma_y^2, \sigma_z^2$ are sorted in descending order. The minimum variance analysis usually gives $\sigma_x^2, \sigma_y^2 \gg \sigma_z^2$. This reflects one- or two-dimensional structure, with z typically along the magnetospheric magnetic field; an additional rotation around z may be needed to point x in the average outward normal direction. The case $\sigma_x^2 \approx \sigma_y^2 \approx \sigma_z^2$ implies three-dimensional structure. We will consider only the one- and two-dimensional cases.

The additional rotation is obtained by trial and error. For each possible rotation, one can attempt the one-dimensional reconstruction (explained in section 10.3 below). The rotation angle that leads to the solution with minimal width is preferred. It should be noted that the results of the more advanced empirical reconstruction methods are not strongly sensitive to the precise value of this rotation angle.

The (x, y, z) frame differs from the traditional (L, M, N) boundary coordinates in that it results from a variance analysis of $\boldsymbol{n}$ rather than $\boldsymbol{B}$, and that it is usually obtained for a much longer time interval (more than an individual magnetopause crossing), knowing that the boundary orientation is actually changing in the meantime. In practice, however, z corresponds more or less to L and, after the aforementioned additional rotation, x and y correspond to an average N and M.

10.3 One-dimensional reconstruction

In a reference frame moving with the boundary, the apparent temporal variations translate into spatial variations. Given the motion $v_{\mathrm{mpbl}}(t)$ of the boundary, its position is

$$x_{\mathrm{mpbl}}(t) = \int_{t_{\mathrm{ref}}}^{t} v_{\mathrm{mpbl}}(t')dt' + x_{\mathrm{mpbl}}(t_{\mathrm{ref}}) \tag{10.1}$$

where $x_{\mathrm{mpbl}}(t_{\mathrm{ref}})$ defines the boundary position at a reference time t_{ref}. One can take the measured plasma velocity v_x to be the boundary velocity v_{mpbl} [*Paschmann et al.*, 1990], but there are several difficulties with this choice:

- Integrating the oscillatory integrand v_{mpbl} leads to increasingly large relative errors as the time interval gets longer.
- The plasma velocity equals v_{mpbl} only if the boundary behaves as a planar, incompressible, tangential discontinuity slab.
- The precision of plasma velocity data is limited. Random errors may cancel as the integration proceeds, but systematic errors add up.
- The plasma velocity time resolution should be sufficient to track the motion of the boundary, that is, a few seconds or less.

The technique works for short time intervals and if the boundary does not experience dramatic accelerations. Using multi-spacecraft data effectively reduces the errors [*De Keyser et al.*, 2004]. Once $x_{\mathrm{mpbl}}(t)$ has been found, each measurement $f^l(t_i^{k,l})$ can be associated with the spacecraft's distance from the boundary $x = x_{\mathrm{sc}}^k(t_i^{k,l}) - x_{\mathrm{mpbl}}(t_i^{k,l})$, i.e., the position of the spacecraft in a frame that co-moves with the boundary with $\boldsymbol{v}_{\mathrm{frame}} = [v_{\mathrm{mpbl}}; 0; 0]$. For one-dimensional and time-stationary boundary structure, plotting a quantity as a function of x produces a single-valued relation: its spatial profile.

The difficulties with integrating 10.1 can be partially overcome by adopting an optimisation approach in which $v_{\mathrm{mpbl}}(t)$ and the spatial profiles of the L physical quantities are determined so as to optimise the quality of the spatial profile fits, and to minimise the deviation of the boundary velocity from an observed proxy $v_x(t)$ (the x-component of the plasma bulk velocity, of one or more component velocities, or of the electric drift

velocity), taking into account the observational errors. *De Keyser et al.* [2002] have used the magnetic field and plasma density and temperatures, together with prescribed profile shapes, to obtain one-dimensional reconstructions that satisfy pressure balance. A more sophisticated version [*De Keyser et al.*, 2005b] does not impose a specific shape of profile and works with any set of 'guiding variables' (the choice obviously will affect the quality of the result). The resulting optimisation is a nonlinear least-squares problem with a large number of free parameters. An effective optimisation strategy has been constructed so as to limit the computing time [for more details, see *De Keyser et al.*, 2005b]. The resulting algorithm is able to deal with measurement errors, the limited time resolution of the data, and occasional data gaps. Data from any number of spacecraft and any type of instrument can be exploited. An example with Cluster is shown in Figure 10.1. It is interesting to see the correspondence between density or field variations during boundary crossings and the position of the spacecraft relative to the computed instantaneous boundary position. Much of the observed time variability can be explained purely by the effect of boundary motion and the relative spacecraft positions.

10.4 Two-dimensional reconstruction

A one-dimensional approximation works for surface waves with a small amplitude-to-wavelength ratio (any boundary deformation can be thought of in terms of surface waves). If this hypothesis is not justified, two-dimensional empirical reconstruction can be used. The following choices for the co-moving frame can be considered:

- If there is only a downtail convection of the wave at a constant speed v_{wave}, the frame velocity is $\boldsymbol{v}_{\mathrm{frame}} = [0; v_{\mathrm{wave}}; 0]$. Plotting the observations along the spacecraft trajectory with $x = x_{\mathrm{sc}}(t)$ and $y = y_{\mathrm{sc}}(t) - v_{\mathrm{wave}}(t - t_0)$ is of limited use in the single-spacecraft context because it provides only a single transect through the structure. The situation is much more interesting with several spacecraft since the availability of several transects allows one to develop a two-dimensional picture of the observed structure.

- If there are *periodic* surface waves with period T, superposition of the data for several wave periods by taking $y = y_{\mathrm{sc}} + v_{\mathrm{wave}}\mathrm{mod}(t - t_0, T)$ may produce a detailed picture (multiple transects), even in the single-spacecraft case. (The modulo function $\mathrm{mod}(t, T)$ denotes the remainder of the division of t by T; for a linearly increasing first argument this produces a sawtooth function with period T.)

- A global, non-periodic, low frequency in/out motion of the boundary on which the periodic waves are superposed can be accounted for by computing $x_{\mathrm{mpbl}}(t)$ and checking how the position changes from period to period: At instants $t_0 + mT$, where $m = 0, \ldots, N$ counts the number of periods, the wave is in the same phase so that the frame velocity in x can be taken as $v_{\mathrm{mpbl,lf}}(t) = dx_{\mathrm{mpbl,lf}}/dt$, where $x_{\mathrm{mpbl,lf}}$ is the piecewise linear interpolant of x_{mpbl} at the times $t_0 + mT$, the piecewise linear curve connecting the points $(t_0 + mT, x_{\mathrm{mpbl}}(t_0 + mT))$ for $m = 0, \ldots, N$ [*De Keyser and Roth*, 2003].

One can then determine where each measurement was made in the two-dimensional co-moving frame. In general, the measurement points are irregularly distributed over xy

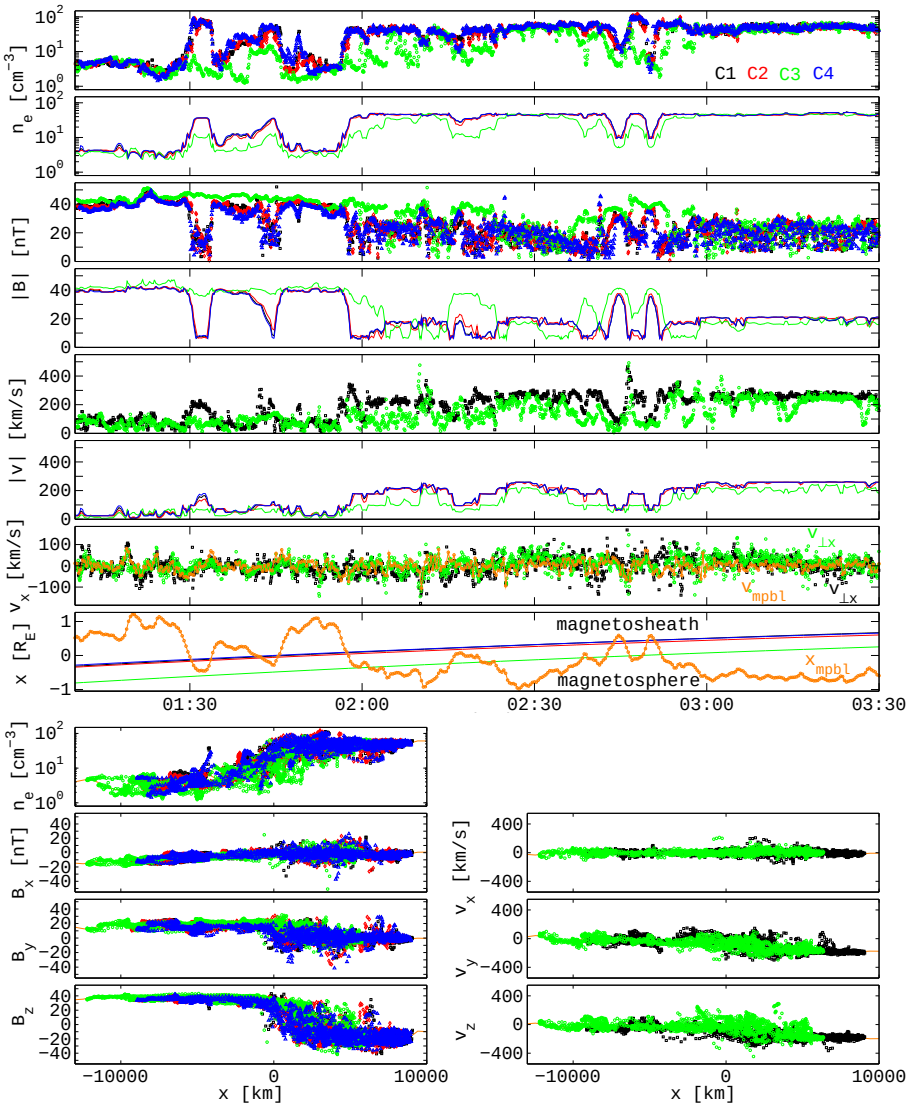

Figure 10.1: Empirical 1-D reconstruction for an outbound magnetospheric boundary pass by Cluster on June 6, 2001, 01:10–03:30 UT, computed with a time resolution of 20 s, using $v_{\perp x}$ from C1 and C3 as boundary motion proxy, with electron density n_e and magnetic field B_z as guiding variables. Top panels: Time profiles of electron density observations (PEACE, C1–C4); n_e predictions from the reconstruction (C1–C4); magnetic field strength observations (FGM, C1–C4); $|B|$ predictions (C1–C4); plasma velocity magnitude observations (CIS/HIA, C1 and C3); $|v|$ predictions (C1–C4); boundary motion proxy $v_{\perp x}$ (C1 and C3) and reconstructed velocity v_{mpbl}; and finally reconstructed boundary position x_{mpbl} and spacecraft trajectories (C1–C4, with C1, C2, and C4 close together). Bottom panels: Predicted spatial profiles of electron density (C1–C4), magnetic field (C1–C4), and plasma velocity (C1 and C3). After Figure 5 in *De Keyser et al.* [2005b].

space. They can be supplemented by imposing constant magnetospheric and magnetosheath values. Smoothing and/or interpolating this set of data points leads to two-dimensional spatial profiles [*De Keyser and Roth*, 2003]. Multi-spacecraft data result in a better coverage of the structure in the two-dimensional spatial domain, producing correspondingly better reconstructions, at least if the spacecraft separations are not too small.

Empirical reconstruction methods cannot deal with transient structures. For surface waves, this can be overcome by moving along with the wave, as discussed above. For other convecting two-dimensional structures, such as FTEs, the same approach can be used. This requires that the FTE propagation speed would be used instead of the wave speed. Of course, there is no periodicity that one can benefit from. In the presence of such structures, one could question whether the locally measured velocity can serve as a good boundary motion proxy, although the more sophisticated methods might overcome this.

10.5 Discussion

Empirical reconstruction techniques for determining the structure of the magnetopause and low-latitude boundary layer are very recent [for a review, see *De Keyser*, 2006]. While useful in the single-spacecraft context, they are especially promising for multi-spacecraft observations. The number of published applications is very limited.

For short time intervals and with an accurate boundary velocity proxy, one-dimensional empirical reconstruction methods produce detailed spatial profiles that reveal the structure of the magnetospheric boundary, e.g., substructure in the low-latitude boundary layer [*De Keyser et al.*, 2005a, p. 306–307], as well as the thickness of the magnetopause and of the low-latitude boundary layer. They can also track boundary motion over an extended time period (with an inaccurate proxy, sometimes at the cost of enforcing some smoothness on the spatial profiles), and thereby permit:

- verification of the extent to which boundary motion alone can explain the observed time variability without having to invoke specific time-dependent (energy or plasma transfer) processes at the magnetopause [*De Keyser et al.*, 2002, 2005b];

- assessment of the relation between boundary motion and solar wind pressure. The statistical correlation between both, measured at discrete times (magnetopause crossings), is based on pressure balance considerations and has been used to create empirical models of magnetopause position [*Sibeck et al.*, 1991]. Knowing the boundary position as a continuous function of time allows this correlation to be studied in more detail [*De Keyser et al.*, 2006].

Two-dimensional reconstruction provides the geometry of surface waves [*De Keyser and Roth*, 2003; *De Keyser et al.*, 2004] on the magnetopause and/or on the inner edge of the low-latitude boundary layer, including wave amplitudes and wavelengths, which are fundamental to understanding the undulating boundary [*Sckopke et al.*, 1981]. Another topic is the possibly non-sinusoidal shape of boundary waves caused by their nonlinear evolution [*Sibeck*, 1990; *Chen and Kivelson*, 1993; *Chen et al.*, 1993; *Hasegawa et al.*, 2004]. The technique may also provide the correct interpretation of magnetopause signatures that can point either to surface waves or to other structures (e.g. flux transfer events), especially when multi-spacecraft data are available [*Sibeck*, 1992; *Song et al.*, 1994; *Sibeck*

et al., 2000; *De Keyser et al.*, 2001]. If the technique doesn't work well in spite of detailed measurements, the underlying assumption of a surface wave must be rejected.

In summary, empirical reconstruction methods compensate for the motion of the magnetospheric boundary for extended periods of time and produce a global picture of all multi-spacecraft, multi-channel data acquired during a boundary pass.

Software implementation

Matlab software to implement these methods is available at http://www.spaceweather.eu/en/software/mim.

Acknowledgement

The author acknowledges the support of the Belgian Federal Science Policy Office (PRODEX/Cluster).

Bibliography

Chen, S.-H. and Kivelson, M. G., 1993, On Non-Sinusoidal Waves at the Earths Magnetopause, *Geophys. Res. Lett.*, **20**, 2699.

Chen, S.-H., Kivelson, M. G., Gosling, J. T., Walker, R. J., and Lazarus, A. J., 1993, Anomalous Aspects of Magnetosheath Flow and of the Shape and Oscillations of the Magnetopause During an Interval af Strongly Northward Interplanetary Magnetic Field, *J. Geophys. Res.*, **98**, 5727.

De Keyser, J., 2006, The Earth's magnetopause: Reconstruction of motion and structure, *Space Sci. Rev.*, **121**, 225–235, doi:10.1007/s11214-006-6731-3.

De Keyser, J. and Roth, M., 2003, Structural analysis of periodic surface waves on the magnetospheric boundary, *Planet. Space Sci.*, **51**, 757–768, doi:10.1016/S0032-0633(03)00112-0.

De Keyser, J., Darrouzet, F., Roth, M., Vaisberg, O. L., Rybjeva, N., Smirnov, V., Avanov, L., Nemecek, Z., and Safrankova, J., 2001, Transients at the dawn and dusk side magnetospheric boundary: Surface waves or isolated plasma blobs?, *J. Geophys. Res.*, **106**, 25 503–25 516.

De Keyser, J., Darrouzet, F., and Roth, M., 2002, Trying to bring the Magnetopause to a Standstill, *Geophys. Res. Lett.*, **29**, 1453, doi:10.1029/2002GL015001.

De Keyser, J., Gustafsson, G., Roth, M., Darrouzet, F., Dunlop, M., Rème, H., Fazakerley, A., Décréau, P., and Cornilleau-Wehrlin, N., 2004, Reconstruction of the magnetopause and low latitude boundary layer topology using Cluster multi-point measurements, *Ann. Geophys.*, **22**, 2381–2389, http://www.ann-geophys.net/22/2381/2004/.

De Keyser, J., Dunlop, M. W., Owen, C. J., Sonnerup, B. U. Ö., Haaland, S. E., Vaivads, A., Paschmann, G., Lundin, R., and Rezeau, L., 2005a, Magnetopause and Boundary Layer, in *Outer Magnetospheric Boundaries: Cluster Results*, edited by G. Paschmann, S. J. Schwartz, C. P. Escoubet, and S. Haaland, pp. 231–320, ISSI, Berne, also published in *Space Science Reviews*, 118 (1–4), 2005.

De Keyser, J., Roth, M., Dunlop, M. W., Rème, H., Owen, C. J., and Paschmann, G., 2005b, Empirical reconstruction and long-duration tracking of the magnetospheric boundary in single- and multi-spacecraft contexts, *Ann. Geophys.*, **23**, 1355–1369, http://www.ann-geophys.net/23/1355/2005/.

De Keyser, J., Roth, M., Dunlop, M. W., Rème, H., Owen, C. J., and Paschmann, G., 2006, Solar wind pressure and the position of the magnetopause: a Cluster perspective, in *Proceedings of the Cluster and Double Star Symposium*, ESA SP-598, ESA Publ. Div., Noordwijk, Netherlands.

Hasegawa, H., Fujimoto, M., Phan, T.-D., Rème, H., Balogh, A., Dunlop, M. W., Hashimoto, C., and TanDokoro, R., 2004, Transport of solar wind into Earth's magnetosphere through rolled-up Kelvin-Helmholtz vortices, *Nature*, **430**, 755–758, doi:10.1038/nature02799.

Paschmann, G., Sonnerup, B. U. Ö., Papamastorakis, I., Baumjohann, W., Sckopke, N., and Lühr, H., 1990, The magnetopause and boundary layer for small magnetic shear: Convection electric fields and reconnection, *Geophys. Res. Lett.*, **17**, 1829–1832.

Sckopke, N., Paschmann, G., Haerendel, G., Sonnerup, B. U. Ö., Bame, S. J., Forbes, T. G., Hones, E. W. J., and Russell, C. T., 1981, Structure of the low-latitude boundary layer, *J. Geophys. Res.*, **86**, 2099–2110.

Sibeck, D. G., 1990, A Model for the Transient Magnetospheric Response to Sudden Solar Wind Dynamic Pressure Variations, *J. Geophys. Res.*, **95**, 3755–3771.

Sibeck, D. G., 1992, Transient events in the outer magnetosphere—boundary waves or flux-transfer events?, *J. Geophys. Res.*, **97**, 4009.

Sibeck, D. G., Lopez, R. E., and Roelof, E. C., 1991, Solar wind control of the magnetopause shape, location and motion, *J. Geophys. Res.*, **96**, 5489.

Sibeck, D. G., Prech, L., Safrankova, J., and Nemecek, Z., 2000, Two-point measurements of the magnetopause: Interball observations, *J. Geophys. Res.*, **105**, 237–244.

Song, P., Le, G., and Russell, C. T., 1994, Observational differences between flux-transfer events and surface-waves at the magnetopause, *J. Geophys. Res.*, **99**, 2309.

Authors' Addresses

Gérard Chanteur
CETP/CNRS
10–12, avenue de l'Europe
78140 Vélizy, France
Email: gerard.chanteur@cetp.ipsl.fr

Patrick W. Daly
Max-Planck-Institut für
Sonnensystemforschung
Max-Planck-Str. 2
37191 Katlenburg-Lindau, Germany
Email: daly@mps.mpg.de

Johan De Keyser
Belgian Institute for Space Astronomy
Ringlaan 3
B-1180 Brussels, Belgium
Email: johandk@aeronomie.be

Malcolm W. Dunlop
Rutherford Appleton Laboratory
Chilton, Didcot, OX11 0QX, United
Kingdom
Email: m.dunlop@rl.ac.uk

Jonathan Eastwood
Space Sciences Laboratory
University of California at Berkeley
7 Gauss Way
Berkeley CA 94720-7450, USA
Email: eastwood@ssl.berkeley.edu

Karl-Heinz Glassmeier
Institut für Geophysik und extraterrestrische
Physik
Technische Universität Braunschweig
D-38106 Braunschweig, Germany
Email: kh.glassmeier@tu-bs.de

Stein Haaland
Department of Physics
University of Bergen
Allegt 55
N 5007 Bergen, Norway
Email: Stein.Haaland@ift.uib.no

Hiroshi Hasegawa
Department of Space Plasma Physics
Institute of Space and Astronautical Science,
JAXA
3-1-1 Yoshinodai, Sagamihara, Kanagawa
229-8510, Japan
Email: hase@stp.isas.jaxa.jp

Tim Horbury
Space and Atmospheric Physics
The Blackett Laboratory
Imperial College London
Prince Consort Rd.
London SW7 2AZ, United Kingdom
Email: t.horbury@imperial.ac.uk

Bertrand Lefebvre
Space and Atmospheric Physics
The Blackett Laboratory
Imperial College London
Prince Consort Rd.
London SW7 2AZ, United Kingdom
Email: b.lefebvre@imperial.ac.uk

Kareem Osman
Space and Atmospheric Physics
The Blackett Laboratory
Imperial College London
Prince Consort Rd.
London SW7 2AZ, United Kingdom
Email: kareem.osman00@imperial.ac.uk

Götz Paschmann
Max-Planck-Institut für extraterrestrische
Physik
Postfach 1312
D-85741 Garching, Germany
Email: goetz.paschmann@mpe.mpg.de

Jean-Louis Pinçon
LPCE/CNRS
3A, avenue de la Recherche Scientifique
45071 Orléans CEDEX, France
Email: jlpincon@cnrs-orleans.fr

Steven J. Schwartz
Space and Atmospheric Physics
The Blackett Laboratory
Imperial College London
Prince Consort Rd.
London SW7 2AZ, United Kingdom
Email: s.schwartz@imperial.ac.uk

Chao Shen
State Key Laboratory of Space Weather
Center for Space Science and Applied Research
Chinese Academy of Sciences
Beijing 100080, China
Email: sc@cssar.ac.cn

Bengt U. Ö. Sonnerup
Thayer School of Engineering
Dartmouth College
Hanover, NH 03755, U.S.A.
Email: sonnerup@dartmouth.edu

Wai-Leong Teh
Thayer School of Engineering
Dartmouth College
Hanover, NH 03755, U.S.A.
Email: teh@dartmouth.edu

Joachim Vogt
School of Engineering and Science
Jacobs University Bremen
Campus Ring 1
D-28759 Bremen, Germany
Email: j.vogt@jacobs-university.de